UNIVERSITY
OF LATVIA
FACULTY OF PHYSICS, MATHEMATICS AND OPTOMETRY

Gopejenko Aleksejs

FIRST PRINCIPLES SIMULATIONS ON YTTRIUM AND OXYGEN PRECIPITATION INSIDE *fcc*-Fe LATTICE

SUMMARY OF DOCTORAL THESIS

Submitted for the Doctoral degree in physics
Subfield of Solid State Physics

Riga, 2020

This work was performed at the Institute of Solid State Physics, University of Latvia, beginning with September 2007 until September 2019.

Type of thesis: scientific papers

Scientific advisor: *Dr. Chem.* Yuri Zhukovskii, Senior Researcher, Institute of Solid State Physics, University of Latvia.

Scientific consulant: *Dr. Phys.* Dmitry Bocharov, Senior Researcher, Institute of Solid State Physics, University of Latvia.

Scientific consulant: *Dr. Phys.* Pavel Vladmirov, Senior Researcher, Institute for Applied Materials, Karlsruhe Institute of Technology, Germany

Reviewers of Doctoral Thesis:

1) Dr. habil.phys. Juris Purans, Senior Researcher, Institute of Solid State Physics, University of Latvia.

2) Dr. Matthias Krack, Group leader of Multiscale Materials Modelling Group, Paul Scherrer Institute, Villigen, Switzherland

3) Prof. Andrei Ruban, Department of Materials Science and Engineering, Royal Institute of Technology (KTH), Stockholm, Sweden

The defense of doctoral thesis will take place in an open session of the Promotion Council of Physics, Astronomy and Mechanics of the University of Latvia on the 7th of February, 2020, at 10:00 in the conference hall of the Institute of Solid State Physics, University of Latvia, Kengaraga street 8.

The full text of Thesis and its summary are available at the Library of the University of Latvia (Kalpaka Blvd. 4, Riga, Latvia) and at the University of Latvia Academic Library (Rupniecibas Str. 10, Riga, Latvia).

Chairperson of the Specialized Promotion Council of the scientific section of the Physics, Astronomy and Mechanics at the University of Latvia	*Dr. habil. phys*. Uldis Rogulis
Secretary of the Specialized Promotion Council	Laureta Buševica

ISBN: 978-9934-18-499-4

Contents

Abstract 4
List of abbreviations (Glossary) 5
1. Introduction 6
1.1. Motivation 6
1.2. Author's contribution 8
1.3. Scientific novelty 10
2. Literature review 10
2.1. Experimental study of ODS nanoparticles formation in RAFM steels 10
2.1.1. Manufacturing of ODS steels 11
2.1.2. Morphology 12
2.1.3. Irradiation and hydrogenation 14
2.1.4. Stabilization of ODS steels by inclusion of Ti precipitates 16
2.2. Theoretical simulations on O-, Y- and Ti-containing precipitates in Fe lattices 18
2.2.1. Atomistic simulations of ODS nanoparticles formation in α-Fe 18
2.2.2. Simulation of ODS cluster formation in α-Fe based on ab initio calculations 20
2.2.3. Ab initio calculations on high-temperature paramagnetic γ-Fe with impurities 23
3. First principles calculations using VASP code 25
3.1. Fundamentals 25
3.2. Basic principles of DFT method 26
3.3. Periodic solid structures and plane-wave formalism 28
3.4. Simulation of equilibrium doped lattice and defect migration trajectories 31
3.5. Application of pseudopotentials for construction of PW basis set 32
3.6. Computational parameters used in the VASP calculations 33
4. Verification of *ab initio* calculations on simplest γ-Fe models 35
4.1. Perfect *fcc*-iron lattice 35
4.2. fcc-iron lattice containing single point defect *per* supercell 36
5. *Ab initio* calculations on multiple-wise defects in γ-Fe models 40
5.1. Pairwise defects 40
5.2. Multiple-wise V_{Fe}-vacancy cluster reducing barrier for Y_{Fe} migration 44
5.3. Atom-substituted triple-wise defects 47
5.3.1. Y_{Fe}-O-Y_{Fe} configurations 47
5.3.2. Ti_{Fe}-O-Ti_{Fe} configurations 52
5.3.3. Ti_{Fe}-O-Y_{Fe} configurations 56
6. Summary 61
7. Main theses 62
8. Literature 63
8.1. Author's publications related to this work 63
8.2. Other author's publications 63
8.3. References on regular publications for PhD Thesis 63
9. Contributions at scientific conferences 67
Acknowledgements 71

Abstract

The oxide dispersed strengthened (ODS) steels are considered as the promising structural materials for future fusion reactors. The implementation of ODS steels allows increasing the operating temperature of the reactor by 100°C, which noticeably improves its efficiency. Both size and spatial distribution of the yttrium oxide particles, which can include, *e.g.*, Ti atoms naturally distributed in steels, affect the mechanical properties of the ODS steels and their radiation resistance. However, the mechanisms of oxide particle formation in ODS steels are not fully understood yet.

The detailed modeling of the defect in the face centered cubic (*fcc*) Fe lattice has been performed using the DFT PAW (Density Functional Theory Projector Augmented Wave) method as implemented in the VASP computer code. Within the framework of this work the calculations of single vacancy, O, and Y impurities have been performed. Pair-wise interactions between vacancy, O, and Y have been calculated along with the assessment of the binding energies between these defects. The interactions between multiple defects have also been calculated. Migration barriers have been assessed using the NEB (Nudge Elastic Band) method. Due to an initial presence of low-concentration Ti impurities in steels, which can form both TiO and YTiO precipitates, additional first principles calculations on the corresponding models have been carried out too. The results of performed calculations reveal the major factors contributing in the formation of the ODS steels.

Keywords: ODS steels, *fcc*-Fe, first-principles DFT PAW calculations, binding energy

List of abbreviations (Glossary)

1D	one-dimensional
2D	two-dimensional
3D	three-dimensional
AE	all-electron
APT	atom probe tomography
at.%	atomic percent
bcc	bulk centred cubic
CRPP	Centre de Recherches en Physique des Plasmas (The Swiss Plasma Center), Lausanne
DFT	density functional theory
dpa	dispacement *per* atom
EUROFER	The name of the material developed by the Karlsruhe Institte for Technology
fcc	face centred cubic
GGA	generalised gradient approximation
HLRS	High performance computing center Stuttgart
HIPing	hot-isostatic pressing
HRTEM	high resolution transmission electron microscope
LDA	local density approximation
LKMC	lattice kinetic Monte-Carlo
LMC	lattice Monte-Carlo
MEP	minimal energy path
MSM	magnetic sample method
NEB	nudge elastic band
NN	nearest neighbour
ODS	oxide dispersed strengthened
PAW	projector augmented wave
PS	pseudo-wave soft
PW	plane waves
PW91	Perdew-Wang exchange-correlation functional
RAFM	Reduced activation ferritic-martensitic
SANS	small angle neutron scattering
SEM	scanning electron microscope
SQS	special quasi-random structure
TEM	transmission electron microscope
VASP	Vienna *ab initio* Simulation Package
wt%	weight percent

1. Introduction

1.1. Motivation

Oxide dispersed strengthened (ODS) structures of reduced activation Cr-containing ferritic-martensitic (RAFM) steels (Figures 1.1 and 1.2) are considered as promising materials for applications in fusion reactors [1]. Use of the ODS steels strengthened by Y_2O_3 precipitates (with partial inclusion of Ti atoms) instead of their non-strengthened counterparts permits to increase the operating temperatures of blanket structures by 100°C [2, 3]. Both size and spatial distribution of oxide particles significantly affect mechanical properties and radiation resistance of ODS steels which are produced by mechanical alloying for several tens of hours, followed by a hot isostatic pressing (hipping) at temperature around 1000-1200°C and pressure ~100 MPa.

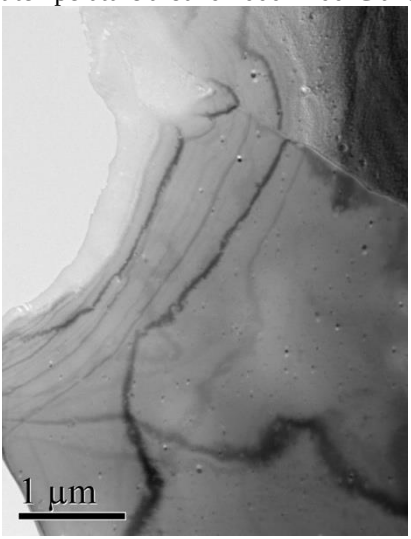

Figure 1.1. Transmission electron microscope (TEM) image of the ferritic steel.

Figure 1.2. TEM image of the martensitic steel (12.1 μm).

These conditions of synthesis correspond to predominance of the high-temperature *fcc*-Fe phase in low-chromium ODS steels (Figure 1.3).

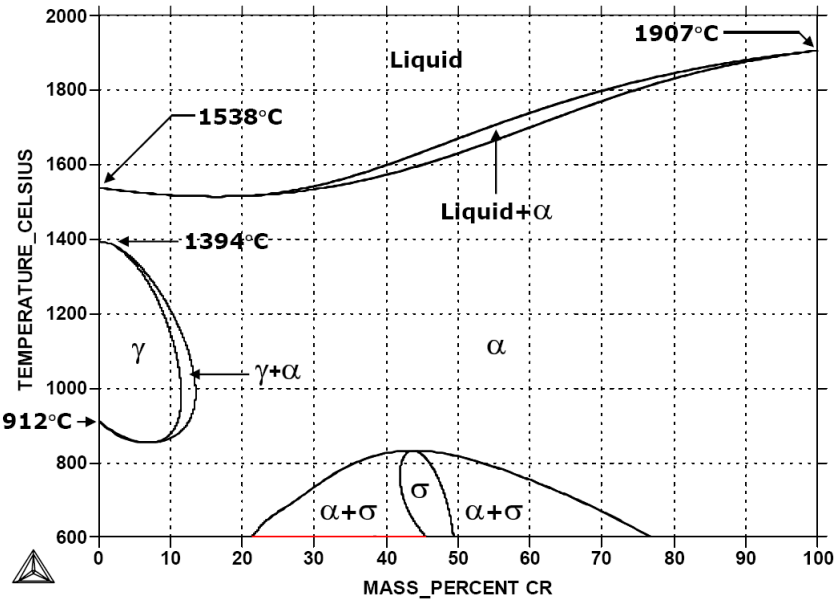

Figure 1.3. Phase diagram for RAFM steels depending on temperature and chromium concentration [4].

While the low-temperature α-Fe matrix was considered in a number of ODS studies performed so far, γ-Fe was not covered up to now at all. This is why, the main objective of this PhD Thesis is to understand the mechanism of ODS nanoparticle formation in *fcc*-Fe lattice. Io achieve this goal, it is necessary to perform the following tasks:

- Modeling of ideal *fcc*-Fe lattice in order to choose the proper parameters for the calculations of the defective structures.
- Modeling of single defects in *fcc*-Fe lattice (such as V_{Fe} vacancy, O atom in both interstitial and substitution positions as well as Y substitute atom), in order to check if the chosen calculation parameters are correct by comparing these results with those obtained in various experimental and other theoretical studies.
- Modeling of pair-wise interactions between vacancies, O and Y atoms in different combinations and at different mutual distances in order to obtain the binding energies between defects.
- Modeling of more complex defect clusters containing vacancies, O and Y atoms.
- Calculations of Fe vacancy self-diffusion.
- Calculations of possible migration barriers and trajectories for single O and Y atoms in the lattice.
- Due to initial presence of low-concentration Ti impurities in steels, which can form both TiO and YTiO precipitates, we have constructed their models and calculated them from the first principles.

These results obtained using *ab initio* calculations to be implemented results in lattice kinetic Monte-Carlo (LKMC) modeling in order to develop the model of the ODS particle formation.

Numerous experiments performed worldwide and, in particular, at the Department of Metallic Materials, Institute of Applied Materials, Karlsruhe Institute of Technology (Germany) have shown that the ODS samples with the best mechanical properties have quasi-homogeneous distribution of small (4-10 nm) yttrium oxide particles [5]. However, such a distribution of particles (Figure 1.4) is not always obtained in the experiments and the reasons for the non-uniformity are not yet well understood. Our study is aimed at elucidation of the atomic scale mechanisms for both nucleation and growth of Y_2O_3 nanoparticle. To understand these mechanisms, it is necessary to investigate the interaction of the yttrium solute atoms with the iron vacancies and the interstitial oxygen as well as their possible diffusion paths.

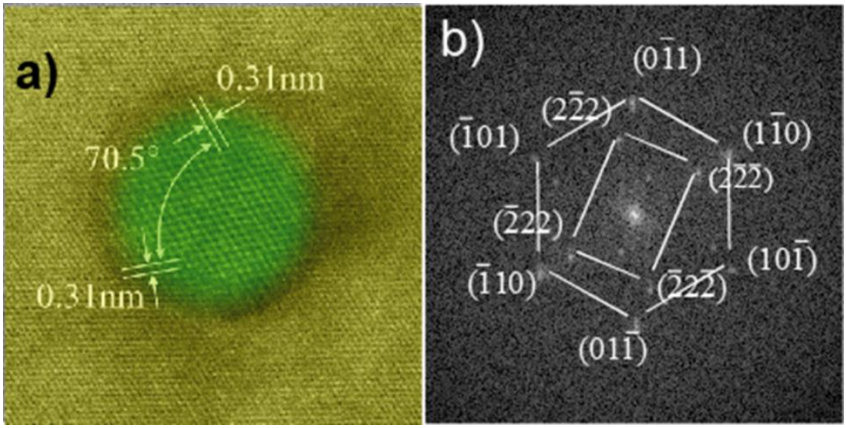

Figure 1.4. High resolution TEM (HRTEM) image of Y_2O_3 nanoparticle embedded into ferrite matrix (a) and its Fourier transformation (b) [5]. The parallel orientation between Fe (110) and Y_2O_3 (111) directions have been confirmed on a number of small ODS particles.

The current study is performed in a close collaboration between the Institute of Solid State Physics, University of Latvia, Riga (Latvia), and the Institute of Applied Materials, Karlsruhe Institute of Technology, Karlsruhe (Germany) supported by H2020 EUROFUSION project (Enabling Research subproject AWP15-ENR-01/UL-01).

1.2. Author's contribution

Results of the calculations described in this PhD thesis are summarized in six high-ranking international publications [P1-P6] as well as presented at local and international conferences (45 oral and poster presentations). The author has been chosen as the corresponding author in publications [P1-P4] and has performed

all the calculations and their analysis reported in all six papers, as well as he played the major role in planning and writing the papers, conference abstracts, and presentations. Additionally, he is the author of six papers published in prestigious scientific journals within the other projects. The detailed author's contribution in the [P1-P6] publications is as follows:

[P1] **A. Gopejenko**, Yu.F. Zhukovskii, P.V. Vladimirov, E.A. Kotomin, and A. Möslang, *Ab initio* simulation of yttrium oxide nanocluster formation on *fcc*-Fe lattice. – *J. Nucl. Mater.* 2010, **406**, p. 345–350. (70% of the planning and writing; all calculations presented in the paper, corresponding author responsibility)

[P2] **A. Gopejenko**, Yu.F. Zhukovskii, P.V. Vladimirov, E.A. Kotomin, and A. Möslang, Modeling of yttrium, oxygen atoms and vacancies in γ-iron lattice. – *J. Nucl. Mater.* 2011, **416**, p. 40-44. (70% of the planning and writing; all calculations presented in the paper, corresponding author responsibility)

[P3] **A. Gopejenko**, Yu.F. Zhukovskii, P.V. Vladimirov, E.A. Kotomin, and A. Möslang, Interaction between oxygen and yttrium impurity atoms as well as vacancies in *fcc*-iron lattice: *Ab initio* modeling. – Proc. NATO ARW „Nanodevices and Nanomaterials for Ecological Security" (Eds. Yuri N. Shunin and Arnold E. Kiv; Springer: Dordrecht, Netherlands) 2012, p. 149-160. (70% of the planning and writing; all calculations presented in the paper, corresponding author responsibility)

[P4] **A. Gopejenko**, Yu.F. Zhukovskii, E.A. Kotomin, Yu.A. Mastrikov, P.V. Vladimirov, V.A. Borodin, and A. Möslang, *Ab initio* modelling of Y–O cluster formation in *fcc*-Fe lattice. – *Phys. Status Solidi B,* 2016, **253**, p. 2136-2143. (70% of the planning and writing; all calculations presented in the paper, corresponding author responsibility)

[P5] **A. Gopejenko**, Yu.A. Mastrikov, Yu.F. Zhukovskii, E.A. Kotomin, P.V. Vladimirov, and A. Möslang, *Ab initio* modelling of the Y, O, and Ti solute interaction in *fcc*-Fe matrix. - *Nucl. Instrum. Methods Phys. Res. B* 2018, **433**, p. 106-110. (70% of the planning and writing; all calculations presented in the paper, corresponding author responsibility)

[P6] V.I. Gopeyenko and **A. Gopejenko**, Using applications and tools to visualize *ab initio* calculations performed in *VASP*. - In a book: "Augmented Reality, Virtual Reality, and Computer Graphics". Lecture Notes in Computer Science (Eds. L.T. De Paolis and P. Bourdot; Springer International Publishing AG, Cham, Switzerland), 2018, Part I, p. 489-496. (90% of the planning and writing; all calculations presented in the paper)

1.3. Scientific novelty

The problem of theoretical modeling of ODS particle formation in RAFM steels is very complex as it requires a two-step approach. The first step is an *ab initio* modeling of different defects (vacancies, O, Ti and Y atoms) in *fcc*-Fe lattice. Ideal iron lattice was chosen as the base model as it is considered that Cr atoms and other impurity atoms do not play decisive role in the formation of ODS particles. The main objective of this step is calculations of the parameters necessary for the future modeling to be performed using LKMC method. That step will allow one to understand the formation of ODS particles and their growth.

Within the framework of this doctoral thesis the model basing on the paramagnetic fcc-Fe lattice has been considered for the first time. As compared to other theoretical studies performed so far, *e.g.*, considered in Subsection 2.2, where the models used for *ab initio* simulation have been based on predominantly ferromagnetic *bcc*-Fe lattice. The idea to include modeling on γ-iron lattice is based on the fact that during the production at temperatures of around 1100-1200°C the ODS steels with the Cr concentration lower than 12% (9% in the case of EUROFER 97) undergo *bcc* to *fcc* phase transformation (Figure 1.3), thus, ODS particles are predominantly formed in the *fcc*-Fe phase. Additionally, since titanium can exist as natural impurity in ODS steels [2], its presence in iron lattice does not result in the marked reconstruction of the latter, structurized either in *bcc* or *fcc* phase.

2. Literature review

2.1. Experimental study of ODS nanoparticles formation in RAFM steels

Reduced activation ferritic-martensitic steels are promising structure materials for future fusion reactors possessing better thermal conductivity, higher swelling resistance and lower damage accumulation than austenitic steels [6]. Also, these materials were developed to reduce the pollution and to decrease the requirements for the facilities of the waste storage of the radioactive structures of the fusion reactors after service. Some elements that are contained in martensitic steels were substituted by other elements with faster decay of the induced radioactivity. Initially, the content of Cr in RAFM steels (EUROFER) was limited to 9%, required for the corrosion resistance and leads to the lowest ductile–brittle transition temperature (DBTT) during the impact tests. Chromium content above 12% leads to the transformation to δ ferrite and to the Cr α′ at low temperatures under irradiation that result in the decrease of the impact toughness. The highest operation temperatures for the RAFM steels was achieved earlier to be 550°C, however, to improve the reactor efficiency the higher operating temperature is required. Both ferritic martensitic ODS steels with ~9% Cr wt.%

and ferritic ODS steels with ~13-14% Cr wt.% concentration are of the high technological interest and are now being widely studied.

One of the most widespread oxides used to reinforce steels is Y_2O_3 [8, 9] stability of which was tested under electron and neutron irradiations. The RAFM steels strengthened by ODS are being tested to evaluate the possibility of their implementation at temperatures instead of standard RAFM steels in combination with their advantages. ODS RAFM steels have better tensile and creep properties as compared to the latter. These properties are improved due to the dislocations that are caused by the dispersion of the nanooxides during the reinforcement of the RAFM steel by Y_2O_3 oxide. Moreover, RAFM steels strengthened by $MgAl_2O_4$ were found to exhibit even better properties than those strengthened by Y_2O_3 [6]. Further improvement of its efficiency requires deep understanding of basic mechanisms of oxide particle nucleation and growth.

2.1.1. Manufacturing of ODS steels

ODS steels are usually produced in two steps, the first of which is mechanical alloying (MA) of the reinforcing particles with the base metal in the form of atomized powder, followed by hot isostatic pressing (HIPping). MA foresees a solid-state synthesis implementing ball milling process (Fig. 2.1) in argon atmosphere to avoid oxidation.

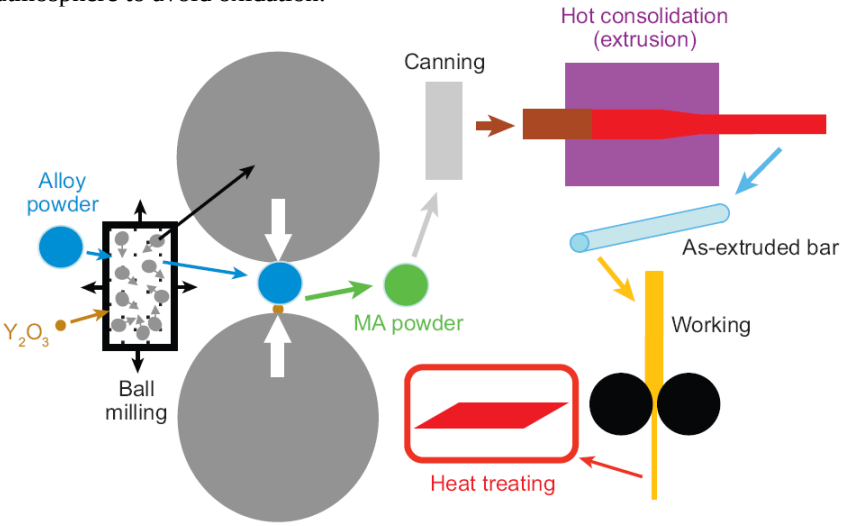

Figure 2.1. Stages of mechanical allowing of ODS steel powder [8].

To produce the materials with better properties and stability at increased temperatures homogeneous distribution of oxide nanoparticles is required. However, as MA is a very complex process in order to achieve the best performance properties since a number of variables need to be controlled. Such

properties as grain distribution, contamination of the milled powders depend on such variables as milling time, process control agent, ball to powder weight ratio, milling atmosphere, *etc.* [8]. On the other hand, HIPping allows avoiding the formability and anisotropy problems. As it is more thermodynamically stable then nitrides and carbides and one of the most stable oxides yttria is used for the reinforcement. During mechanical alloying small amounts of Ti are added as they refine the dispersion of reinforcing oxide on reprecipitation during HIPping. The precise control of O, Ti and C content during the production of ODS steels is important as the contamination by foreign elements has harmful effect on the mechanical properties [9]. ODS particles found after HIPping are the remnants of initial oxide powder that are formed during MA. This may be supported by the fact that the HIPping temperatures are lower than yttria melting temperature so thermal process does not occur during the oxide particle transformation. There are experimental evidences that after milling a noticeable part of Y and O atoms can be decomposed from yttria clusters in steel matrix with concentrations above their equilibrium solubility [10]. In this case, the precipitation of Y_2O_3 nanoparticles can occur already at the hipping stage as a result of yttrium-oxygen co-precipitation.

2.1.2. Morphology

The structure of Y_2O_3 particles in alloy lattice was analysed using HRTEM method (Fig. 1.4) [5]. In addition to the extensive investigation of mechanical properties of ODS materials it is also necessary to examine the crystalline structure of the ODS particles and its orientation with respect to the alloy matrix as this knowledge is important to improve the mechanical properties ODS alloys because the lattice coherency of the particles is important for their strengthening in steel. Before that structural study the relationship of crystallographic orientation was established between metal oxides, carbides or nitrides and metallic matrix. It was caused by the growth of the precipitates during HIPping process and was not observed between the metal matrix and the ODS nanoparticles earlier formed in it. The main reason for the orientation relationship between the particles was the interaction between these particles and metal matrix during their growth or solidification. Therefore, the objective of that work was to find if the orientation relationship exists between yttria particles and surrounding metal matrix as well to determine whether it occurs during the mechanical alloying or during the HIPping stage of the production.

The crystallographic structure of the EUROFER-ODS material at room temperature corresponds to α-Fe with *bcc* structure and a lattice constant of 2.87 Å while the Y_2O_3 powder has crystalline *bcc* structure with lattice constant 10.6 Å. This crystallographic structure was also observed for the ODS particles embedded in the metal matrix [5]. The size of each particle was found to be within the range of 3 to 45 nm with average size of 12 nm (nanoparticle size of 3 nm is the smallest size that is possible to find using TEM which resolution is

$4\times10^{21}m^{-3}$). The nanoclusters considered as the precursors of the ODS particles containing various solute atoms (V, Cr, Ta, C and N together with the elements of iron matrix in many cases) including oxide forming elements with the sizes ~2 nm were observed [11]. Usually the particles have spherical shape and the particles with the size larger than 12 nm tend to have a well-established faceted surface [5]. The strong relationship of the crystallographic orientation yttria particles with alloy lattice was found. The following orientation relationships were found for a large number of particles (but not for all of them): [110] YO ∥ [111] FeCr and $(1\bar{1}\bar{1})$ YO ∥ $(1\bar{1}1)$ FeCr (Fig. 1.4). Thorough analysis of the preparation steps suggests that orientation relationship occurs after the HIPping. Yttria particles are in the solid state during HIPping as the melting point of yttria is ~2500° C which might be slightly reduced in particles with the size smaller than 15 nm thus meaning that the particles should not be in the liquid state during HIPping. However, it is possible that yttria particles in solid state may change their crystallographic orientation [5]. Surface diffusion leads to the minimization of surface energy and the formation of spherical or faceted particles. The experimental findings suggest that the orientation relationship of ODS particles and the matrix most likely evolves during the HIPing process.

Unlike the model suggested in Ref. [5] that foreseen the formation of the single-phase yttria dispersoids, Klimenkov *et al* considered ODS particles as not single-phase dispersoids but more complex precipitate disposition [12]. It was observed that a shell consisting of V-Cr-O is formed around each of the ODS particles as well as 5-12% of Mn was detected inside yttria (earlier Mn was not detected in the ODS particles). The main objective of that study was to investigate if the chemical composition and the dispersion of ODS particles is influenced by minor alloying elements contained in the matrix. V-rich shell as well as the increased concentration of the Cr was found around the ODS particles. The Cr concentration around the ODS particle increased from 9 to 12-15 mass percent as compared to the average concentration in the matrix. This means that a uniform shell with V and Cr compositions can be formed around the ODS particle (the thickness of this shell is approximately 1.0-1.5 nm). The EELS spectra showed that Mn is detectable only in ODS particles but not in the alloy matrix. These techniques precisely determined the elemental distribution in relation to the location of different phases, the Y_2O_3 core, and V, Cr shell on the nanometer scale. It was clearly visible that Cr concentration increased around the particles but in the areas at the distance of 3-4 nm from the particles the Fe and Cr concentration did not change. The decrease of Fe concentration in ODS particle was estimated at ~70% while the Cr concentration around the ODS particle increased from 9 to 11-14% while inside the particle varied from 14 to 18%. In comparison to the average concentration level in the alloy matrix the Cr concentration is 40-70% higher in the ODS particle. In some areas of the matrix, the Cr concentration decreased to 8.2% which might be caused by the diffusion of Cr into the shell. This area exists in the prepared material which might clarify the mechanism of the shell formation around the particle. Presumably the ODS

particles and the shell can be formed either during the HIPping at 1150°C or during the cooling as ODS particles were not found in the mechanically alloyed powder. It was suggested that the areas with the decreased concentration of Cr mean that they are formed during the cooling at temperatures below 850°C when the Cr diffusion is significant and cannot minimize the concentration difference at the distance of several nanometers around the ODS particle. Also, due to the formation of the oxide shell around the ODS particles the excessive oxygen can be concentrated in this area which might have positive effect on the mechanical properties, however, these effects are not yet studied.

To investigate whether the lack of toughness of the material is an inherent property of the production process, the positron annihilation spectroscopy was used [13]. Voids with sizes up to ~25 nm were found using TEM in milled EUROFER and ODS-EUROFER after annealing while the behaviour of non-milled EUROFER was found to be different, *e.g.*, the formation of high density three-dimensional vacancy clusters was observed. The main conclusion of this study was that Ar atoms are absorbed during the mechanical alloying by the Y_2O_3/matrix interfaces that act as very strong and stable sinks for Ar and vacancies. These voids are one of causes of the embrittlement and poor impact toughness of ODS-EUROFER. Special investigation was performed whether it would be possible to improve the properties of the materials during the production varying the treatment methods [14]. The harmful effect of milling on the ductility but without qualitative increase in Charpy impact energy can be reduced by normalization treatments for EUROFER. However, normalization does not change neither the ductility nor the impact toughness of the tempered ODS-EUROFER. It was also found that oxygen intake produced by milling does not affect the decrease of ductility and impact toughness. TEM suggests that the embrittlement might be caused by the precipitation of the carbides during quenching after the HIPping.

2.1.3. Irradiation and hydrogenation

The knowledge of the irradiation effects on ODS steels are not well known yet, irrespectively on extensive studies [9]. Irradiation causes heavy hardening and reduction in uniform elongation already at the lowest doses in conventional ferritic-martensitic steels. The fracture properties significantly decrease below the ductile to brittle transition temperature which can shift above room temperature after irradiation. However, this material still suffers less from the irradiation as other metals such as stainless steels or pure *fcc* metals. At low doses, unidentified so-called black dots are observed using TEM, which can be interstitial clusters of 1 to 2 nm. At higher doses at ~300°C dislocation loops and nanocavities were observed. The dispersion evolution of the oxides is one of the concerns in ODS steels under the irradiation which should accumulate damages at lower rate than conventional ferritic-martensitic steels as oxide particles should trap radiation induced defects, *e.g.*, grain boundaries in microstructure.

No significant change in tensile strength of ODS steel occurred, however, 20% hardening and loss of ductility were observed under irradiation below 500°C. These results are better than those observed for conventional ferritic-martensitic steel. The DBTT is markedly increased, however, no swelling occurred. The absence or the significant reduction of ODS swelling in steels as compared to conventional steels is caused by the high density of ODS particles acting as trapping sites.

Ref. [9] describes the ODS studies of the irradiation effects on both Plansee and Centre de Recherches en Physique des Plasmas (CRPP) ODS steels as well as materials based on Fe alloys containing Cr, Mo, Ni, Ta and W). The latter were irradiated to 0.3, 1.0, and 2.0 displacements *per* atom (dpa) at 40°C. No significant change in mechanical properties was observed compared to the non-irradiated conditions. The hardening of the material was 20% and did not change with the increase of dose; the elongation of the material was almost unchanged. The CRPP ODS was irradiated to 1.0 dpa at 350°C. The elongation of the material decreased by 50%, slight hardening of the material was observed, similar to the hardening caused by radiation in EUROFER97. This means that the damage accumulation is caused by nanostructured microstructure rather than by oxide dispersion. This is caused by the fact that nanostructured material possesses high density of trapping sites such as grain boundaries and dislocations, which might drastically decrease the irradiation induced defect density. It was also found that irradiation temperature does not affect the hardening of the material. TEM analysis showed no change in the oxide dispersion in both ODS materials. At low irradiation temperature the induced defects mainly consist of the black dots, similar to those observed in the conventional ferritic-martensitic steels.

At 350°C dislocation loops develop in EUROFER and in ODS similar to those observed in ferritic-martensitic steels. A high density of nanocavities is observed in the CRPP ODS. The hardening of the material is also caused by the yttria particles and this fact should be considered in the analysis of the irradiation induced defects. These factors, namely, the irradiation induced defects and the yttria particle density and size were analysed. The density of the irradiation induced defects was found to be smaller than the yttria particle density, which might explain the facts that the irradiation induced hardening is low and that the change in total elongation in comparison to the conventional ferritic-martensitic steel is negligible. One more reason for the low irradiation effect is the following: yttria particles act as the trapping sites for radiation induced point defects. During the mechanical alloying process the increase of grain boundaries occurs, which also act as trapping sites for the radiation induced defects, caused by the reduction of grain size. It was also found that tempered ferritic-martensitic steels with the martensite morphology possess better radiation resistance than deeply recrystallized material, with equiaxed grains and low dislocation density, because of its high dislocation and lath boundary densities that act as sinks for radiation defects [9].

Irradiation effects on the microstructural stability of 14%Cr wt.% ODS steels were studied in Ref. [15]. The material was irradiated by Fe^{5+}, He^{+} and H^{+} ions at 600 °C to 30 dpa in order to simulate fusion relevant conditions. The results of the TEM analysis show that the size of the nanoparticles in the samples have increased during the irradiation, however they have maintained their composition and morphology. The major effect of the irradiation was the formation of the small bubbles in the matrix or was related to the nanoparticles. Recent study [16] clearly shows that under irradiation of ODS steel Cr preferentially diffuses towards and segregates at the $FeCr/Y_2O_3$ interface (Fig. 2.2) resulting in formation of amorphous oxide layer with external Y atoms partially substituted by Cr ones while further migration of the latter towards the ODS core is neglecting. Thermal and irradiation stability of the $FeCr/Y_2O_3$ interface was studied too.

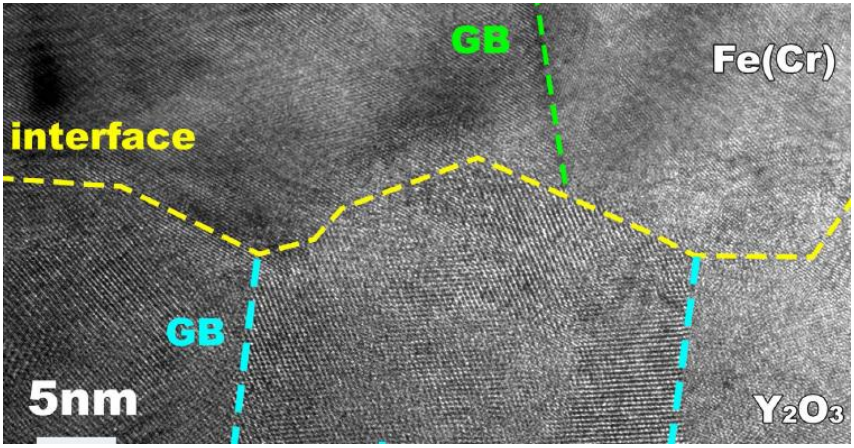

Figure 2.2. Grain boundaries (GB) around the $FeCr/Y_2O_3$ interface [16].

The effects of hydrogen loading on the microstructure of the EUROFER 97 and ODS-EUROFER have been studied in Refs. [16, 17]. It was found that ferritic-martensitic EUROFER strengthened by yttria nanoparticles uptake hydrogen much more when comparing with the conventional EUROFER 97. While the effect of the hydrogen on the yield stress and tensile strength is minor, it significantly reduces the elongation to the fracture of ODS-EUROFER if its concentration exceeds a certain level. It should be noted that both hydrogen and helium inhibition was confirmed experimentally in ODS steels.

2.1.4. Stabilization of ODS steels by inclusion of Ti precipitates

To analyze ferritic ODS steels, influence of Ti concentration on them was studied using SEM and TEM microscopies (this concentration was varied from 0 to 0.4 wt.%) [18]. Performed investigation revealed that Ti leads to formation of

spherical titanium oxides as opposed to chromium oxides due to the stronger Ti affinity to O. The hardness grows with the increase of Ti concentration (its optimal value was found to be 0.3%). While ferritic steels have an advantage over ferritic-martensitic steels in term of tensile strength their disadvantage was found to be higher temperature ductility.

Chemical and microstructural evolution of ferritic ODS steels containing Ti impurities was analyzed for samples containing 14% Cr [18]. The study revealed that carbon content significantly increases as well as oxygen decomposition from yttria during mechanical alloying, N and O contamination was observed during milling. Ti-enriched precipitates were found using microprobe analysis and TEM. Annealing effects on microstructure of ferritic-martensitic steels were considered as important structural transformations occurring during annealing [19]. X-ray evaluation of dislocation density in ferritic-martensitic steels showed that it is a martensitic transformation that leads to a high dislocation density in ODS-EUROFER steels [20].

Extensive analysis of spatial distribution, morphology, structure and chemical composition of different precipitates in EUROFER 97 was performed using TEM analysis [21] which detected presence of $Mn_{23}C_6$, TaC, VN and TiN precipitates. An investigation of such properties as hardness, the morphological and crystallographic anisotropy and the nano-precipitation size evolution has been performed to improve the fabrication methods of ferritic-martensitic ODS steels [22]. The study showed the importance of $\alpha \rightarrow \gamma$ phase transformation to reduce the morphological and crystallographic anisotropy caused by the manufacturing process.

The influence of Y on the microstructural and mechanical properties of the ferritic ODS steels enriched with Ti wt.% has been studied elsewhere [23]. Y has been added as an elemental powder with the particle size of < 45 μm. When being initially as an impurity in Y powder, Si might be also competing with Ti during the nucleation of the oxides. It was found that after heating the material to the temperature ~1300°C the significant softening occurs at room temperatures. Deformation and damage mechanisms of ferritic ODS steels (12% Cr wt.%.) under high temperature (550-650°C) cyclic loading were studied too possessing four distinct stages during the material tensile tests [24]: cyclic softening, cyclic hardening, continuous linear cycling softening, as well as initiation of fatigue crack. The first stage occurs due to the free movement of free dislocations and their rearrangement. During the hardening the dislocation density is increased, while a softening leads to the clustering of the dislocations, mutual annihilation of the dislocations as well as appearance of microcracks, due to the damage at previous stages. The cracks were initiated on the surface and the oxidation assisted both the crack initiation and propagation. High temperature low cycle fatigue tests have been performed on austenitic ODS steels with 15-17% Cr wt.%. The observed cyclic hardening is lower than in non-ODS steels. Zr-rich zones, which might affect the fatigue life of the material found on the fracture surfaces.

The effects of sintering temperature on the microstructure and mechanical properties of the 14% Cr wt.% ferritic ODS steels were studied elsewhere [25]. As TEM observations of them showed, there are two kinds of oxides appear in spark plasma sintering (SPS) ODS steels: high-density nanoscale Y–rich oxides $Y_2Ti_2O_7$ and coarse Cr-rich $TiCr_2O_4$ oxides, tensile strength of which decreases with the increase of the sintering temperature. The latter grew from 950°C to 1025°C during the study and showed simultaneously that the average grain size increased from 260 to 2420 nm. The effects of N on the ferritic-martensitic ODS steel reinforced by Ti layers were studied too [26]. The material has been manufactured by putting the powder and Ti discs alternately into the graphite dyes and then sintered. Both ODS and ODS/Ti steels with different concentration of N were sintered by spark plasma sintering. It was found that 0-0.2% wt.% N ODS steels exhibit inferior tensile properties compared to the pure ODS steels while 0.5% wt.% N has a very high tensile strength. The former is caused by the inter-diffusion of the elements across the interface, while in the latter a thick continuous Ti(C, N) layer is formed, limiting the inter-diffusion.

2.2. Theoretical simulations on O-, Y- and Ti-containing precipitates in Fe lattices

According to phase diagram of steels (Fig. 1.3), α-Fe phase is the most widespread for the Cr-free iron solid structures in the temperature intervals $T < 912\ ^{o}C$ and $1394\ ^{o}C < T < 1538\ ^{o}C$. Thus, it is not surprising that so far, majority of theoretical simulations on several-atom ODS fragments incorporated in iron lattice were performed during last two decades on periodic *bcc*–Fe supercells.

2.2.1. Atomistic simulations of ODS nanoparticles formation in α-Fe

In addition to the results obtained in the abovementioned experimental studies, various theoretical simulations clearly show that a presence of titanium atoms reduces the size of Y_2O_3 clusters when transforming them to $Y_2Ti_2O_7$ or Y_2TiO_5 [27]. These apparently coherent transition phases are precursors to equilibrium phase distinguished by a low O/Me ratio. For better understanding the nature of non-equilibrium features, the Lattice Monte Carlo (LMC) simulations of the nanocluster (NC) composition and structure were performed [28]. In earlier studies, a rigid body-centered cubic lattice was fixed in all the simulations at fixed lattice positions taken into account only first nearest neighbor bonds for metal–metal (Fe–Fe, Y–Y, Ti–Ti, Fe–Y, Y–Ti and Fe–Ti) interactions, first and second nearest neighbor bonds for metal–oxygen (Fe–O, Y–O and Ti–O) interactions, and up to fifth nearest neighbor bonds for O–O interactions where oxygen atoms were placed on the octahedral interstitial sublattice. To estimate pairwise bond energies, LDA-DFT calculations were performed using SEQUEST code [29] in order to obtain the potential energy *per* atom as a function of atomic volume (Fig. 2.3) where alloy concentration served for

developing full potentials within either Rose's equation of state [30] or the Lennard-Jones framework [31].

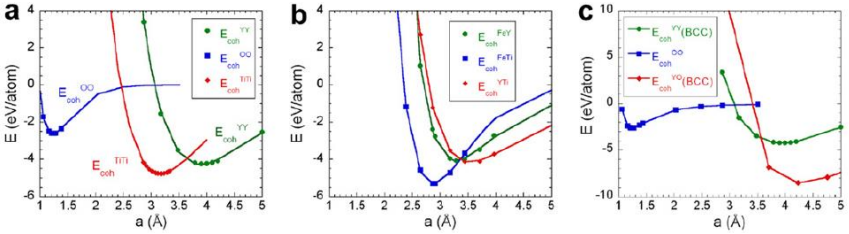

Figure 2.3. LDA-DFT results of the cohesive energy as a function of lattice parameter (data points) and fits (solid lines) to the LDA calculations based on Rose's equation of state (YY, TiTi, FeY, FeTi, YTi, YY, YO) [30] or a Lennard-Jones functional form (O–O) for: (a) *bcc* Y, Ti and molecular O_2 (as a function of bond length), (b) *bcc* Fe–Y, Fe–Ti and Y–Ti as well as (c) *bcc* Y, Y–O and molecular O_2 [27].

Fig. 2.4 shows the effect of increasing the bulk oxygen content of the simulated nanocluster in α-iron from 0.25 to 1.5 at.%, which leads to decreased Y content in the NC, at nearly constant Ti concentration. The NCs consist of segregated Y and Ti rich regions, with a nearly uniform oxygen concentration. The reduced Y content in the nanoclusters with increased bulk O concentration may influence NC thermal stability, and is reasonably consistent with the earlier finding that oxygen excess had a significant effect on the recrystallization temperature of nanostructured ferritic alloys (NFAs) [32].

Lattice strain energies E_{str} were not directly accounted for, which may be acceptable only for very small spherical clusters. However, E_{str} values were partly taken into account by imposing the Fe–Fe bond lengths on the dissolved O, Y and Ti solutes, rather than using their relaxed equilibrium Fe–Me lengths. To verify both structure and properties of Y-Ti-O NCs formed in the LMC, those were compared to data from small angle neutron scattering (SANS) and atom probe tomography (APT) measurements to be convinced if self-consistent structures and chemistries can be properly described [27]. When using the former method both magnetic and nuclear scattering cross sections provide information on both the composition and atomic density of nanoclusters, while the latter method provides direct measurements of their chemistry. The key issue is the NC and matrix strainenergies that are required to maintain coherency with the Fe lattice. It was found that the nanoclusters preferentially form pyroclore oxides phases, which occur at only slightly larger sizes (>5–6 nm), and what controls their subsequent thermal and radiation stability.

It was found that Y–Ti–O nanoclusters can be formed at all temperatures when the NC lattice parameter is larger than 1.2 a_o. The smaller nanoclusters were described as faceted polyhedrons of roughly spherical shape with compositions of 15–26%Y, 23–31%Ti and 45–65%O containing segregated regions that are Y or Ti rich, with nearly uniform O concentrations. The predicted NC for effective lattice parameters between 1.2 a_o and 1.3 a_o can be reasonably

consistent with the experimental observations when the matrix O concentration is less than 0.5 at.%. At a lattice parameter > 1.3 a_o, a significant strain energy contribution to the NC free energy was observed, in a correspondence with the experiment [28].

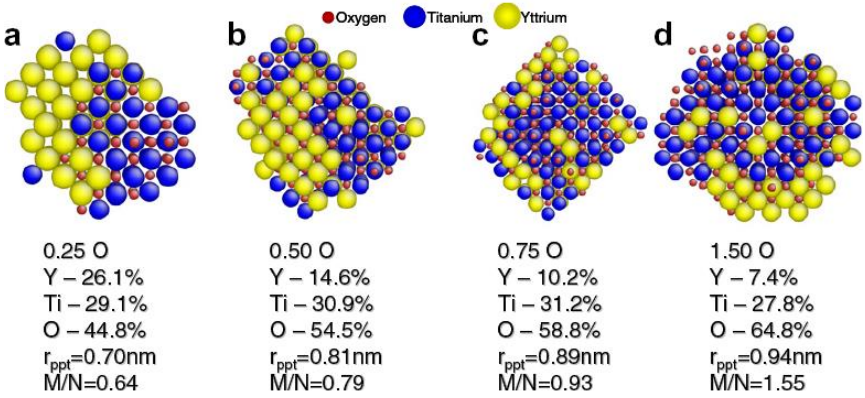

Figure 2.4. LMC simulation results showing the predicted NC structure, size (precipitate radius, r_{ppt}), composition and calculated M/N (magnetic to nuclear) scattering ratio as a function of alloy oxygen content in an Fe–0.47 at.%Ti–0.12 at.%Y alloy at 673 K and a NC lattice parameter of 1.3 a_o (where a_o = 0.287 nm is the lattice constant of *bcc*-Fe) [27].

Obviously, aforementioned LMC model was used to be clearly oversimplified, although the obtained results provided quite helpful atomic-level insight into the Y–Ti–O NCs and a basis for understanding the thermal and radiation stability. The next modeling efforts were focused on the partitioning of strain energy between the matrix and nanoclusters, while the interfacial structure was clarified by performing off-lattice relaxations using the full potential energy functions. Moreover, when including the effects of both off-lattice relaxation and highly non-equilibrium vacancy concentration on the precipitation kinetics essentially enhanced reliability of further simulations on the Y, Ti and O precipitates in ODS steels.

2.2.2. Simulation of ODS cluster formation in α-Fe based on ab initio calculations

Comprehensive atomistic simulations on ODS particles foresees multiscale two-stage computational scheme (a) large-scale first principles calculations on *bcc*-Fe lattice supercells containing single V_{Fe} vacancies, O, Ti and Y impurity atoms as well as their small aggregates; (b) calculations of kinetic parameters using lattice kinetic Monte-Carlo code (LAKIMOCA) based on *ab initio* estimates of both interatomic binding energies and migration barriers of solute impurity atoms, in order to describe precipitate nanocluster growth [33]. Unlike theoretical approach described in previous subsection 2.2.1, current models include vacancies of iron atoms V_{Fe}, (Figs. 2.5a,b) presence of which makes essentially

more probable the interlattice and substitutional migration of Fe, Ti_{Fe} and Y_{Fe} atoms (Fig. 2.5a) inside *bcc*-iron lattice (while alternative migration of oxygen atoms can be realized *via* interstitial octahedral (Figs. 2.5a,b). Moreover, Fu *et al*. stated that the formation of ODS nanoclusters is not possible at all without the direct assistance of V_{Fe} [34].

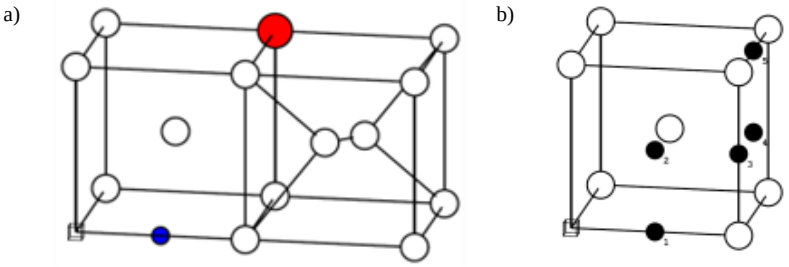

Figure 2.5. Different types of point defects in *bcc*-Fe lattice [33]: small transparent cube - V_{Fe} and transparent spheres – Fe (a, b); large dark spheres - substitutional atoms Cr_{Fe}, Ti_{Fe} and Y_{Fe} (a); small dark spheres – interstitial O atoms (a,b); dumbbell with self-interstitial Fe atom (a) [33]

On the other hand, Y-Ti-O precipitates, and especially the smallest Y_2TiO_3 nanocluster, do not require a vacancy to be stable [33]. Certain repulsion between Y_{Fe} and Ti_{Fe} is overcome by the strong attraction between these metal solutes to O atom, which can increase noticeably the binding energy. Moreover, presence of V_{Fe} vacancies can regulate diffusion of Y atom possessing larger diameter as compared to other atoms of precipitate. Additional study is required to determine if a high O contents is or not an obstacle for growth of Y-Ti-O precipitates, since due to the high binding energy between V_{Fe} vacancy and O atom, the former can be considered as an oxygen sink. As shown by us recently [Q5], vacancies strengthen stability of Y-O nanoclusters in the *bcc*-Fe lattice since Y solute atoms can be stabilized in the host matrix by vacancies since yttrium migration occurs in multiple steps by the vacancy mechanism. Clusters with 2 and 1.5 vacancies *per* Y solute atom provide conditions to create Y-O bixbyite-type bonds.

In order to understand the role of quasi-coherent interfaces around ODS nanoparticles, *ab initio* calculations have been also performed to investigate structural, energetic and electronic properties of the {100}<100>Fe//{100}<100>Y_2O_3 interface as well as their interaction with point defects [35]. For O monovacancy in the Y_2O_3 layer, its formation energy slightly increased when approaching to interface, while for V_{Fe}, the vacancy formation energy decreased when it arranged close to the interface. Obtained results suggest that the α-Fe/Y_2O_3 interface tends to attract V_{Fe} vacancies, preventing formation of interfacial voids, which enhances radiation resistance of ODS steels. On the other hand, with increasing number of V_{Fe} vacancies, structural morphology becomes more and more complicated [36]. Calculations on different ODS configurations in α-Fe lattice create database consisting of

binding energies is a solid ground to further establishment of a multi-element interaction model for a kinetic study.

Since all potential ODS steels contain large enough amounts of Cr_{Fe}, this element was also included in the extensive calculations performed so far [36-38], although it does not actively take part in ODS interatomic bonding [16] (Fig. 2.2). Increasing the interaction range considered up to the fifth nearest neighbour (5NN, corresponding to one diagonal the primary body-centred cubic cell) is also of prime negligible at these distances, thus, the Cr–Cr interaction is a long-ranged [39, 40]. Accordingly to the results reported in Refs. [36, 37], Cr, Ti and Y were found to stay in substitutional positions (Fig. 2.5a), while oxygen impurity atom was found to be the most stable in octahedral position of *bcc*-lattice (Figs 2.5a,b). A self-interstitial atom (SIA) in *bcc* Fe or FeCr is most likely to form a dumbbell around a regular lattice position (Fig. 2.5a), in a (110) plane [36]. Additionally, using density functional theory and nudged elastic band method for optimization of migration trajectory [41], Murali have calculated the diffusion coefficients of Fe, Y, Ti and Zr [38] by the vacancy mechanism using the nine frequencies model of Le Claire [42]

The ultra-high density of oxide nanoclusters in the ODS steels ensure trapping of helium atoms (after their He^+ irradiation as mentioned in subsection 2.1.3) in small bubbles and prevent dislocations from moving [43]. Large-scale first principles calculations clearly demonstrated that Y_2O_3 particles in ODS steels have a higher He solubility than the Fe matrix [44], which is primarily the result of larger interstitial sites. The solubility at oxide-iron interfaces around ODS nanoparticles is obviously larger than that in the bulk oxides. Strain fields, which can affect in particular the iron matrix, lead to solubility gradients near oxide-iron interfaces. Results obtained provide not only valuable insight into the behavior of He in ODS steels but also can be used to derive parameters for rate equation models of He sequestration in ODS steels. In the case of *ab initio* simulations on $Y_2Ti_2O_7$ nanoparticles in ODS steels the helium trapping effect was found to be even more pronounced [45] than for yttria clusters [44].

In general, the current level of simulations on ODS cluster formation in α-Fe based on *ab initio* spin-polarized calculations is found to be quite comprehensive. Three stages of the (Y, Ti, O) oxides appearance are of peculiar interest: the formation, the stability under normal conditions, and the stability under irradiation. To achieve such a goal, the interactions between each steel component have to be described. Analyzing the cohesive energies of Cr, Ti, Y and O impurities in different positions of a *bcc*-Fe matrix enables to deduce the most stable one [33]. High precision of energies calculated for interatomic distances up to the 5 NN (at which the interaction becomes weak enough to be neglected) must be provided. They will give information about the composition and the geometric configuration of the ODS clusters. The migration energies of a substitutional atom by the vacancy diffusion mechanism and of interstitial atoms must also be calculated to be able to simulate the kinetics of the system. All these data can be calculated using the VASP package. Implementation of the

obtained results in LAKIMOCA demands the evolution of α-Fe lattice containing defects after metal alloying. The idea is to run simulations covering a broad spectrum of initial compositions in order to determine the influence of each component. Reliable formation of nanoclusters would be a validation of the entire study, whereas not observing it would mean that a better model has to be found. Still using LAKIMOCA, and starting from a configuration with clusters, their stability will be studied during reactor lifespan timescales.

At the same time, a generalized *ab initio*-based model has been recently developed in order to study the thermodynamics of multi-phase and multi-component systems [46]. Beyond previous approaches, such a model foresees the inclusion of the defect exchange between different phases controlled by the equivalent chemical potentials of the same atomic species in all phases. This model enables calculation of the equilibrium defect concentrations in each phase provided that their zero-temperature internal energy changes are due to particularly known defects, input parameters for which were obtained from large-scale spin-polarized DFT calculations. The following defects: vacancies in both Y_2O_3 and *bcc*-Fe phases, Y substitutes and O interstitials in iron lattice, Fe impurities and antisite defects in Y_2O_3, were included in the thermodynamic equilibration. The corresponding equilibrium concentrations were estimated as a function of temperature and the fraction of yttria. Compared to both the lattice and object KMC approach, the proposed model gives a possibility to include the global equilibrium in multi-phase systems [46]. Its advantage over the models based on a lattice approach or empirical potentials is in a more accurate defect energetics, used as input parameters, and calculated within the DFT technique. Considered model does not include inter-phase interfaces; however, it can be applied easily by extending new types of defects and the areas included. For example, the nanoparticle–matrix interface can be introduced as one more phase (region) in the system such as $(Y_2O_3)_x(\text{interface})_y(bcc\text{-Fe})_{1-x-y}$ with specific values of energy change occurring due to defects near the interface [47], where its fraction, *y*, can be defined by relationships between the number of atoms in the interface and the total number of atoms in the whole system, being dependent on the interface properties (*e.g.*, the thickness) and the particle size.

2.2.3. Ab initio calculations on high-temperature paramagnetic γ-Fe with impurities

In previous Subsection, earlier performed first-principles simulations on magnetically-ordered low-temperature α-Fe lattice containing ODS precipitates have been analyzed based on the formalism of large-scale spin-polarized calculations. To simulate paramagnetic γ-Fe (austenite) lattice containing both substitutional and interstitials impurity atoms, both host and defective lattices were recently studied using a couple of approaches applied to PAW-GGA DFT method [48]. The paramagnetic state was modeled by a supercell realization of

the disordered local moment (DLM) model introduced by Hubbard [49] and Hasegawa [50] in the framework of magnetic sample method (MSM) combined with the magnetic special quasi-random structure (SQS) approach. In the proposed technique, the magnetic SQS supercell was created for the host, *fcc*-Fe, and then calculations for impurities located at different positions of the supercell (C, N, Nb, V) were performed, followed by the averaging of the results as supposed by the MSM method. It was shown that the SQS-MSM approach gives estimations of solution enthalpies with accuracy similar to what is expected for first-principles calculations in magnetically-ordered and nonmagnetic materials [51]. Since the calculated and measured solution enthalpies were found to be small, relative deviations between them were significant for C and N impurities, while solubility products for corresponding carbides and nitrides in the paramagnetic state calculated with the proposed approach are in qualitative agreement with available experimental data. All the impurities, as found, can induce a local magnetic polarization of Fe atoms neighboring the impurity by the spin-flip (SF) transitions occurring at Fe sites located in the first coordination shell of the impurity atom. The SF transition is manifested by a change of orientation of a local magnetic moment during self-consistent iterations as compared to its original direction defined within the formalism of MSM-SQS supercell. Induced magnetization is especially pronounced for a carbon atom and can lead to a change of the magnetic structure in overcooled austenite. Additionally, for carbon, it was established a correlation between the occurrence of polarization and the decrease of solution enthalpy.

Obviously, for the current PhD study the aforementioned theoretical formalism looks too complicated in order to perform a series of large-scale calculations on ODS precipitates in *fcc*-Fe lattice. This is why we have simplified the computational scheme applied in the current study since paramagneticity means that at temperatures where *fcc*-Fe is stable in reality, the magnetic moments of iron atoms are disordered. The magnetic moments of individual atoms are certainly not static, however, change of their direction dynamically giving by averaging over sufficiently large volume a total magnetic moment equal to zero [P4]. An attempt to simulate such a behaviour using DFT methods would mean that for each defect configuration one is forced to calculate many configurations with various random magnetic moment orientations. Instead, we assume that such averaging would result in obtaining zero magnetic moments on the most of the atoms and perform non-magnetic calculations. Nonmagnetic approach might be not completely correct for all the cases, however, it gives practical way in order to estimate the defect binding energies and other properties necessary for modelling of yttrium oxide particle nucleation in **γ**-iron.

3. First principles calculations using VASP code

For large-scale *ab initio* calculations on O, Ti and Y impurity atoms as well as vacancies inside γ-Fe lattice, including simulation of their migration trajectories and formation energies of small clusters, we have used the *VASP* computer code, the commercial complex software package based on the density functional theory. Its computational procedure includes an iterative solution of Kohn-Sham equations, which is based on residuum-minimization and optimized charge-density mixing routines [52] as well as employs a plane-wave (PW) basis set combined with the Projector Augmented-Wave (PAW) scalar relativistic pseudopotentials [53]. Pair-, triple- and multiple-wise interactions inside the complexes of O, Ti and Y impurity atoms, V_{Fe} vacancies as well as energy barriers of their migration trajectories inside γ-Fe lattice to be used for further lattice kinetic Monte-Carlo simulations of Y_2O_3 and $Y_2Ti_2O_7$ clusters' growth.

3.1. Fundamentals

In an isolated stationary interacting system containing numerous electrons and nuclei, its properties can be determined by the many-body Hamiltonian $\hat{H}(\boldsymbol{r},\boldsymbol{R})$ consisting of kinetic energies of electrons $\hat{T}_e(\boldsymbol{r})$ and nuclei $\hat{T}_N(\boldsymbol{R})$, possible external potentials differently influencing on electrons $\hat{V}_e(\boldsymbol{r})$ and nuclei $\hat{V}_N(\boldsymbol{R})$, Coulomb potentials of interactions between only electrons $\hat{J}_{ee}(\boldsymbol{r},\boldsymbol{r}')$, only nuclei $\hat{J}_{NN}(\boldsymbol{R},\boldsymbol{R}')$, as well as electrons and nuclei $\hat{J}_{eN}(\boldsymbol{r},\boldsymbol{R})$ [54]:

$$\hat{H}(\boldsymbol{r},\boldsymbol{R}) = \hat{T}_e(\boldsymbol{r}) + \hat{T}_N(\boldsymbol{R}) + \hat{V}_e(\boldsymbol{r}) + \hat{V}_N(\boldsymbol{R}) + \hat{J}_{ee}(\boldsymbol{r},\boldsymbol{r}') + \hat{J}_{NN}(\boldsymbol{R},\boldsymbol{R}') + \hat{J}_{eN}(\boldsymbol{r},\boldsymbol{R}), \qquad (Eq.3.1.1)$$

where $\mathbf{r} = \{\mathbf{r}_i\}$ represents the set of all electronic coordinates and $\mathbf{R} = \{\mathbf{R}_k\}$ the set of all nuclear coordinates.

Due to a much smaller mass of electron m_e as compared to that of nucleus M_N, the motion of the former can be separated from that of the latter using the Born-Oppenheimer approximation (*adiabatic approach*) [20], which assumes that electrons respond instantaneously to the motion of nuclei and neglects the possible coupling between electrons and motion of nuclei (*e.g.*, vibrational one describing the phonon structure). In other words, the relaxation time of the electronic subsystem inside the isolated many-particle system is considered to be zero and the electrons are found to be in their so-called instantaneous *ground state*. For the electrons, on the other hand, the nuclear positions are fixed. With this adiabatic approximation, the original problem is simplified into many interacting electrons moving in an external potential field generated by all nuclei. Thus, it is possible to set up a perturbation series where in the first approximation order the degrees of freedom of electrons and nuclei are decoupled [55]. It means that the *wave function* $\Psi(\mathbf{r},\mathbf{R})$ describing a behavior of the whole many-particle system can be separated into the electronic and nuclear parts:

$$\Psi(\mathbf{r},\mathbf{R}) = \Psi_e(\mathbf{r},\mathbf{R})\,\Psi_N(\mathbf{R}). \qquad \textit{(Eq. 3.1.2)}$$

Obviously, the many-body Hamiltonian $\hat{H}(\boldsymbol{r},\boldsymbol{R})$ can be also decoupled into electronic $\hat{H}_e(\boldsymbol{r},\boldsymbol{R})$ and nuclear $\hat{H}_N(\boldsymbol{R})$ parts. In order to calculate the electronic structure of the system under study, one can use the electronic Hamiltonian:

$$\hat{H}_e(\boldsymbol{r},\boldsymbol{R}) = \hat{T}_e(\boldsymbol{r}) + \hat{V}_e(\boldsymbol{r}) + \hat{J}_{ee}(\boldsymbol{r}_i,\boldsymbol{r}_j) + \hat{J}_{NN}(\boldsymbol{R}_k,\boldsymbol{R}_l) + \hat{J}_{eN}(\boldsymbol{r}_i,\boldsymbol{R}_k). \qquad \textit{(Eq. 3.1.3)}$$

The Schrödinger equation for electrons containing the electronic wave function only can be written as [54]:

$$\hat{H}_e(\boldsymbol{r},\boldsymbol{R})\Psi_e(\boldsymbol{r},\boldsymbol{R}) = E_e(\boldsymbol{R})\Psi_e(\boldsymbol{r},\boldsymbol{R}). \qquad \textit{(Eq. 3.1.4)}$$

where the total electronic energy of system $E_e(\mathbf{R})$ can be used as a potential for the nuclei motion (*e.g.* vibrations around the equilibrium system configuration) in the corresponding nuclear Hamiltonian:

$$\hat{H}_N(\boldsymbol{R}) = \hat{T}_N(\boldsymbol{R}) + \hat{V}_N(\boldsymbol{R}) + E_e(\boldsymbol{R}). \qquad \textit{(Eq. 3.1.5)}$$

The Schrödinger equation for the nuclei subsystem can be written as:

$$\hat{H}_N(\boldsymbol{R})\Psi_N(\boldsymbol{R}) = E_N\Psi_N(\boldsymbol{R}). \qquad \textit{(Eq. 3.1.6)}$$

However, the many-electron problem described by *Eq. (3.1.4)* is still difficult to deal with, and one of the most efficient and successful approach for its solutions is based on density functional theory (DFT) [56].

3.2. Basic principles of DFT method

The origin of density functional theory goes back to Thomas and Fermi [57, 58] as well as their idea that the electron density for n occupied states and for the fixed nuclei configuration $\{\mathbf{R}\}$ can be expressed as:

$$\rho(\boldsymbol{r}) = n\sum_\sigma \int \Psi_e(\boldsymbol{r},\sigma;\chi_2;\chi_3;\ldots;\chi_n)\Psi_e^*(\boldsymbol{r},\sigma;\chi_2;\chi_3;\ldots;\chi_n)d\chi_2 d\chi_3\ldots d\chi_n, \qquad \textit{(Eq. 3.2.1)}$$

and contains essential information about the electronic system in the ground state. The variable $\chi_i = (\mathbf{r}_i,\sigma_i)$ represents the spatial $\mathbf{r}_i$ and spin σ_i degrees of freedom for arbitrary i^{th} particle, while $\int d\chi = \sum_\sigma \int d\boldsymbol{r}$. *Eq. 3.2.1* shows that the ground state of the electronic system is not described by a complicated wave function Ψ_e that depends on $3n$ spatial degrees of freedom and n spin components, but by an electron density $\rho(\mathbf{r})$ depending on three components of the vector $\mathbf{r}$ only.

The cornerstone of DFT was laid by the theorem of Hohenberg–Kohn (HK) [59], which suggests that the properties of a many-electron system in the ground state should be uniquely determined by the electron density $\rho(\boldsymbol{r}) = \rho(\boldsymbol{r},\boldsymbol{r}')$. The total energy of the electronic subsystem in the atomic system of units ($|a_{\text{H}}| = |e| = |m_e| = |\hbar| = 1$) can be written in this case as:

$$E[\rho(\boldsymbol{r})] = \int V_c(\boldsymbol{r})\rho(\boldsymbol{r})d\boldsymbol{r} + T[\rho(\boldsymbol{r})] + \frac{1}{2}\int \frac{\rho(\boldsymbol{r}\prime)\rho(\boldsymbol{r})}{|\boldsymbol{r}-\boldsymbol{r}\prime|} d\boldsymbol{r}'d\boldsymbol{r} + E_{xc}[\rho(\boldsymbol{r})], \qquad \textit{(Eq. 3.2.2)}$$

where the first term on the right side of equation describes the external potential created by nuclei (or cores) subsystem (plus possible influence outside the many-particle system), which determines the outside conditions for the electronic subsystem, for example, attraction of electrons to atomic nucleus with charges Z_j: $V_c[\rho(\boldsymbol{r})] = \sum_j \int \frac{Z_j\rho(\boldsymbol{r})}{|\boldsymbol{r}-\boldsymbol{R}_j|} d\boldsymbol{r}$corresponds to the operator of external potential $\hat{V}_c$; the second term describes the kinetic energy of electrons, operator of which is $\hat{T} = \frac{\partial^2}{\partial \boldsymbol{r}^2} = \nabla_{\boldsymbol{r}}^2$, the third term $J[\rho(\mathbf{r})]$ describes the electron–electron Coulomb repulsion, while the last term is called the exchange-correlation potential described by operator $\hat{v}_{xc}[\rho(\boldsymbol{r})] = \frac{\delta E_{xc}[\rho(\boldsymbol{r})]}{\delta\rho(\boldsymbol{r})}$ and included all other contributions, in particularly many-electron interactions.

By minimizing the energy functional $E[\rho(\mathbf{r})]$ over the electron density, the Kohn-Sham one-electron equations, expressed *via* the one-electron wave functions (orbitals) $\psi_i(\mathbf{r})$, determine the electron density as a constraint:$\rho(\boldsymbol{r}) = \sum_i^n |\psi_i(\boldsymbol{r})|^2$, while the discrete spectrum of one-electron energies (eigenvalues) ε_i, may be derived [60]. The Kohn-Sham equations are non–linear since all the potentials containing in them depend on the density $\rho(\mathbf{r})$ and, thus, on the orbitals. Therefore, Kohn-Sham equations have to be solved using the iterative self-consistence method.

For electrons, spin projections of which are defined as ±½, the total wave function of the electronic subsystem (possessing a fixed nuclei structure $\{\mathbf{R}\}$) is antisymmetric, due to Pauli principle, and can be expressed *via* Slater determinant of $\psi_i(\mathbf{r}_i)$ orbitals and normalization constant before it [61]:

$$\Psi_e^a(\boldsymbol{r}) = \frac{1}{\sqrt{n!}} det[\,\psi_1(\boldsymbol{r}_1)\ldots\psi_n(\boldsymbol{r}_n)]. \qquad \textit{(Eq. 3.2.3)}$$

Since the exact form of the exchange-correlation functional $\hat{v}_{xc}[\rho(\mathbf{r})]$ is not known, considerable methodical efforts were undertaken in order to create both relatively simple and proper functionals. Those of different complexity were developed within the hierarchy of DFT functionals. The simplest approximation is the local-density approximation (LDA) based on the exact exchange energy for a uniform electron gas, which can be obtained from fits to the correlation energy for a uniform electron gas [62, 63]:

$$E_{xc}[\rho(\boldsymbol{r})] \approx E_{xc}^{LDA} = \int \rho(\boldsymbol{r})\varepsilon_{xc}\,[\rho(\boldsymbol{r})]d\boldsymbol{r}, \qquad \textit{(Eq. 3.2.4)}$$

where $\varepsilon_{xc}[\rho(\mathbf{r})]$ is the exchange-correlation energy *per* electron in a uniform electron gas with density $\rho(\mathbf{r})$. In principle, the LDA approach works best for systems with slowly varying electron density and fails for very inhomogeneous cases like single atoms and surfaces. However, the LDA has been shown to be

very successful in describing various electronic systems including even very inhomogeneous ones [63].

Further improvement to the approximation of exchange-correlation energy resulted in various generalized gradient approximations (GGAs) [64, 65]. Although different in their detailed formulations, the GGA functionals essentially include the magnitude of the gradient of the electron density $\nabla_{\boldsymbol{r}}\rho(\boldsymbol{r})$ [65]:

$$E_{xc}[\rho(\boldsymbol{r})] \approx E_{xc}^{GGA} = \int \rho(\boldsymbol{r})\varepsilon_{xc}\,[\rho(\boldsymbol{r}), |\nabla_{\boldsymbol{r}}\rho(\boldsymbol{r})|]d\boldsymbol{r}, \qquad \textit{(Eq. 3.2.5)}$$

In the present study, we use the GGA formalism, which foresees that the electronic density is unevenly distributed: the highest density of electronic distribution is located around the atom nucleus. Possible simplification of different GGA approximations foresees that the exchange-correlation energy is expanded in the Taylor series depending on the electronic density degrees. If only the first order of expansion is taken into account the resulting expression contains an electronic density gradient $\nabla_{\boldsymbol{r}}\rho(\boldsymbol{r})$ [66].

According to computational experience accumulated during the last two decades, both approximations adequately describe the systems with rather delocalized *sp* valence electrons as well as the ground state properties (*e.g.*, the total energy surfaces $E_e(\mathbf{R})$, charge density distributions $\rho(\mathbf{r})$, *etc.*) [63]. On the other hand, quantitatively unappropriated results were rather obtained, for example, when studying the spectrum of one–electron energies ε_i, band gaps $\Delta\varepsilon$ in semiconductors and insulators, excited states, localized *d* or *f* electrons, strong electronic correlations, as well as such long–ranged interactions as van der Waals forces or hydrogen-bonded structures. It is very important to find such a functional $\hat{v}_{xc}[\rho(\mathbf{r})]$, which can be used for at least qualitative description of a large number of systems without additional parameters involved during calculation. For our *ab initio* study, the Perdew-Wang exchange-correlation functional PW91 has been chosen [64].

3.3. Periodic solid structures and plane-wave formalism

The DFT method briefly considered above was successfully applied for calculations on both finite-sized small molecules and clusters as well as periodic structures with 1D, 2D and 3D dimensionalities [54, 56, 66, 67]. The atomic structure of 3D periodic solid can be described by a Bravais lattice, where every primitive unit cell (PUC) contains one or more basis atoms depending on the chemical nature of considered solid (containing either one or several types of elements). These PUCs with various parallelepiped shapes are constructed using three nonplanar primitive basic vectors $\boldsymbol{a}_1$, $\boldsymbol{a}_2$ and $\boldsymbol{a}_3$ and determine different types of crystalline structure described by crystallographic point groups [54]. Translation operator $\hat{t}_{\boldsymbol{a}}$ acting through the lattice vector $\boldsymbol{a} = n_1\boldsymbol{a}_1 + n_2\boldsymbol{a}_2 + n_3\boldsymbol{a}_3$,

where n_1, n_2, n_3 are integers, relates the equivalent **r** and **r'** points of a given 3D crystal: **r'** = **r** + $\boldsymbol{a}$. A linear transformation of PUC translation vectors:

$$\boldsymbol{R}_j = \sum_{i=1}^{3} l_{ij}\boldsymbol{a}_i, \qquad \textit{(Eq. 3.3.1)}$$

where the integer coefficients l_{ij} form matrix $\|\boldsymbol{l}\|$ which determinant equals L. Vectors $\mathbf{R}_j$ and their integer linear combinations $\boldsymbol{R}_n = \sum_{j=1}^{3} n_j \boldsymbol{R}_j$ define for $L >$ 1 new, "rare" Bravais lattice for which it is possible to consider various unit cells also. The primitive cell of a new lattice with volume $V_{\boldsymbol{R}} = L \times V_{\boldsymbol{a}}$ will be the so-called large unit cell (supercell), in relation to an initial primitive unit cell. At L = 1 transformation described by *Eq.3.3.1* means transferring to other vectors of the basic translations, to another PUC under the form, but not on the volume [54]. The crystallographic (conventional) unit cell is defined as the minimal volume unit cell in the form of a parallelepiped constructed using vectors of translations and possessing the point symmetry of the lattice. Every real space Bravais lattice can be associated with a *dual* Bravais lattice of wave vectors called *reciprocal lattice* [68]:

$$\boldsymbol{K}_n = \sum_{k=1}^{3} m_{kn} b_k, \qquad \textit{(Eq. 3.3.2)}$$

where $\boldsymbol{a}_i \cdot \boldsymbol{b}_k = 2\pi\delta_{ik}$ (Kronecker's symbol $\delta_{ik} = 1$ if $i = k$, in other cases $\delta_{ik} = 0$). The unit cell of the reciprocal lattice that lies symmetrically around one lattice point $\mathbf{K}_n$ and contains all points that are closer to $\mathbf{K}_n$ than to any other lattice point is called the first Brillouin zone (BZ).

The electronic properties of periodic solids are described with the energy band model within the formalism of plane waves (PW) describing behavior of electronic system in a periodic potential [68]:

$$\hat{h}\psi_{n\boldsymbol{k}}(\boldsymbol{r}) = \left(-\tfrac{1}{2}\nabla_{\boldsymbol{r}}^2 + v_{eff}(\boldsymbol{r})\right)\psi_{n\boldsymbol{k}}(\boldsymbol{r}) = \varepsilon_{n\boldsymbol{k}}\psi_{n\boldsymbol{k}}(\boldsymbol{r}), \qquad \textit{(Eq. 3.3.3a)}$$

$$v_{eff}(\boldsymbol{r}) = v_{eff}(\boldsymbol{r} + \boldsymbol{R}), \qquad \textit{(Eq. 3.3.3b)}$$

where **R** is the lattice vector *(Eq.3.3.1)*, **k** the wave vector, v_{eff} the crystal potential, which is generated by the periodic lattice of the nuclei and also includes the interactions between the electrons as a mean field. Due to the periodicity of $v_{eff}(\mathbf{r})$, the wave function may be determined by the Bloch's theorem [54]:

$$\psi_{n\boldsymbol{k}}(\boldsymbol{r}) = u_{n\boldsymbol{k}}(\boldsymbol{r})e^{i\boldsymbol{k}\boldsymbol{r}}, \qquad \textit{(Eq. 3.3.4a)}$$

$$u_{n\boldsymbol{k}}(\boldsymbol{r} + \boldsymbol{R}) = u_{n\boldsymbol{k}}(\boldsymbol{r}), \qquad \textit{(Eq. 3.3.4b)}$$

where $u_{n\boldsymbol{k}}(\boldsymbol{r})$ is the UC's periodic part of the wave function $\psi_{n\mathbf{k}}(\mathbf{r})$ and i $= \sqrt{-1}$. The energies $\varepsilon_{n\mathbf{k}}$ describe the electronic band structure while the states $\psi_{n\mathbf{k}}$ are called Bloch states, where the band index n and the wave vector **k** are quantum numbers. The Kohn-Sham method employing a plane-wave basis set is one of powerful techniques in contemporary computational material science. The use of PW basis possesses several immediate advantages [68]: (*i*) it is easy to make a

change from a real-space representation (where the potential energy v_{eff} has a diagonal representation) *via* a fast Fourier transform to the momentum-space where the kinetic energy T is diagonal; (*ii*) the control of basis set convergence is almost trivial; it is sufficient to monitor the eigenvalues and total energies as a function of the *cut-off* energy, *i.e.*, the highest kinetic energy of a plane wave within the chosen basis set; (*iii*) the Hellmann-Feynman forces acting on the atoms and the stresses on the unit cell may be calculated directly in terms of the expectation value of the Hamiltonian with respect to the atomic (ionic) coordinates; (*iv*) basis-set superposition errors that have to be carefully controlled in calculations based on local basis sets are avoided.

The periodic functions of unit cells and arbitrary supercells can be written as a sum of plane waves, going to reciprocal space lattice and performing the Fourier transformation [68]:

$$u_{\boldsymbol{k}}(\boldsymbol{r}) = \sum_{\boldsymbol{G}} u_{\boldsymbol{k}}(\boldsymbol{G}) e^{i\boldsymbol{G}\boldsymbol{r}}, \qquad \textit{(Eq. 3.3.5a)}$$

$$\psi_{\boldsymbol{k}}(\boldsymbol{r}) = (N\Omega_0)^{-1/2} \sum_{\boldsymbol{G}} u_{\boldsymbol{k}}(\boldsymbol{G}) e^{i(\boldsymbol{k}+\boldsymbol{G})\boldsymbol{r}}, \qquad \textit{(Eq. 3.3.5b)}$$

$$u_{\boldsymbol{k}}(\boldsymbol{G}) = \frac{1}{\Omega_0} \int_{\Omega_0} e^{-i\boldsymbol{G}\boldsymbol{r}} u_{\boldsymbol{k}}(\boldsymbol{r}) d\boldsymbol{r}, \qquad \textit{(Eq. 3.3.5c)}$$

where **G** is chosen by such a way that $e^{i\mathbf{G}\mathbf{r}}$ has the periodicity of the real space lattice. In fact, the number of plane waves can be determined as a function of the kinetic energy cut-off, thus forming the PW sphere $\frac{(\boldsymbol{k}+\boldsymbol{G})^2}{2} < E_{cut}$ in reciprocal space [68].

Development of PW formalism as used in VASP computer code resulted in implementation of the *projector-augmented wave* (PAW) *method* originally introduced by Blöchl [69]. This method has been used in the current work. The main idea of PAW method is to transform the physically relevant full all-electron (AE) Kohn-Sham wave functions Ψ_n of this Hilbert space into a new computationally convenient pseudo-wave soft (PS) variational functions $\widetilde{\Psi}_n$ in so-called pseudo-Hilbert space [53]. Within the PAW formalism the AE wave function is derived from the PS wave function by means of a linear transformation [69]:

$$|\Psi_n\rangle = |\widetilde{\Psi}_n\rangle + \sum_i (|\varphi_i\rangle - |\tilde{\varphi}_i\rangle)\langle \tilde{p}_i | \widetilde{\Psi}_n\rangle, \qquad \textit{(Eq. 3.3.6)}$$

where the AE partial waves φ_i are obtained for a reference atom whereas the PS partial waves $\widetilde{\varphi}_i$ are equivalent to the AE partial waves outside a core radius r_c^l and match continuously onto $\widetilde{\varphi}_i$ inside the core radius (the augmentation region, similar to linearized muffin-tin LMTO formalism); the index *i* is a shorthand for the atomic site R_i, the angular momentum numbers $L = l, m$, and an additional index *k* referring to the one-electron reference energy ε_{kl}. The core radius is

chosen approximately about half the nearest-neighbor distance [69]. The projector functions $\tilde{p}_i$ are dual to the PS partial waves:

$$\langle \tilde{p}_i | \tilde{\phi}_j \rangle = \delta_{ij}. \qquad \textit{(Eq. 3.3.7)}$$

Contemporary DFT calculations on solids are determined by several key options: (*i*) the choice of exchange-correlation functional, (*ii*) the choice of a basis set to expand the Kohn-Sham eigenfunctions (plane waves or localized basis functions), and (*iii*) the choice of a way to describe interactions between the ionic core and the valence electrons (full-potential approach or pseudopotential approach [70]).

3.4. Simulation of equilibrium doped lattice and defect migration trajectories

Possible configurations of any stable complex crystalline system are determined by their correspondence to the local minima upon the potential electronic energy surface $E_e(\mathbf{R})$ (*PES*) defined by solution of *Eq.3.1.4* (where variable configuration **R** corresponds to coordinates of all the cores of chosen supercell). To construct the *PES* for determination of local minima and description of migration trajectories of impurity atoms and vacancies inside *fcc*-Fe lattice, the minimization procedure for the total energy of the system with respect to all atomic coordinates and unit cell parameters must be performed [71, 72]. In the multi-dimensional phase space made of all structural parameters, the potential energy surface consists of "valleys" and "hills" which are connected by saddle points (Figure 3.1).

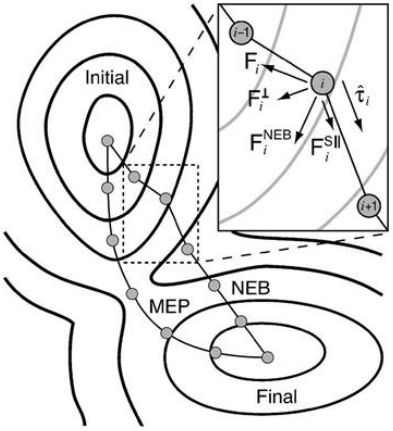

Figure 3.1. Illustration of the nudged elastic band method [41]. The initial and final states are two local minima of the energy surface. To determine the minimum energy path (MEP) between these states, an initial guess of the reaction path (dashed line) is constructed by connecting the initial and the final states. A number of images of the system (gray solid circles) are positioned along the path. The initial path is then optimized to yield the MEP (solid line) on the energy surface.

Each valley acts as a local basin of attraction, and any local minimization methods such as conjugate gradients can only find a local minimum lying in a basin which is not necessarily the global minimum. In order to localize the point of global minimum instead of local ones, various stochastic methods have been

proposed including the so-called basin hopping [71], random searching [72] and genetic algorithms [72, 73], which allow one to determine the global minimum with certain probability.

Next, a certain number of lowest-energy structures after relaxation must be chosen (discarding the remaining ones) and then be used as parents to randomly generation off spring through crossover and mutation [74]. Then, these new structures are passed on to compete in the next generation by relaxing them to local minima and comparing their total energies. Finally, the above process is iterated until convergence criteria are satisfied or a maximum number of iterations (generations) is reached. To find the saddle points on a potential energy surface, the minimum-mode method can be used [75]. It is complimentary to the nudged elastic band method because it does not require a final state. If the transitions out of a basin are found, their individual rates can be evaluated, and the system can be evolved over long time scales using the kinetic Monte Carlo simulations [76] which move the system over that saddle point to an adjacent basin.

3.5. Application of pseudopotentials for construction of PW basis set

The pseudopotential method provides an efficient modeling of the electron-ion interaction to assist *ab initio* calculations based on the DFT method [70, 77]. Two basic approximations are included in construction of pseudopotentials: (*i*) the separation of frozen chemically inert core electrons from chemically active electrons of external atomic shell (in some pseudopotentials not only valence electrons but also electrons of subvalence shells are included in external shell); (*ii*) external shells (half-filled or completely filled with electrons) possess the spherical symmetry (so-called Unsold's Theorem [78]). Application of pseudopotentials allows one to describe separately only the outer shells' electrons. In turn, all the inner electrons can be substituted by a joint effective pseudopotential. Depending on the number of included electrons the pseudopotentials can be separated as large core (LC) and small core (SC) relativistic energy-consistent pseudopotentials (RECP) [79].

One of the main objectives, in order to perform large-scale PW-DFT calculations, is the proper choice of PAW pseudopotentials extracted from the library combined with the *VASP* code [52] since a wrong choice of these pseudopotentials could lead to incorrect or implausible results. Pseudopotentials provided by *VASP* are usually used as set in the library because either creation or re-optimization of them usually requires several months and even years. *VASP* provides three pseudopotentials that describe Fe atom, which possesses the electron structures which differ by the number of core electrons and the number of valence electrons (10 and 18 core electrons with $3s^2 3p^6 3d^7 4s^1$ and $3d^7 4s^1$ external electrons, respectively, or 12 core electrons with $3p^6 3d^7 4s^1$ external electrons). According to recommendations suggested in *VASP* manual we have used for our calculations the pseudopotential with 18 core electrons (LC) and

$3d^7 4s^1$ valence electrons, which core corresponds to Ar atom, *i.e.*, $1s^2 2s^2 2p^6 3s^2 3p^6$. This pseudopotential has been tested on simple calculations and provided plausible results for properties of *fcc*-Fe lattice. *VASP* library contains two pseudopotentials for O atom. Both contain the same information about the structure of core and valence electrons (two core $1s^2$ electrons and $2s^2 2p^4$ valence electron shell). Although both pseudopotentials have been tested, one of them has been excluded, due to both unsatisfactory convergence and estimated values of diffusion barriers for oxygen impurity atom. *VASP* library supplies three pseudopotentials for Ti with different number of external electrons (4, 10, and 12). The PAW pseudopotential recommended by *VASP* includes 12 valence electrons configured in $3p^6 4s^2 3d^4$ external shell. As to Y the only pseudopotential has been available in the *VASP* library, which describes 28 core electrons and $4s^2 4p^6 5s^1 4d^2$ shell with 11 external electrons, respectively.

3.6. Computational parameters used in the VASP calculations

To perform large-scale calculation using *VASP* PW code, at least four input files are required:

(i) POSCAR, which contains information on geometry of the calculated model such as extension of the lattice unit cell as well as coordinates of all supercell (or UC) atoms coordinates in; including impurities; in addition, it is possible to fix all or part of SC (or UC) atoms during the whole relaxation procedure;

(ii) POTCAR, which contains the pseudopotentials for each atomic species used in the calculation [52]. If the calculations are performed on a model containing atoms of different chemical nature, several POTCAR files are joined within one POTCAR file;

(iii) KPOINT, which specifies the *k*-point mesh in the BZ for the model under the consideration;

(iv) INCAR, the main operating file required to perform any *VASP* calculations; this file contains a lot of parameters that specify how to perform the calculations and what parameters must be used.

The full list of all possible *VASP* parameters and keywords is given in [52]. It is suggested to perform the *VASP* calculations using the minimum number of parameters, so that the other parameters would be automatically set to the default values. To check if the used set of parameters allows one to achieve plausible results, it is necessary to perform the test calculations (firstly, for ideal *fcc*-Fe lattice). The parameters that have been used in the calculations within PhD activities are following:

- NPAR – number of cores *per* computer node;
- NSIM – number of NSIM bands can be simultaneously optimized;
- NCORE – total number cores/NPAR;

- ISMEAR determines how partial occupancies are set for each shell (using GAUSSIAN smearing);
- ENCUT – cut-off energy (in eV) for certain PW basis set. All plane-waves with a kinetic energy smaller than that are included in the basis set;
- NSW sets the maximum number of ionic steps;
- IBRION determines the algorithm how the ions are updated and moved;
- POTIM serves as a scaling constant for the forces for IBRION = 1, 2 or 3;
- ISPIN specifies whether to perform spin-polarized calculations or not;
- IALGO specifies different algorithms used in *VASP* computer code.

NPAR and NSIM parameters significantly affect the efficiency of the performed calculations, however, these parameters are dependent on the hardware used in the supercomputers. As the calculations performed within this PhD thesis have been done during several years on different supercomputers the different values of these parameters have been used. NCORE has been added to VASP since VASP 5.2.13 and VASP manual recommends using this parameter instead of NPAR in the calculations as it allows to use computational power more efficiently. It should also be noted that NPAR and NCORE parameters cannot be used together in the input files as NPAR parameter has higher priority over NCORE. Similarly to both NPAR and NSIM parameters NCORE is dependent on the hardware used for the calculations.

ISMEAR = 2 has been used in the calculations as the VASP manual recommends this value for the calculations of metals. To use the conjugate gradient algorithm during the calculations. IBRION value has been set to 2, while POTIM has been set to 0.2.As we have assumed that at high HIPping temperatures the magnetic moments in fcc-iron lattice are disordered we have performed non spin polarized calculations by setting ISPIN to 1.The default algorithm used in *VASP* computer code has been used in calculations, so IALGO parameter has been omitted in the input files.

The cut-off energy has been varied from 300 to 1200 eV while the **k**-point set has been changed from 64 (4×4×4) to 4096 (16×16×16) generated *k*-point mesh using the Monkhorst-Pack's technique [80]. To determine the electron populations within the Methfessel-Paxton method has been used [81]. It has been found that the results reliably converged only beginning with the unusually large cut-off energy of 800 eV (*cf.* the default cut-off energy of 267 eV), while when varying the *k*-point mesh, it has been found that at least 9×9×9 mesh allows us to obtain plausible results. The increase of the cut-off energy to 900 or 1000eV did not affect the results, however, computational time increase approximately two times. And the increase of the *k*-point mesh to 12×12×12 also requires two times more of CPU time.

The relative atom displacements δr have been calculated using rdf.pl script available in the VASP TST tools [82] containing source code and scripts for localization of saddle points between the two preliminary fixed local minima on the energy surface and evaluating rate constants within the formalism of transition state theory (TST) [83-85]. Various tools have been also used to

construct the models of both perfect and defective lattices, to check and analyze their structure before and after the relaxation, to draw the total and difference electron charge density plots [P5].

4. Verification of *ab initio* calculations on simplest γ-Fe models

In order to optimize the parameters of DFT-PAW calculations necessary to reproduce properly the basic available experimental data for γ-Fe (optimal supercell sizes, lattice constant a_0, bulk modulus B, cohesive energy *per* atom E_{coh}, structural relaxation around the point defects δr_i, charge transfers towards/outwards these defects accompanying by electron density redistribution, *etc.*), a series of test calculations has been performed on both perfect lattice and that containing single point defects.

4.1. Perfect *fcc*-iron lattice

A series of preliminary calculations has been performed within the PAW-PW91 plane-wave formalism in order to define the computational parameters reproducing the experimental and simulation data (*e.g.*, lattice constant, bulk modulus and cohesive energy *per* atom in *fcc*-Fe) [P1], including an analysis how the convergence of the results depends on the supercell size, the cut-off energy and the *k*-point set in the corresponding Brillouin zone. We have found that the calculations of the 27-atom $3a_0\times3a_0\times3a_0$ supercell, commonly used previously, have been found to be still inaccurate, due to a small size of the supercell which causes the noticeable interactions between defect and its periodical image in further calculations on defective lattice. Thus, the supercell has been extended to 64 atoms with the $4a_0\times4a_0\times4a_0$ enlarged translation vectors of the unit cell (Fig. 4.1).

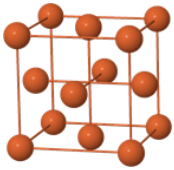

Figure 4.1. The unit cell of the perfect *fcc*-iron lattice

For calculations on the pair of Y atoms in *fcc*-Fe lattice, even larger, at least $4a_0\times4a_0\times6a_0$ (96-atom), which symmetry is lower, and $5a_0\times5a_0\times5a_0$ (125-atom) supercells are required. Optimized values of the lattice constant a_0 for them have been calculated to be almost the same, ~3.448 Å, while computed values of bulk modulus B and the cohesion energy E_{coh} have been found to be 162 GPa and 4.96 eV/atom, respectively. Obtained data qualitatively agree with the results of alternative *ab initio* calculations on the same structure performed previously: (*i*) 3.40–3.60 Å [85,86], (*ii*) 171–211GPa [85,87], (*iii*) 4.42 eV/atom [87], respectively, and with the corresponding experimental values of: (*i*) 3.57 Å [83],

(*ii*) 133–164 GPa [88] for *γ*-Fe, which can exist in different magnetic states, (*iii*) 4.28 eV/atom [85] for a low-temperature ferromagnetic α-Fe which is believed to be close to cohesive energy of *γ*-Fe.

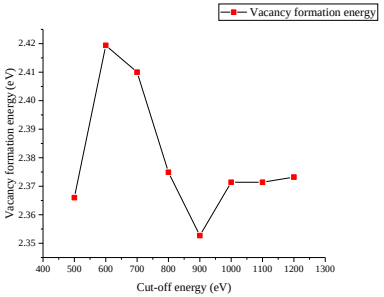

Figure 4.2. Convergence of V_{Fe} vacancy formation energy depending on the cut-off energy.

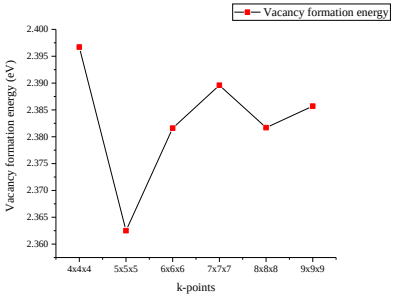

Figure 4.3. Convergence of V_{Fe} vacancy formation energy depending on the *k*-point set.

The cut-off energy has been varied from 300 to 1200 eV (Fig. 4.2) and the *k*-point set from 64 (4×4×4) to 4096 (16×16×16) as shown in Fig. 4.3. It has been found that the results are reliably converged only beginning with the unusually large cut-off energy of 800 eV (*cf.* with the default cut-off energy of 267 eV), while for a varying *k*-point mesh, only 6×6×6 and larger mesh allowed us to obtain qualitatively plausible results. The calculations on γ-Fe have clearly shown that for achieving plausible results for basic parameters aforementioned cut-off kinetic energies must be increased at least up to 800 eV. In any case, for arbitrary configuration of defective iron supercells, positions of all atoms have been optimized by a minimization of the total energy.

4.2. fcc-iron lattice containing single point defect *per* supercell

The formation energy of single vacancy (Fig. 4.4a) in a 4×4×4 γ-Fe unit cell, which is surrounded by twelve nearest iron atoms forming cuboctahedron, has been found to be 2.37 eV accompanied with 0.75% and ~0.5% inward relaxation of the two nearest coordination shells [P1].

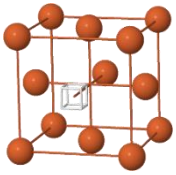

Figure 4.4a. The model of V_{Fe}.

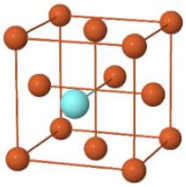

Figure 4.4b. The model of Y_{Fe} substitute.

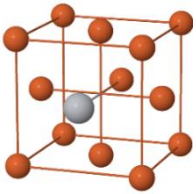

Figure 4.4c. The model of Ti_{Fe} substitute.

To calculate the formation energy of single V_{Fe} vacancy (Fig. 4.4a) the following equation is used:

$$E_{vac}^{form} = E_{Fe-vac} - \frac{N-1}{N} E_{Fe}, \qquad \textit{(Eq. 4.2.1)}$$

where E_{Fe-vac} is a total energy of 4×4×4 supercell of *fcc*-Fe lattice containing one V_{Fe} vacancy, N the number of atoms *per* supercell and E_{Fe} the total energy of the ideal iron lattice. The vacancy causes a noticeable electron charge redistribution with the closest Fe atoms as can be observed in Fig. 4.5.

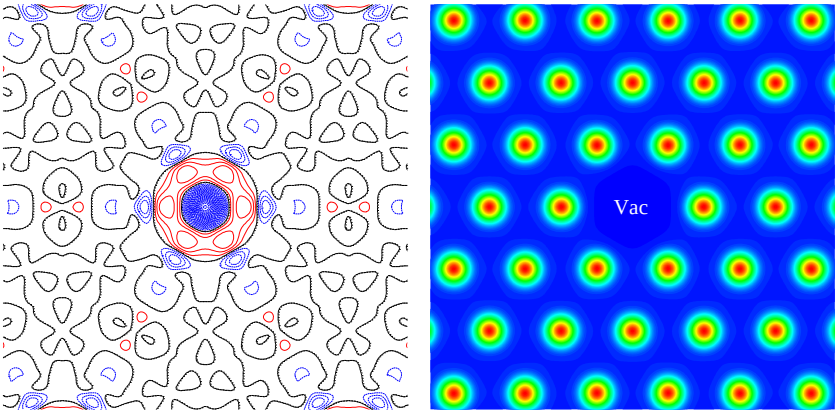

Figure 4.5. Difference (left) and total (right) electron charge density distributions along (111) section of *fcc*-Fe supercell containing V_{Fe} vacancy in the center. Solid (red), dash (blue) and dash-dot (black) isolines (with the increment of 0.002 e/Å^3) represent positive, negative and neutral electronic charge, respectively.

The calculations of Y atom in γ-Fe lattice have been performed assuming that the Y atom is substituting the regular site of Fe lattice (Fig. 4.4b). The Y_{Fe} atom donates the electronic density to the nearest Fe neighbors (charge transfer $\Delta q \approx 1$ *e per* atom) as shown in Figure 4.6. The formation energy of the Y-substitution defect in the γ-Fe lattice is estimated to be 0.48 eV *per* 4×4×4 supercell, with the 7% and ~2% expansion of the two nearest coordination shells, respectively. At the same time, the Y atom inserted in the *fcc* Fe lattice is rather affected by repulsion from the nearest Fe neighbors as follows from the electron charge re-distribution.

The following equation has been used to calculate yttrium formation energy:

$$E_{Y}^{form} = E_{Fe-Y} - \frac{N-1}{N} E_{Fe} + E_{cohY}, \qquad \textit{(Eq. 4.2.2)}$$

where E_{Fe-Y} is a total energy of the Fe supercell with one Y_{Fe} substitute atom, N the number of atoms in the supercell, E_{Fe} the total energy of perfect γ-Fe lattice, E_{cohY} – the cohesive energy of Y_{Fe}.

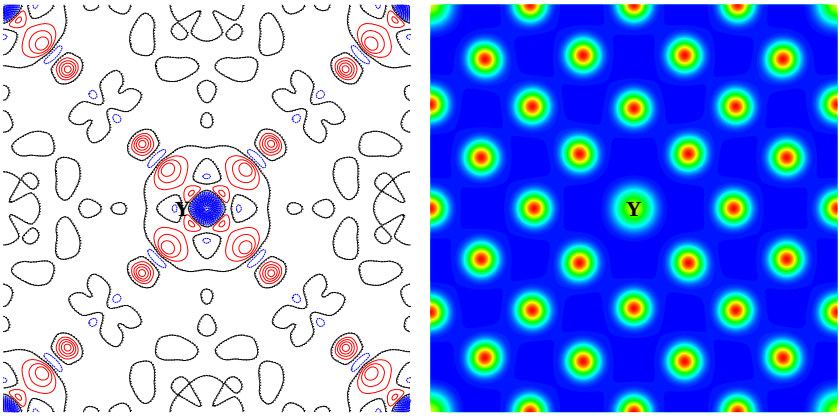

Figure 4.6. Difference (left) and total (right) electron charge density distributions along (001) section of *fcc*-Fe supercell containing Y_{Fe} substitute in the center. Solid (red), dash (blue) and dash-dot (black) isolines (with the increment of 0.002 e/Å^3) represent positive, negative and neutral electronic charge, respectively.

The simulations of the Ti impurity atom in γ-Fe lattice has been performed similarly to those for Y solute atom (Fig. 4.1c). Ti_{Fe} substitute donates $\Delta q \approx 1.1$ e to the nearest Fe neighbors as demonstrated in Fig. 4.7. The first coordination sphere around Ti_{Fe} has expanded by ~3%, while 2nd coordination sphere is shrunk by about 0.5%.

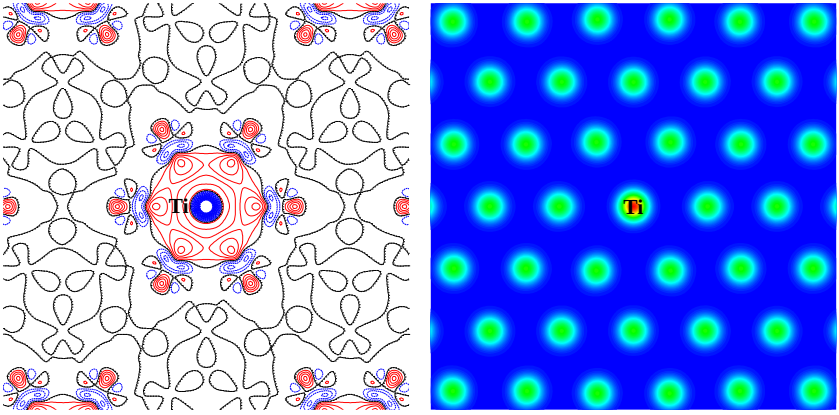

Figure 4.7. Difference (left) and total (right) electron charge density plots distributions along (111) section of *fcc*-Fe supercell containing Ti_{Fe} substitutite in the center. Solid (red), dash (blue) and dash-dot (black) isolines (with the increment of 0.002 e/Å^3) represent positive, negative and neutral electronic charge, respectively.

In contrary, oxygen atoms may be arranged inside the same γ-Fe supercell either on octahedral *O* site (six nearest Fe neighbors, Fig. 4.8a), tetrahedral *T* site (four nearest Fe neighbors, Fig. 4.8b), or in the substitutional position O_{Fe} (Fig. 4.8c) [P1]. The presence of interstitial O_i atom results in a considerable expansion

of the two nearest coordination spheres around an impurity atom (1.75% and ~9% for octahedral and tetrahedral positions, respectively). A barrier for oxygen atom migration between the nearest *O* and *T* positions has been found to be 1.1 eV (*cf.* 1.72–1.75 eV, according to various experimental studies systematized in the handbook [84]). Moreover, *O* position is found to be ~0.1-0.2 eV more favourable than *T*, in accordance with results of theoretical simulations of oxygen absorbed in the *fcc* Al lattice [89], while V_{Fe} vacancy is about 0.5 eV energetically more favourable for arrangement of O_{Fe} substitute than *O* site for location of O_i. It is worth noting that O_{Fe} displaces by about 0.79 Å towards the *O* position due to relaxation while O_i atom moves from octahedral interstitial position towards the V_{Fe} by 0.07 Å being trapped by the latter which can block further interstitial migraton of oxygen impurities. The migration barrier for the diffusion between O_{Fe} and *O* has been estimated by us ~1.5 eV.

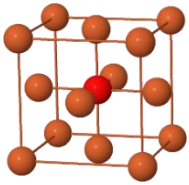

Figure 4.8a. The model of O_{oct} on octahedral interstitial position *O*

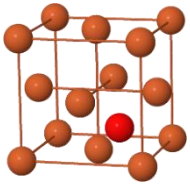

Figure 4.8b. The model of O on tetrahedral interstitial position *T*

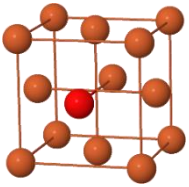

Figure 4.8c. The model of substitutional atom O_{Fe}

The excessive electronic charge attracted by O_{oct} in γ-Fe lattice achieves $\Delta q \approx 1.4$ *e* as shown in Fig. 4.9 (*cf.* $\Delta q \approx 1.8$ *e* for the same position of O atom in *fcc* Al lattice [89]).

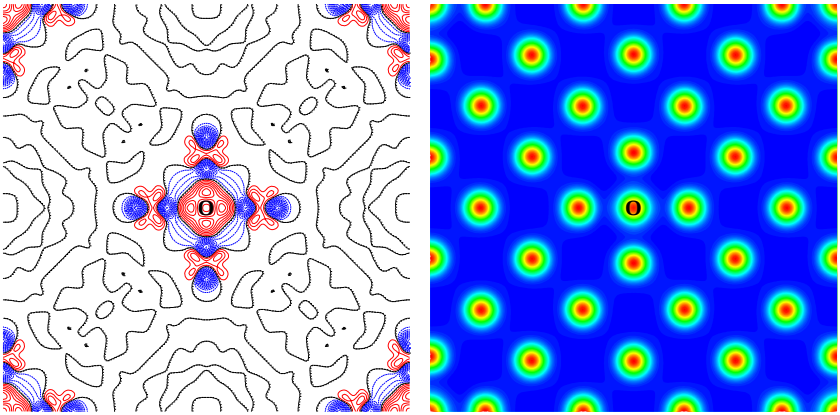

Figure 4.9. Difference (left) and total (right) electron charge density distributions along (001) section of *fcc*-Fe supercell in *O* configuration, where O_{oct} is located in the interstitial octahedral position. Solid (red), dash (blue) and dash-dot (black) isolines (with the increment of 0.002 $e/Å^3$) represent positive, negative and neutral electronic charge, respectively.

Formation energy of oxygen interstitial atom is calculated according to the following equation:

$$E_{O_{oct}}^{form} = E_{Fe+O} - (E_{Fe} + E_O), \qquad \textit{(Eq. 4.2.3)}$$

where E_{Fe+O} is the total energy of γ-Fe lattice with oxygen atom in interstitial *O* center, E_{Fe} the total energy of the ideal *fcc*-Fe lattice and E_O the energy of single oxygen atom (analogously, the formation energy of oxygen in tetrahedral *T* center have been estimated). To estimate the formation energy of substitutional O_{Fe} in *fcc*-Fe lattice, we have used *Eq. 4.2.2*.

5. *Ab initio* calculations on multiple-wise defects in γ-Fe models

5.1. Pairwise defects

The two substitute Y_{Fe} atoms incorporated in V_{Fe} vacancies have been positioned at permanently increasing interdefect distances (1NN, 2NN, 3NN and 4NN corresponding to the nearest neighbor separations of consequent atomic coordination spheres in lattice) [P2, P3]. Since no binding is found between them at any interatomic distance (*i.e.*, the binding energies have been found to be negative, varying from -0.45 eV down to -1.05 eV as shown in Table 5.1), we have considered influence of vacancies on the binding of Y_{Fe} atoms in γ-Fe lattice.

Table 5.1. Calculated parameters for Y_{Fe}-Y_{Fe} pair in γ-Fe

Configuration	E_{bind}, eV	Δq (Y_{Fe}), e*	δr_Y, Å
1NN	-0.73	1.00	0.11
2NN	-0.45	1.08	0.01
3NN	-0.46	1.07	0.03
4NN	-1.05	1.07	0.00

*estimated within the Bader topological analysis [90]

Similarly to the results of the Y_{Fe}-Y_{Fe} calculations, no binding energies are found between both Y_{Fe}-Ti_{Fe} and Ti_{Fe}-Ti_{Fe} impurity pairs (Tables 5.2 and 5.3 respectively). It is worth noting that the largest absolute values of the binding energies are found for the calculated Y_{Fe}-Y_{Fe} interactions while the smallest absolute values are assessed for Ti_{Fe}-Ti_{Fe} configurations. The absolute values of the binding energies between Y_{Fe}-Ti_{Fe} pairs are close to the average value between Y_{Fe}-Y_{Fe} and Ti_{Fe}- Ti_{Fe} binding energies.

Table 5.2. Calculated data for Y_{Fe}-Ti_{Fe} pair

Configuration	E_{bind}, eV	Δq, e* (Y_{Fe})	Δq, e* (Ti_{Fe})	δr_Y, Å	δr_{Ti}, Å
1NN	-0.44	1.06	1.03	0.04	0.19
2NN	-0.12	1.12	1.11	0.00	0.02
3NN	-0.17	1.12	1.11	0.00	0.03
4NN	-0.24	1.11	1.09	0.00	0.00

*estimated within the Bader topological analysis [90]

Table 5.3. Calculated data for Ti_{Fe}-Ti_{Fe} pair

Configuration	E_{bind}, eV	Δq, e* (Ti_{Fe})	δr_{Ti}, Å
1NN	-0.29	1.07	0.10
2NN	0.02	1.12	0.03
3NN	-0.06	1.11	0.00
4NN	-0.03	1.12	0.00

*estimated within the Bader topological analysis [90]

The largest displacement of the atoms during relaxation occurs when Y_{Fe} and Ti_{Fe} atoms are the 1NN neighbors, while almost no displacement is observed for other configurations. Both Y_{Fe} and Ti_{Fe} atoms donate about the same amount of electronic charge Δq to the closest Fe atoms in the lattice. Both Ti_{Fe} atoms donate the same charge, while their displacement δr in the γ-Fe lattice is also the same. Ti_{Fe} atoms donate about 1.10 e to the closest Fe atoms. The largest displacement of Ti_{Fe} atoms are obesrved when both Ti_{Fe} atoms are the 1NN, while the absolute value of the δr_{Ti} decreases to 0 Å with the increase of the distance between the defects.

We have also calculated the pair-wise interactions of the two O_{Fe} atoms separated by different distances (Table 5.4 and Figure 5.1) {P3]. Results of performed calculations indicate no binding energy for all the possible values of O_{Fe}-O_{Fe} separation. Both O_{Fe} substitute atoms accept slightly more than 1.0 e from the nearest Fe atoms. For both oxygen atoms at 1NN position, $d_{O\text{-}O}$ distance grows by 1.28 Å during the relaxation. For the two O_{Fe} atoms positioned at 2NN, $d_{O\text{-}O}$ is reduced on 1.19 Å during the relaxation, while both for 3NN and 4NN configurations, $d_{O\text{-}O}$ is again increased: by 1.28 Å and 1.04 Å, respectively.

Table 5.4. Calculated data for O_{Fe}-O_{Fe} pair.

Configuration	E_{bind},eV	Δq, e*(O_{Fe})	δr_O, Å
1NN	-0.11	-1.11	0.63
2NN	-0.51	-1.06	0.59
3NN	-0.10	-0.74	0.82
4NN	-0.05	-1.04	1.02

*estimated within the Bader topological analysis [90].

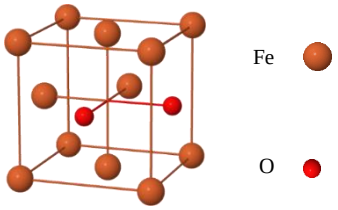

Figure 5.1 Initial 1NN structure of O_{Fe}-O_{Fe} pair

When calculating the binding energies in O_{Fe}-V_{Fe} pair, the highest binding energy is found to be in O_{Fe}-V_{Fe} at 2NN positions (1.18 eV) as presented in Table 5.5.

Table 5.5. Calculated parameters for O_{Fe}-V_{Fe} pairs

Configuration	E_{bind},eV	Δq, e*(O_{Fe})
1NN	0.64	1.15
2NN	1.18	1.21
3NN	0.13	1.10
4NN	0.09	1.09

*estimated within the Bader topological analysis [90]

As shown in Table 5.7, the binding energies between Ti_{Fe} atoms and V_{Fe} vacancies are quite similar to the ones between Y_{Fe} and V_{Fe} (Table 5.6 and Figure 5.2) [P2, P3]. The largest binding energy is found between Ti_{Fe} and V_{Fe} as the first nearest neighbours, no binding energy was found between these defects in 2NN configuration, while small binding energy was found for 3NN and 4NN configurations. The largest displacement δr of Ti atom (0.42 Å) and the largest electron charge transfer from Ti atom (1.16 e) are observed when Ti atom is placed as the 1NN to the vacancy.

The positive binding energies E_{bind} are found for the configurations where Y_{Fe} and V_{Fe} are 1NN, 3NN and 4NN, while repulsion takes place at 2NN distance. The largest binding energy of 1.67 eV corresponds to 1NN distance between Y_{Fe} and V_{Fe} accompanied by significant displacement of δr_Y 1.25 Å of yttrium atom towards vacancy (corresponding approximately to a half of 1NN distance since during the relaxation, the closest atoms are moved too). No noticeable change of effective charge on impurity atom (Δq) is induced irrespectively of the length of Y_{Fe}-V_{Fe} pair.

The largest binding energy in Y_{Fe}-O_{Fe} pair is calculated at 1NN distances, and it decreases with the increase of distance between the atoms as shown in Table 5.8. The largest charge transfers from Y_{Fe} atom to O_{Fe} atom is assessed for 1NN configuration. During the relaxation the largest displacement of Y atom (0.94 Å) is also observed for the 1NN configuration, while almost no displacement of Y atom occurrs during the relaxation of all other Y_{Fe}-O_{Fe} configuraions [P3]. It is worth mentioning that O displacement during the relaxation of all four Y_{Fe}-O_{Fe} configuraions has been quite significant.

Table 5.6. Calculated data for Ti_{Fe}-V_{Fe} pairs

Configuration	E_{bind}, eV*	Δq, e*(Ti_{Fe})	δr_{Ti},Å
1NN	0.46	1.16	0.42
2NN	-0.09	1.10	0.01
3NN	0.10	1.12	0.03
4NN	0.12	1.13	0.00

Table 5.7 Calculated data for Y_{Fe}-V_{Fe} pairs

Configuration	E_{bind}, eV*	Δq,e*(Y_{Fe})	δr_Y, Å
1NN	1.67	0.99	1.25
2NN	-0.21	0.97	0.03
3NN	0.30	1.01	0.05
4NN	0.40	1.03	0.00

*estimated within the Bader topological analysis [90]

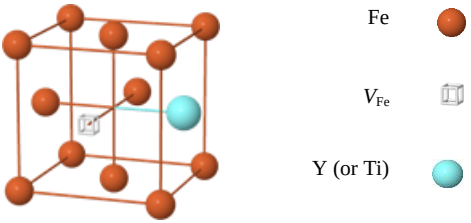

Figure 5.2. Initial 1NN configuration of V_{Fe}–Y_{Fe} (or Ti_{Fe}) pair.

Similarly, to the Y_{Fe}-O_{Fe} configuraions, the largest binding energy in Ti_{Fe}-O_{Fe} pair is calculated at 1NN distance (Table 5.9). Displacements of atoms for these configurations are also similar to Y_{Fe} and O_{Fe} atom displacements (as for configurations in Table 5.8) with the largest shift of Ti_{Fe} atom observed during the relaxation of 1NN configuration. Noticeable displacement of O_{Fe} atom is also observed for all four configurations. Ti_{Fe} donates the largest amount of charge (1.21 *e*) in the 1NN configuration, while O_{Fe} attracts about the same number of electrons in all configurations.

Table 5.8. Calculated data for Y_{Fe}-O_{Fe} pairs

Configuration	E_{bind}, eV*	Δq, *e** (Y_{Fe})	Δq, *e** (O_{Fe})
1NN	1.59	1.25	-1.20
2NN	0.80	1.15	-1.26
3NN	0.22	1.10	-1.05
4NN	0.21	1.14	-1.12

Table 5.9. Calculated parameters for Ti_{Fe}-O_{Fe} pairs

Configuration	E_{bind}, eV*	Δq, *e** (Ti_{Fe})	Δq, *e** (O_{Fe})
1NN	0.20	1.21	-1.12
2NN	0.11	1.10	-1.13
3NN	0.14	1.13	-1.07
4NN	0.18	1.12	-1.12

*estimated within the Bader topological analysis [90]

No binding is found between Y_{Fe} and O_{oct} in the octahedral interstitials (Table 5.10) when the defects are positioned in the first coordination sphere [P3]. The increase of the distance between O_{oct} and Y_{Fe} leads to the appearance of the binding energy between the point defects. It is worth noting that oxygen atom attracts noticeably more electronic charge from the closest atoms when it is located in the octahedral interstitial position (~1.35-1.38 *e*) compared to the configurations when oxygen atom occupies the regular lattice site (substitutional position) while Y_{Fe} atom donates about the same amount of electronic charge, both when O atom occupies interstitial or substitutional positions. The largest displacements of the atoms have been observed when Y_{Fe} and O_{oct} have been located in the first coordination sphere.

Table 5.10. Calculated parameters for Y_{Fe}-O_{oct} pairs

Configuration	E_{bind}, eV*	Δq, *e** (Y_{Fe})	Δq, *e** (O_{oct})	δr_Y, Å	δr_O, Å
1st sphere	-0.21	1.17	-1.36	0.23	0.20
2nd sphere	0.39	1.09	-1.38	0.06	0.01
3rd sphere	0.42	1.10	-1.35	0.05	0.05

*estimated within the Bader topological analysis [90]

Table 5.11. Calculated parameters for Ti_{Fe}-O_{oct} pairs

Configuration	E_{bind}, eV*	Δq, e* (Ti_{Fe})	Δq, e* (O_{oct})	δr_{Ti}, Å	δr_O, Å
1st sphere	-0.41	1.17	-1.39	0.18	0.06
2nd sphere	0.16	1.08	-1.38	0.08	0.01
3rd sphere	0.12	1.11	-1.37	0.03	0.02

*estimated within the Bader topological analysis [90]

No binding energy is found also between Ti_{Fe} and O_{oct} in the octahedral interstitials (Table 5.11) when the defects are placed in the first coordination sphere, while the binding energy is found to be average between both defects at the distance of 2nd and the 3rd coordination spheres. These results are similar to those obtained in calculations of Y_{Fe}-O_{oct} pair. The displacement of the atoms is smaller though, which can be explained by the fact that Ti atom size is close to the size of Fe atoms and is noticeably smaller than that of Y. This results in a smaller disturbance of the lattice caused by Ti_{Fe} impurity atom compared to Y_{Fe}. Similarly to the configurations described in Table 5.8 the charge transfer to O_{oct} is noticeably larger than for in Ti_{Fe}–O_{Fe} pair, while the charge transfer from Ti atom is similar for all the calculated configurations.

5.2. Multiple-wise V_{Fe}-vacancy cluster reducing barrier for Y_{Fe} migration

Recent calculations performed on V_{Fe}-containing *bcc*-Fe lattices with varied defect concentration clearly show that precipitates from V_{Fe} vacancies create stable clusters in α-iron [Q5] based on chosen configurations and fixed number of vacancies (octahedron and simple cube containing 6 and 8 vacancies, respectively). Moreover, Y_{Fe} solute atoms (possessing largest sizes among impurities considered in this PhD study) surrounded by vacancies can be stabilized in the host iron matrix and their migration is noticeably more effective *via* multiple steps within the V_{Fe}-containing cluster.

For *fcc*-Fe, we have studied stability of V_{Fe} clusters containing 2-4 vacancies *per* γ-Fe unit cell and their influence on migration of Y_{Fe} substitutes [P4].

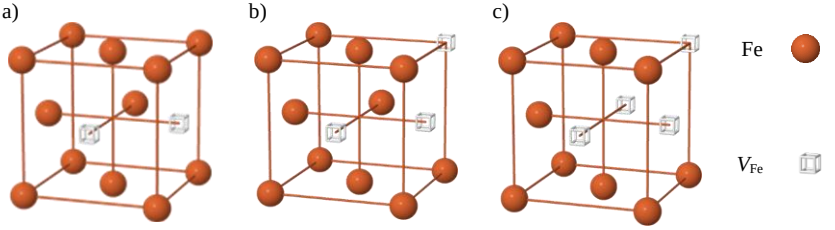

Figure 5.3. Three models of *fcc*-Fe unit cells containing different number of iron vacancies:
(a) two V_{Fe} defects (b) three V_{Fe} defects (c) four V_{Fe} defects

The results describing the interactions between the two lattice vacancies show rather weak binding between two V_{Fe} vacancies positioned at 1NN and 3NN posttions and a slight repulsion for 2NN and 4NN interdefect distances (Table 5.12 and Fig. 5.3a corresponding to 1NN configuration).

Table 5.12. Binding *per* vacancy in V_{Fe}-V_{Fe} pairs

Configuration	E_{bind}, eV [P3,P4]
1NN	0.25
2NN	-0.09
3NN	0.10
4NN	-0.12

Table 5.13. Binding *per* vacancy in multiple configurations of $(V_{Fe})_n$ where n = 2-4

Configuration	E_{bind}, eV
2 V_{Fe}	0.25
3 V_{Fe}	0.37
4 V_{Fe}	1.32

Values of binding energies are expressed *via* corresponding formation energies [P3]:

$$E_{2V_{Fe}}^{bind} = 2E_{V_{Fe}}^{form} - E_{2V_{Fe}}^{form}, \quad \textit{(Eq. 5.2.1a)}$$

$$E_{3V_{Fe}}^{bind} = 3E_{V_{Fe}}^{form} - E_{3V_{Fe}}^{form}, \quad \textit{(Eq. 5.2.1b)}$$

$$E_{4V_{Fe}}^{bind} = 4E_{V_{Fe}}^{form} - E_{4V_{Fe}}^{form} \quad \textit{(Eq. 5.2.1c)}$$

where the formation energy of one iron vacancy $E_{V_{Fe}}^{form}$ is determined by *(Eq. 4.2.1)*, the formation energies of vacancies' pair and triad are $E_{2V_{Fe}}^{form} = E_{lattice+2V_{Fe}}^{total} - \frac{N-2}{N} E_{perfect\ lattice}^{total}$ and $E_{3V_{Fe}}^{form} = E_{lattice+3V_{Fe}}^{total} - \frac{N-3}{N} E_{perfect\ lattice}^{total}$, respectively, N the number of atoms *per fcc*-Fe supercell, while $E_{lattice+2V_{Fe}}^{total}$, $E_{lattice+3V_{Fe}}^{total}$ and $E_{perfect\ lattice}^{total}$ the total energies of iron lattice containing either pair and triad of V_{Fe} vacancies (*per* supercell) or corresponding to perfect crystal.

Table 5.13 shows that the binding energy increases with the growth of the number of the vacancies in densely-packed $(V_{Fe})_n$ cluster inside *fcc* Fe lattice (Figs. 5.3(a-c). The highest binding energy in the configurations with two neares V_{Fe} vacancies (1NN) is found to be 0.25 eV increasing to 0.37 eV in the case of $3V_{Fe}$ configuration, while the highest binding energy per vacanxy in the configurations with multiple vacancies has been observed in 4 V_{Fe} configuration (1.32 eV).

The results presented in Table 5.14 clearly shows a noticeable influence of iron vacancies, *e.g.*, their number and arrangement (Figs 5.4a-c), on the binding energies of single Y_{Fe} substitute (two and three V_{Fe} vacancies are positioned in the closest sites to it). In the Y_{Fe}-$2V_{Fe}$ (1NN) configuration (Figure 5.4a), yttrium impurity atom donates 1.52 *e* to the closest Fe atoms while its displacement from the initial substitute position is found to be 1.03 Å. When Y_{Fe} and two vacancies are at the 2NN positions (Fig. 5.4b) Y_{Fe} donates smaller amount of 1.24 *e* to the closest iron atoms while its shift from the initial position is 0.61 Å. The calculations of Y_{Fe} surrounded by 3 V_{Fe} vacancies (Fig. 5.4c) result in yttrium

atom displacement by 1.28 Å accompanied by donation of electronic charge 1.40 *e* to the closest lattice atoms. This configuration is described by the highest binding energy. In all the cases, the yttrium impurity atom moves to the central position between the V_{Fe} vacancies.

Table 5.14. Calculated parameters of Y_{Fe} substitute surrounded by V_{Fe} vacancies

Configuration	E_{bind}, eV	Δq, e* (Y_{Fe})	δr_Y, Å
Y_{Fe}-2V_{Fe} (1NN)	4.10	1.52	1.03
Y_{Fe}-2V_{Fe} (2NN)	2.37	1.24	0.61
Y_{Fe}-3V_{Fe}	5.17	1.40	1.28

*estimated within the Bader topological analysis [90]

Table 5.15. Calculated parameters for two Y_{Fe} atoms at different distances from V_{Fe} vacancy

Configuration	E_{bind}, eV	Δq, e* (Y_{Fe})	δr_Y (1), Å	δr_Y (2), Å
Y_{Fe}-V_{Fe}-Y_{Fe} 2NN	1.76	1.04	0.31	0.31
Y_{Fe}-V_{Fe}-Y_{Fe} 3NN	2.26	1.07	0.44	0.59
Y_{Fe}-V_{Fe}-Y_{Fe} 4NN	2.32	1.04	0.19	1.31

*estimated within the Bader topological analysis [90]

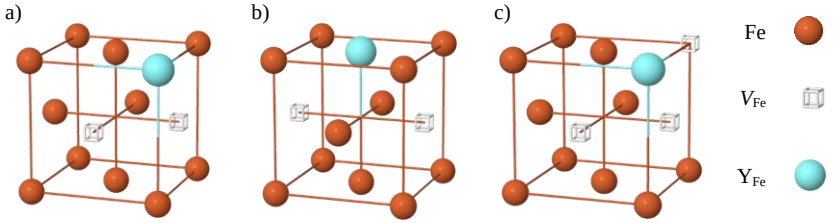

Figure 5.4. Three models of Y_{Fe} substitute in *fcc*-Fe unit cells surrounded by two and three V_{Fe} vacancies:
a) Y-2V_{Fe} (1NN) b) Y-2V_{Fe} (2NN) c) Y-3V_{Fe}

Essential influence of V_{Fe} vacancy on Y_{Fe} substitutes is also confirmed by simulations of defect configurations in *fcc*-lattice containing two Y_{Fe} atoms and single V_{Fe} vacancy *per* unit cell (Figs. 5.5a-c) where two yttrium atoms are located at the increasing relative distances: 2NN, 3NN and 4NN (Table 5.15) while V_{Fe} is posititioned at 1NN distance relatively to both Y_{Fe} {P4]. The binding energy E^{bind} increases noticeably when going from 2NN to 3NN and seems to be saturated at larger distances. Both Y_{Fe} atoms are symmetrically shifted inside 2NN configuration donating ~1 *e* to the nearest Fe atoms (Table 5.15). In the configuration when both Y_{Fe} atoms are located at 4NN distance, first atom is displaced by 0.19 Å, while the second moves towards V_{Fe} vacancy by 1.31 Å.

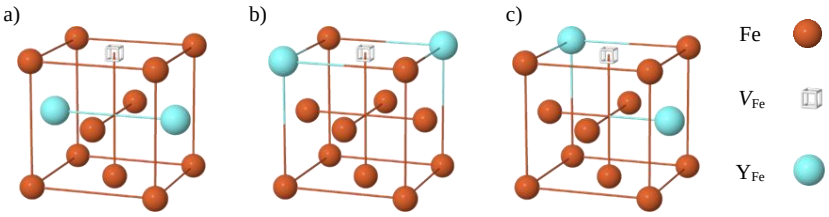

Figure 5.5. Three models of V_{Fe} vacancy in *fcc*-Fe unit cells surrounded by two Y_{Fe} substitutes each:
a) Y_{Fe}-V_{Fe}-Y_{Fe} 2NN b) Y_{Fe}-V_{Fe}-Y_{Fe} 3NN c) Y_{Fe}-V_{Fe}-Y_{Fe} 4NN

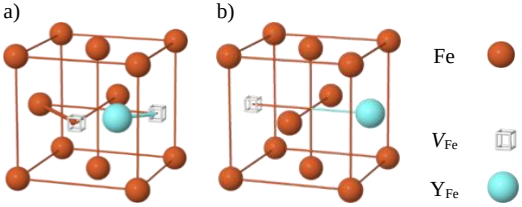

Figure 5.6. Initial (a) and final (b) supercell configurations for migration of Y_{Fe} atom surrounded by two V_{Fe}.

Table 5.16. NEB simulation of Y_{Fe} migration.

Configuration	Energy barrier (eV)
Y_{Fe}-V_{Fe}(1NN)	2.60
Y_{Fe}-V_{Fe}(2NN)	2.37
Y_{Fe}-V_{Fe}(3NN)	1.85
Y_{Fe}-V_{Fe}(4NN)	1.81

The NEB method implemented within VASP code [41] (Subsection 3.4) is used in the current study for optimization of migration trajectory for yttrium impurity (Figures 5.6a,b) and other defects as well as determination of the diffusion barriers (*e.g.*, Table 5.16) [P4]. It is clearly seen that the energy barrier decreases with the growth of distance between Y_{Fe} impurity atom and V_{Fe} vacancy. This can be explained by the fact that the distance between migrating and regular atoms in the lattice along the migration paths are smaller when Y_{Fe} and V_{Fe} are closer to each other. Thus, the repulsing forces grow and increase the energy barriers. On the contrary, with the increase of the distance between Y_{Fe} and V_{Fe} the energy barriers decrease. These results illustrate influence of vacancies on migration path of Y atoms in *fcc* Fe lattice. In order to receive accurate results for energy barriers, we have used seven intermediate configurations for the NEB calculations of the optimized migration paths. The results of performed large scale *ab initio* calculations will be used in the LKMC simulations of the ODS cluster formation.

5.3. Atom-substituted triple-wise defects

5.3.1. Y_{Fe}-O-Y_{Fe} configurations

In order to study how O impurity atom might affect the binding energies between the two Y_{Fe} atoms, two Ti_{Fe} atoms as well as between Y_{Fe} and Ti_{Fe} atoms, both Bader charges and relative atomic displacements have been calculated and analysed for a number of models described below [P4,P6]. The results systematized in Table 5.17 correspond to the schematic models shown in Figs.

5.7a-c. The O_{Fe} atom is positioned as the first nearest neighbour (1NN) to both Y_{Fe} atoms in all cases. It is important to note that the size of Y atom is noticeably larger than that of Fe atoms, which leads to the expansion of the coordination spheres around the Y_{Fe} atoms. A noticeable O_{Fe} atom displacement occurs during the relaxation of all three calculated configurations. The expansion of the coordination spheres around Y_{Fe} atoms noticeably pushes a smaller O_{Fe} atom away from both Y_{Fe} atoms by 0.24 Å, while the distance between Y_{Fe} atoms increases by 0.14 Å in the 1NN configuration (Fig. 5.7a and Table 5.17).

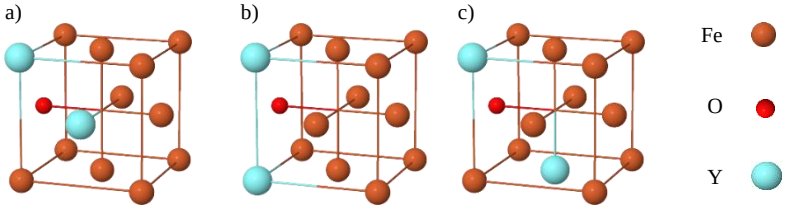

Figures 5.7. Model of O_{Fe} atom bound to 2 nearest Y_{Fe} atoms as 1NN, interatomic distance of which is:

a) 1NN b) 2NN c) 3NN

O_{Fe} is pushed away from both Y_{Fe} atoms by 0.13 Å towards Fe atoms, while the distance between two 2NN Y_{Fe} atoms decreases by 0.42 Å (Fig. 5.7b and Table 5.17). In the 3NN configuration, the distance between O_{Fe} and both Y_{Fe} atoms decreases by 0.09 Å, while the distance between the two Y_{Fe} atoms is almost unchanged (the latter become closer by 0.01 Å). The described atom displacements can explain the values of the binding energies. The smallest binding energy are found between the defects when they are positioned as 1NN, the binding energies increased with the increase of the distance between the two Y_{Fe} atoms with the largest binding energy of 2.20 eV calculated for the 3NN configuration (Fig. 5.7c and Table 5.17).

Table 5.17. Calculated parameters for two Y_{Fe} and one O_{Fe} atoms

Configuration	E_{bind}, eV	Δq, e^* (Y_{Fe})	Δq, e^* (Y_{Fe})	Δq, e^* (O_{Fe})	δr_Y (1), Å	δr_Y (2), Å	δr_O, Å
1NN**	1.12	1.06	1.08	-1.16	0.27	0.27	0.64
2NN**	2.00	1.17	1.17	-1.19	0.36	0.36	0.64
3NN**	2.20	1.23	1.23	-1.19	0.45	0.45	0.60

*estimated within the Bader topological analysis [90];
**configuration of two Y_{Fe} atoms in *fcc*-Fe.

Difference charge electron density maps shown in Figs. 5.8-5.10 confirm the conclusions of the Bader charge analysis describing the electron charge redistribution: oxygen atom attracts electrons (red isolines around O atom show the increase of the electron charge around it) while Y atoms donate electrons (blue isolines around these atoms show decrease of the electron charge) [P4,P6]. It is obvious that morphology of charge distribution along the cross-section plane in Figure 5.9 is different from those in Figures 5.8 and 5.10. Figures 5.8-5.10 also demonstrate that despite the high affinity of oxygen atom towards yttrium

atoms, O_{Fe} atom is displaced in opposite direction from Y_{Fe} towards Fe atoms during the relaxation sharing additional electron charge with them. The Bader analysis shows that Y_{Fe} atoms donate 1.06-1.23 *e*, while O atom attracts 1.16-1.19 *e*.

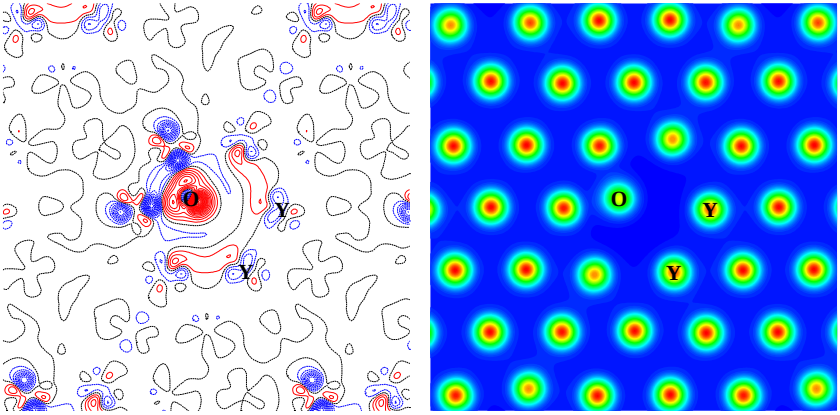

Figure 5.8. Difference and total electron charge density maps for the first type of Y_{Fe}-O_{Fe}-Y_{Fe} configurations (1NN for Y_{Fe} atoms), where O_{Fe} atom is the first nearest neighbour for each of Y_{Fe}. Solid (red), dash (blue) and dash-dot (black) isolines (with the increment of 0.002 *e*/Å^3) represent positive, negative and neutral electronic charge, respectively.

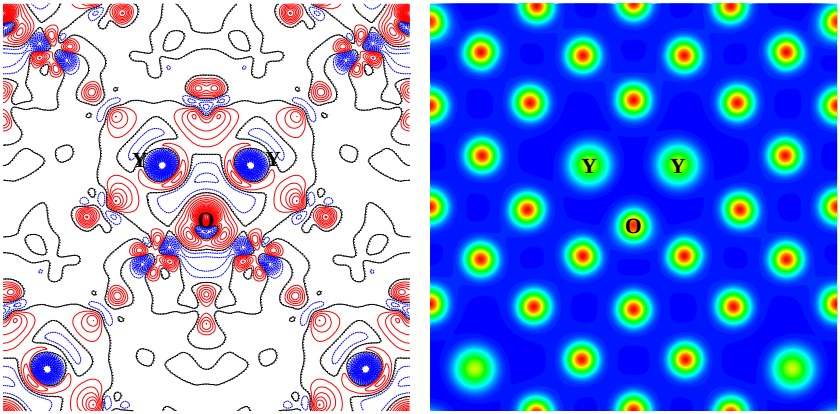

Figure 5.9. Difference and total electron charge density maps for the second type of Y_{Fe}-O_{Fe}-Y_{Fe} configurations (2NN for Y_{Fe} atoms), where O_{Fe} atom is the first nearest neighbour for each of Y_{Fe}. Solid (red), dash (blue) and dash-dot (black) isolines (with the increment of 0.002 *e*/Å^3) represent positive, negative and neutral electronic charge, respectively.

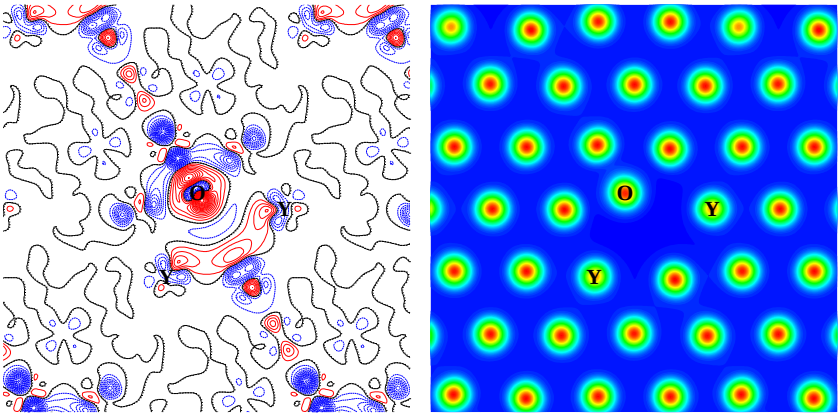

Figure 5.10. Difference and total electron charge density maps for the third type of Y_{Fe}-O_{Fe}-Y_{Fe} configurations (3NN for Y_{Fe} atoms), where O_{Fe} atom is the first nearest neighbour for each of Y_{Fe}. Solid (red), dash (blue) and dash-dot (black) isolines (with the increment of 0.002 e/Å^3) represent positive, negative and neutral electronic charge, respectively.

The results of the calculations on the unit cells configurations containing oxygen atom shifted to octahedral site O_{oct} shown in Figs. 5.11a,b are presented in Table 5.18. The atom displacements for the configuration where Y_{Fe} atom is positioned as 1NN are qualitatively similar to the ones observed for the configurations with Y_{Fe}-O_{Fe}-Y_{Fe}, *i.e.*, in this case both Y_{Fe} atoms expand the coordination sphere around themselves pushing O_{Fe} atom away increasing the distance between O_{Fe} and both Y_{Fe} atoms by 0.45 Å, while the distance between two Y_{Fe} atoms increases by 0.38 Å [P6]. However, the results of calculations on the configuration when Y_{Fe} atoms are placed as 2NN are different from those described above. This difference originates from the position of O_{oct} atom and the forces acting on it during the relaxation. In this configuration, interstitial oxygen is positioned symmetrically relatively to both yttrium atoms in the first coordination sphere and the forces from the Fe and Y atoms located in the first coordination sphere around O_{oct} are compensating each other. This results in no displacement of O_{oct} atom in relation to its initial position during the relaxation. At the same time, both Y_{Fe} atoms are displaced away from O_{Fe} atom by 0.34 Å and by 0.69 Å from each other. No binding energies have been found between the defects as shown in Table 5.18.

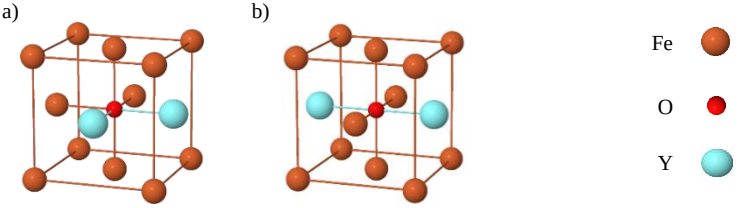

Figure 5.11. Two Y_{Fe} atoms as 1NN (a) and 2NN (b), while O_{oct} is in the first coordiantion sphere for both.

Table 5.18. Calculated parameters for two Y_{Fe} and one O_{oct} atoms

Configuration	E_{bind}, eV	Δq, e^* (Y_{Fe})	Δq, e^* (Y_{Fe})	Δq, e^* (O_{oct})	δr_Y (1), Å	δr_Y (2), Å	δr_O, Å
1NN**	-0.60	1.11	1.11	-1.35	0.23	0.23	0.29
2NN**	-0.32	1.16	1.16	-1.37	0.34	0.34	0.00

*estimated within the Bader topological analysis [90]

**distance between two Y_{Fe} atoms, O_{oct} is in the first coordination sphere related to both Y atoms

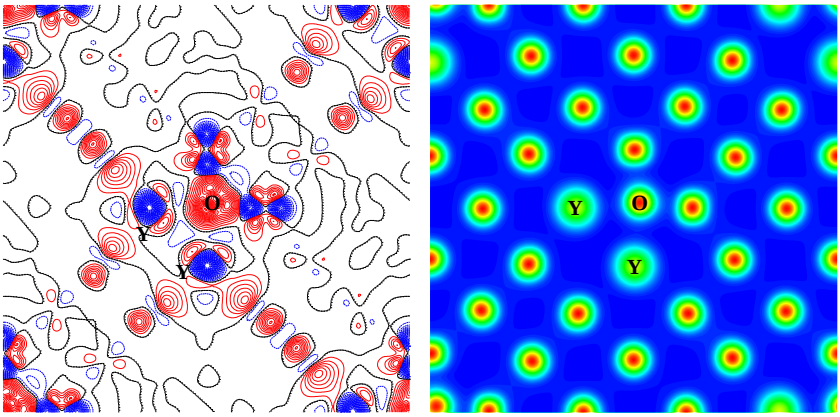

Figure 5.12. Difference and total electron charge density maps for Y_{Fe}-O_{oct}-Y_{Fe} 1NN, where oxygen interstitial is located in the first coordination sphere to both Y_{Fe} atoms. Solid (red), dash (blue) and dash-dot (black) isolines (with the increment of 0.002 e/Å^3) represent positive, negative and neutral electronic charge.

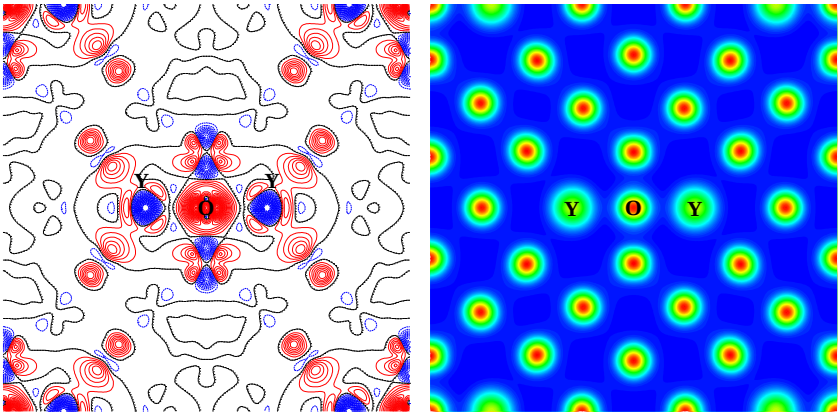

Figure 5.13. Difference and total electron charge density maps for Y_{Fe}-O_{oct}-Y_{Fe} 2NN, where oxygen interstitial is located in the first coordination sphere to both Y_{Fe} atoms. Solid (red), dash (blue) and dash-dot (black) isolines (with the increment of 0.002 e/Å^3) represent positive, negative and neutral electronic charge.

Difference charge electron density maps shown in Figs. 5.12 and 5.13 support the conclusions of the Bader charge analysis describing the electron charge redistribution. O atom attracts electrons (red isolines around O atom show the increase of the electron charge around it) while Y atom donate them (blue isolines around the latter show decrease of the electron charge). It is obvious from Figure 5.12 that Y_{Fe} atoms cause the shift of O atom towards the closest Fe atoms during the relaxation sharing additional electron charge with them. As the defect atom positions in Y_{Fe}–O_{oct}–Y_{Fe} 2NN configuration are symmetric, *e.g.*, O atom remains unchanged during the relaxation while the distance between Y atoms increases as it can be observed in Figure 5.13. Y_{Fe} atoms donates about the same electronic charge (1.11-1.16 *e*) as for the configurations described in Table 5.17, however, O atoms attracts a noticeable larger electronic charge (1.35-1.37 *e*).

5.3.2. Ti_{Fe}-O-Ti_{Fe} configurations

Table 5.19 systematizes results of our calculations on the models of Ti-O precipitates at *fcc*-Fe lattice shown in Figures 5.14a-c. The size of Ti atoms is quite similar (marginally smaller) to that of Fe atoms which means that Ti_{Fe} substitutes possess almost no effect on the coordination sphere around themselves [P6]. Noticeable attraction of O_{Fe} atoms by 0.34 Å towards Ti_{Fe} atoms occurs, while both titanium impurity atoms have been displaced by 0.18 Å from each other. The smallest binding energy (0.88 eV) has been observed for the configuration where Ti_{Fe} atoms are placed as the 1NN neighbours and the binding energy of 1.35 eV is calculated for the 3NN positions of Ti_{Fe}. In the 3NN configuration, the distance between O_{Fe} and both Ti_{Fe} atoms decreases by 0.47 Å, while the distance between both Ti_{Fe} atoms is reduced by 0.32 Å.

Table 5.19. Calculated parameters for two Ti_{Fe} and one O_{Fe} atoms

Configuration	E_{bind}, eV	Δq, e^* (Ti_{Fe})	Δq, e^* (Ti_{Fe})	Δq, e^* (O_{Fe})	$\delta r_{Ti\,(1)}$, Å	$\delta r_{Ti\,(2)}$, Å	δr_{O}, Å
1NN**	0.88	1.15	1.15	-1.22	0.22	0.22	0.86
2NN**	1.58	1.22	1.22	-1.27	0.20	0.20	1.58
3NN**	1.35	1.24	1.24	-1.18	0.22	0.22	0.81

*estimated within the Bader topological analysis [90]

**distance between two Ti_{Fe} atoms, O_{Fe} is the 1NN to both Ti_{Fe} atoms

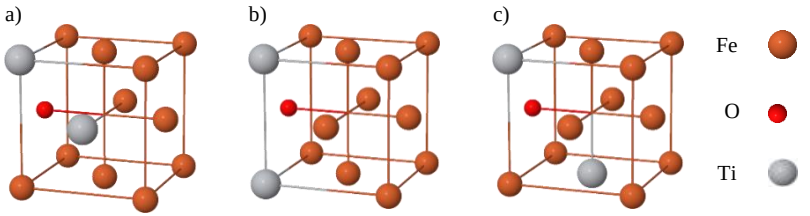

Figure 5.14. Models of two Ti_{Fe} atoms coordinated as 1NN (a), 2NN(b) and 3NN (c), respectively, while O_{Fe} is the 1NN for both Ti_{Fe} atoms.

A significant displacement of the O_{Fe} atom is observed for all three configurations (0.86 Å, 1.58 Å, and 0.81 Å for the 1NN, 2NN, and 3NN, respectively). In these configurations, oxygen atom is displaced from the initial O_{Fe} position towards O_{oct} position, which is clearly visible from the total electron charge density maps shown in Figs. 5.15-5.17. Oxygen atom is shifted very close to O_{oct} position during the relaxation of 1NN and 3NN configurations, while it occupies exactly O_{oct} position after the relaxation of 2NN configuration. Such a displacement causes the local expansion of the coordination sphere around O_{Fe} increasing the distance between Ti_{Fe} atoms by 0.36 Å, while the distance between O_{Fe} and both Ti_{Fe} atoms noticeably decreases (by 0.53 Å). This explains that largest binding energy between these defects (1.58 eV) has been found for the 2NN configuration.

Difference charge electron density plots shown in Figures 5.15-5.17 are backed up by the Bader charge analysis describing the electron charge redistribution [P6]. Oxygen atom attracts electrons (red isolines around O atom show the increase of the electron charge around it) while Ti atoms donate electrons (blue isolines around these atoms show decrease of the electron charge around them). Figs. 5.22-5.24 show the high isoline density between the defects. The Bader analysis shows that Ti_{Fe} atoms donate 1.15-1.24 *e*, while O_{Fe} attracts 1.18-1.27 *e*.

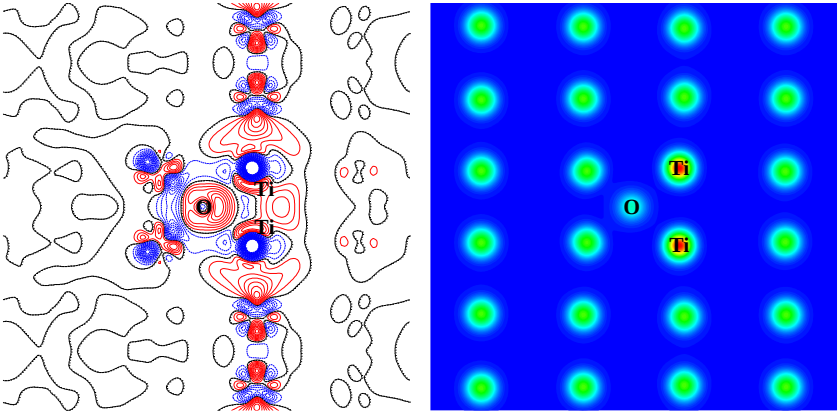

Figure 5.15. Difference and total electron charge density maps for the first type of Ti_{Fe}-O_{Fe}-Ti_{Fe} configurations (1NN for Ti_{Fe} atoms), where O_{Fe} atom is the first nearest neighbour for each of Ti_{Fe}. Solid (red), dash (blue) and dash-dot (black) isolines (with the increment of 0.002 *e*/Å^3) represent positive, negative and neutral electronic charge, respectively.

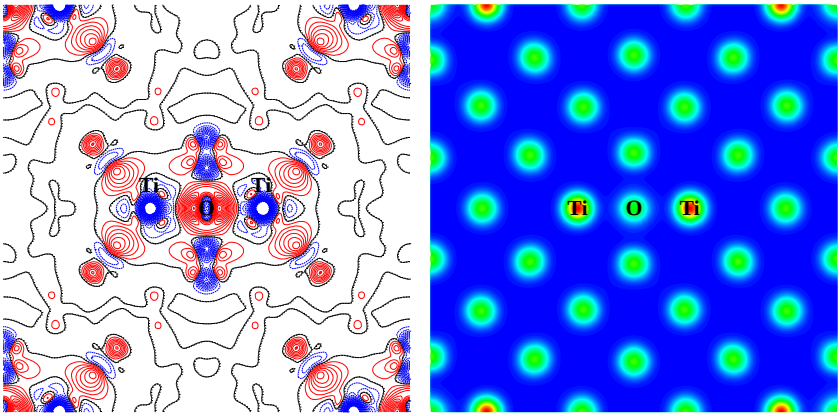

Figure 5.16. Difference and total electron charge density maps for the second type of Ti_{Fe}-O_{Fe}-Ti_{Fe} configurations (2NN for Ti_{Fe} atoms), where O_{Fe} atom is the first nearest neighbour for each of Ti_{Fe}. Solid (red), dash (blue) and dash-dot (black) isolines (with the increment of 0.002 e/Å^3) represent positive, negative and neutral electronic charge, respectively.

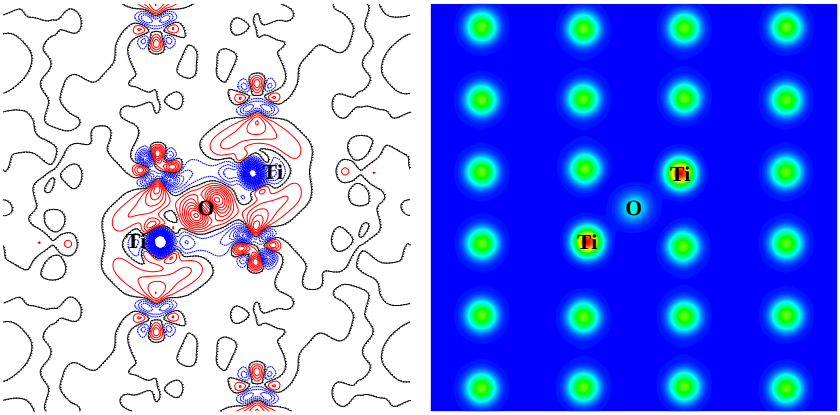

Figure 5.17. Difference and total electron charge density maps for the third type of Ti_{Fe}-O_{Fe}-Ti_{Fe} configurations (3NN for Ti_{Fe} atoms), where O_{Fe} atom is the first nearest neighbour for each of Ti_{Fe}. Solid (red), dash (blue) and dash-dot (black) isolines (with the increment of 0.002 e/Å^3) represent positive, negative and neutral electronic charge, respectively.

The results presented in Table 5.20 for the models of Ti-O precipitate at *fcc*-Fe shown in Figs. 5.18a and 5.18b are similar to those presented in Table 5.16, *i.e.*, no binding energy is observed between Ti_{Fe} and O_{oct} atoms. The slight displacement of Ti_{Fe} atoms during the relaxation is observed while only a marginal displacement of O_{oct} takes place when Ti_{Fe} atoms are positioned as 1NN, and no displacement of O_{oct} is observed when Ti_{Fe} atoms are positioned as 2NN neighbours. In the 1NN configuration, the distance between O_{oct} and both Ti_{Fe} atoms is increased by 0.26 Å, while the distance between Ti_{Fe} atoms is reduced by 0.20 Å. In the 2NN configuration, the distance between O_{Fe} and both Ti_{Fe} atoms is grown by 0.21Å, while the distance between Ti_{Fe} atoms is increased

by 0.35 Å. These results are quite similar to those mentioned above for the Y_{Fe}-O_{oct}-Y_{Fe} configurations.

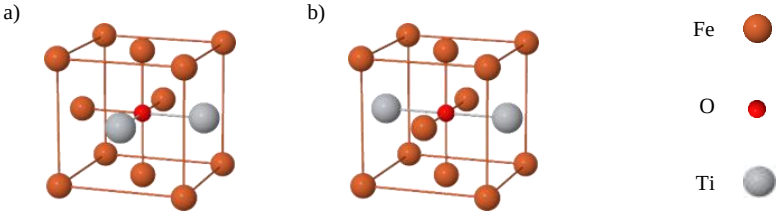

Figures 5.18. Two Ti_{Fe} atoms as 1NN (a) and 2NN (b), and O_{oct} in the first coordiantion sphere around them.

Table 5.20. Calculated parameters for two Ti_{Fe} and one O_{oct} atoms

Configuration	E_{bind}, eV	Δq, e^* (Ti_{Fe})	Δq, e^* (Ti_{Fe})	Δq, e^* (O_{oct})	$\delta r_{Ti\,(1)}$, Å	$\delta r_{Ti\,(2)}$, Å	δr_O, Å
1NN**	-0.94	1.14	1.14	-1.38	0.20	0.20	0.07
2NN**	-0.90	1.17	1.17	-1.39	0.21	0.21	0.00

*estimated within the Bader topological analysis [90]

**distance between two Ti_{Fe} atoms where O_{oct} is in the first coordination sphere relatively to both Ti_{Fe} atoms

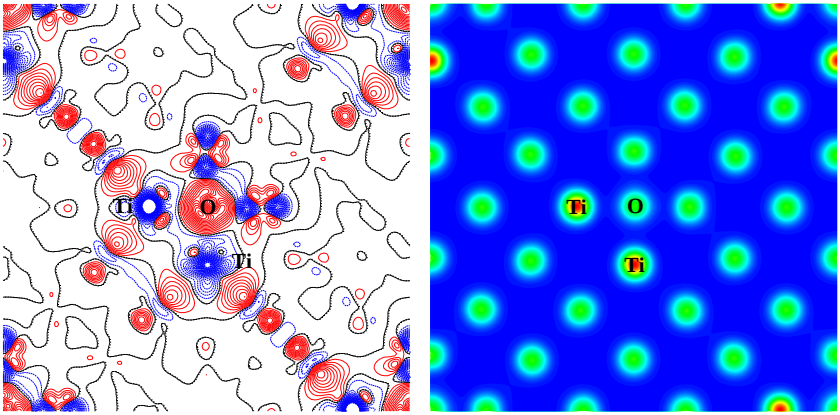

Figure 5.19. Difference and total electron charge density maps for Ti_{Fe}-O_{oct}-Ti_{Fe} 1NN, where oxygen substitute atom is located in the first coordination sphere to both Ti atoms. Solid (red), dash (blue) and dash-dot (black) isolines (with the increment of 0.002 e/Å^3) represent positive, negative and neutral electronic charge, respectively.

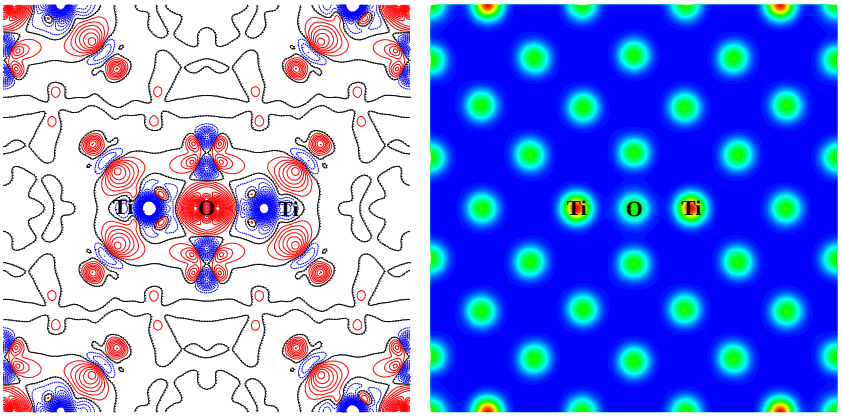

Figure 5.20. Difference and total electron charge density maps for Ti_{Fe}-O_{oct}-Ti_{Fe} 2NN, where O atom is located in the first coordination sphere to both Ti atoms. Solid (red), dash (blue) and dash-dot (black) isolines (with the increment of 0.002 e/Å^3) represent positive, negative and neutral electronic charge, respectively.

Difference charge electron density maps shown in Figures 5.19-5.20 confirm the conclusions of the Bader charge analysis describing the electron charge redistribution. Oxygen atom attracts electrons (red isolines around O atom show the increase of the electron charge) while Ti atoms donate electrons (blue isolines around these atoms show the decrease of the electron density). It is obvious from Figure 5.19 that Ti_{Fe} atoms cause the shift of O atom towards the closest iron atoms during the relaxation sharing additional electron charge with them. As the defect atom positions in Ti_{Fe}-O_{oct}-Ti_{Fe} 2NN configuration are symmetric, the position of O atom remains unchanged during the relaxation while the distance between Ti atoms increases as it can be observed in Figure 5.17. Ti_{Fe} atoms donate 1.14-1.17 e, while O_{Fe} attracts 1.38-1.39 e.

5.3.3. Ti_{Fe}-O-Y_{Fe} configurations

Atomistic models of Ti-O-Y precipitate in *fcc*-Fe lattice shown in Figs. 5.21a-c have been calculated *ab initio* [P6]. The binding energies and other parameters of these defects presented in Table 5.21 are found to be similar to those reported in Table 5.17 for Y-O-Y. It means that the smallest binding energy of 1.34 eV is estimated for the 1NN configuration and the value of the binding energy increases with the increase of the distance between Y_{Fe} and Ti_{Fe} up to 2.04 eV and 2.18 eV for the 2NN and 3NN distances respectively. Similarly, a noticeable displacement of O_{Fe} atom is observed as well. It is worth noting that the displacement of O_{Fe} atom for the configurations presented in Table 5.21 are larger than those reported in Table 5.17 and smaller than those reported in Table 5.19. Thus, when comparing these three Tables, the smallest O_{Fe} displacements are observed in the configurations with two Y_{Fe} atoms, while the largest O_{Fe} displacement is achieved in the configurations containing two Ti_{Fe} atoms. Table

5.21 shows the results obtained for impurity configuration containing one Y_{Fe}, one Ti_{Fe}, and one O_{Fe} atoms, so the results of these calculations seem to be quite logical. As described above, Y_{Fe} atoms expand the coordination sphere around itself while the coordination sphere around both Ti_{Fe} and O_{Fe} atoms shrinks. As a result, during the relaxation of the 1NN configuration the distance between Y_{Fe} and O_{Fe} decreases by 0.21 Å, and the noticeable decrease of distance between Ti_{Fe} and O_{Fe} (by 0.49 Å is observed), while the distance between Y_{Fe} and Ti_{Fe} increases by 0.24 Å. The distance between Y_{Fe} and O_{Fe} decreases by 0.13 Å, the distance between T_{Fe} and O_{Fe} decreases by 0.41 Å, while the distance between Y_{Fe} and Ti_{Fe} decreases by 0.46 Å in the 2NN configuration. Analogously, the distance between Y_{Fe} and O_{Fe} decreases by 0.16 Å, the distance between T_{Fe} and O_{Fe} decreases by 0.41 Å, while the distance between Y_{Fe} and Ti_{Fe} decreases by 0.91 Å in the 3NN configuration. The atomic displacements listed in Table 5.21 can probably explain the values of binding energy between the defects.

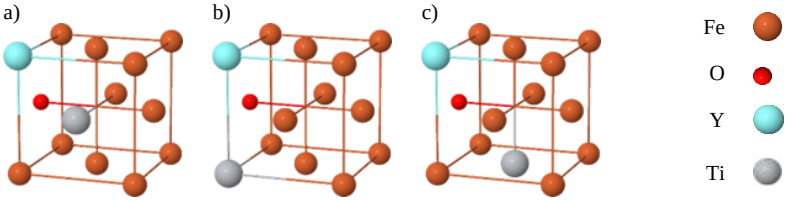

Figures 5.21. Model of Y_{Fe} and Ti_{Fe} atoms as 1NN (a), 2NN (b) and 3NN (c) neighbours, while O_{Fe} as the 1NN to both Y_{Fe} and Ti_{Fe} atoms.

Table 5.21 Calculated parameters for Y_{Fe}, Ti_{Fe}, and O_{Fe} atoms

Configuration	E_{bind}, eV	Δq, e^* (Y_{Fe})	Δq, e^* (Ti_{Fe})	Δq, e^* (O_{Fe})	δr_Y, Å	δr_{Ti}, Å	δr_O, Å
1NN**	1.34	1.24	1.11	-1.19	0.45	0.35	0.95
2NN**	2.04	1.23	1.17	-1.23	0.86	0.09	0.87
3NN**	2.18	1.24	1.20	-1.24	0.91	0.15	0.76

*estimated within the Bader topological analysis [90]
**distance between Y_{Fe} and Ti_{Fe} atoms, O_{Fe} is the 1NN to both Y_{Fe} and Ti_{Fe} atoms

Difference charge electron density maps shown in Figs. 5.22-5.24 confirm the conclusions of the Bader charge analysis describing the electron charge redistribution. O atom attracts electron density (red isolines around O atom show the increase of the electron charge) while Y and Ti atoms donate electrons (blue isolines around these atoms show decrease of the electron charge). It is obvious that similarly to Y_{Fe}-O_{Fe}-Y_{Fe} configurations morphology of charge distribution along the cross-section plane in Figure 5.23 is different from those in Figs 5.22 and 5.24. All the Figures demonstrate the higher affinity of O atom towards Ti atom compared to Y atom, which is indicated by the higher density of the isolines between Ti and O atoms. In these configurations, Y_{Fe} donates 1.23-1.24 *e*, Ti_{Fe} donates 1.11-1.24 *e*, while O_{Fe} attracts 1.19-1.24 *e*.

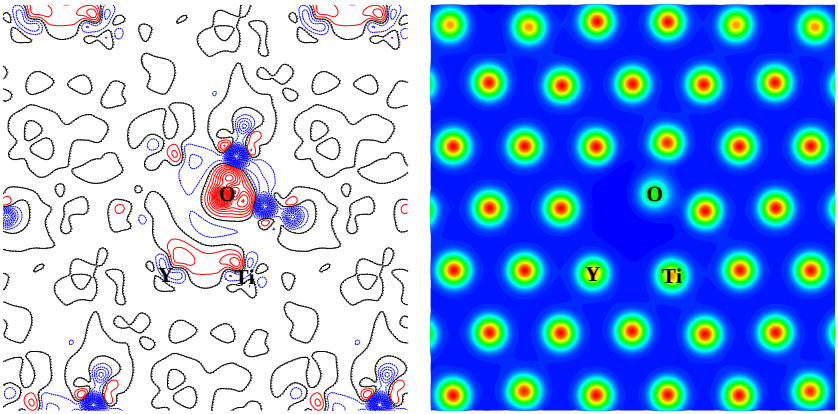

Figure 5.22. Difference and total electron charge density maps for Y_{Fe}-O_{Fe}-Ti_{Fe} 1NN, where oxygen substitute atom is the first nearest neighbour (1NN) for both Y and Ti atoms. Solid (red), dash (blue) and dash-dot (black) isolines (with the increment of 0.002 e/Å^3) represent positive, negative and neutral electronic charge, respectively.

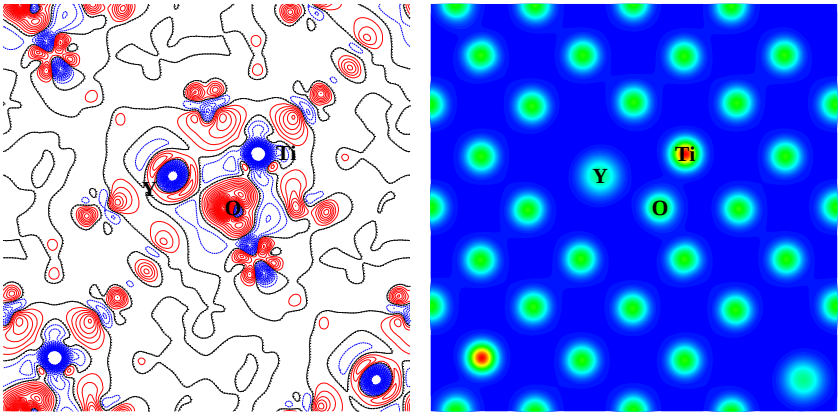

Figure 5.23. Difference and total electron charge density maps for Y_{Fe}-O_{Fe}-Ti_{Fe} 2NN, where oxygen substitute atom is the first nearest neighbour (1NN) for both Y and Ti atoms. Solid (red), dash (blue) and dash-dot (black) isolines (with the increment of 0.002 e/Å^3) represent positive, negative and neutral electronic charge, respectively.

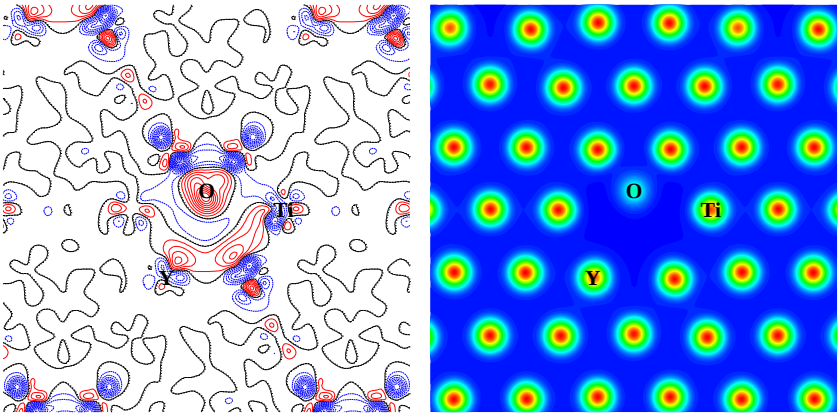

Figure 5.24. Difference and total electron charge density maps for Y_{Fe}-O_{Fe}-Ti_{Fe} 3NN, where oxygen substitute atom is the first nearest neighbour (1NN) for both Y and Ti atoms. Solid (red), dash (blue) and dash-dot (black) isolines (with the increment of 0.002 e/Å^3) represent positive, negative and neutral electronic charge, respectively.

The results presented in Table 5.22 for the models of interstitial oxygen shown in Figs. 5.25a and 5.25b are similar to those presented in Tables 5.18 and 5.20, *i.e.*, no binding energies are found between the defects in these cases [P6]. Only slight atom shifts is observed during the relaxations of both configurations. It should be noted that as opposed to O_{Fe}, which results in the decrease of the coordination sphere around itself, O_{oct} causes the expansion of the corresponding coordination sphere. In the 1NN configuration, the distance between O_{oct} and Y_{Fe} increases by 0.44 Å, the distance between O_{oct} and Ti_{Fe} increases by 0.26 Å, while the distance between Y_{Fe} and Ti_{Fe} increases by 0.38 Å. It is worth mentioning that the configuration when Y_{Fe} and Ti_{Fe} atoms are positioned as the 2NN is different from the ones described in Tables 5.16 and 5.18, while in the latter configuration, the forces between pairs of Y_{Fe} or Ti_{Fe} atoms are compensating each other and result in the absence of the displacement of O_{oct} atom. It is obvious that the resulting force of Y_{Fe} and Ti_{Fe} atoms acting on O_{oct} atom is not equal to 0, which explains the displacement of O_{oct} atom in the configuration when Y_{Fe} and Ti_{Fe} are the 2NN. In the latter, the distance between O_{oct} and Y_{Fe} increases by 0.41 Å, between O_{oct} and Ti_{Fe} increases by 0.16 Å, while the distance between Y_{Fe} and Ti_{Fe} increases by 0.58 Å.

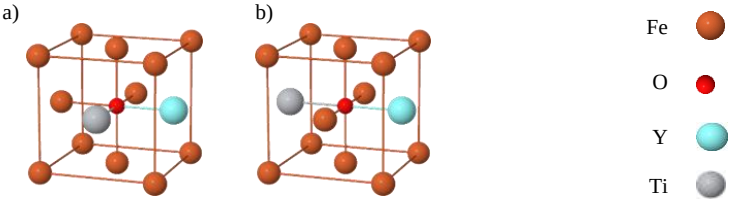

Figure 5.25. Y_{Fe} and Ti_{Fe} atoms as 1NN (a) and 2NN (b), and O_{oct} in the first coordiantion sphere around them.

Table 5.22. Calculated parameters for Y_{Fe}, Ti_{Fe}, and O_{oct} atoms

Configuration	E_{bind}, eV	Δq, e* (Y_{Fe})	Δq, e* (Ti_{Fe})	Δq, e* (O_{oct})	δr_Y, Å	δr_{Ti}, Å	δr_O, Å
1NN**	-0.76	1.14	1.12	-1.36	0.24	0.21	0.20
2NN**	-0.68	1.19	1.18	-1.38	0.25	0.32	0.15

*estimated within the Bader topological analysis [90]

**distance between Y_{Fe} and Ti_{Fe} atoms, O_{oct} is in the first coordination sphere relatively to both Y_{Fe} and Ti_{Fe} atoms

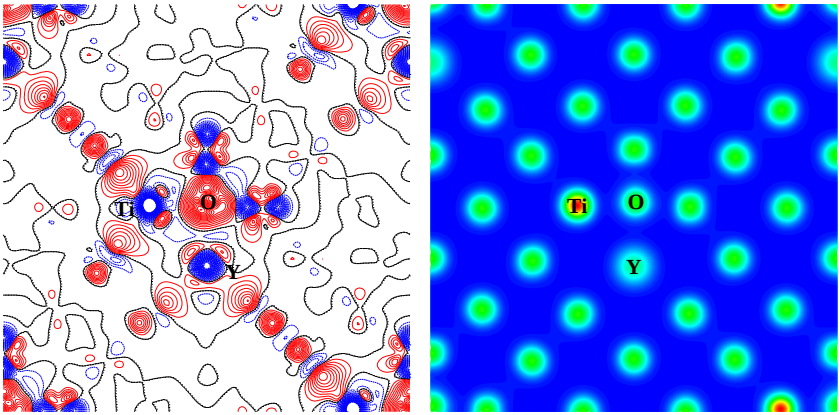

Figure 5.26. Difference and total electron charge density maps for Y_{Fe}-O_{oct}-Ti_{Fe} 1NN, where oxygen substitute atom is located in the first coordination sphere to both Y and Ti atoms. Solid (red), dash (blue) and dash-dot (black) isolines (with the increment of 0.002 e/Å^3) represent positive, negative and neutral electronic charges.

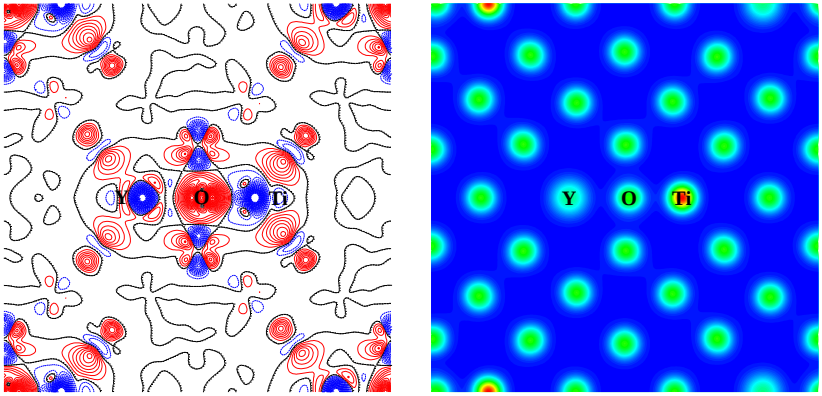

Figure 5.27. Difference and total electron charge density maps for Y_{Fe}-O_{oct}-Ti_{Fe} 2NN, where oxygen substitute atom is located in the first coordination sphere to both Y and Ti atoms. Solid (red), dash (blue) and dash-dot (black) isolines (with the increment of 0.002 e/Å^3) represent positive, negative and neutral electronic charges.

Difference charge electron density plots shown in Figs. 5.26 and 5.27 confirm the conclusions of the Bader charge analysis describing the electron charge redistribution. O_{oct} atom attracts electrons (red isolines around O atom

show the increase of the electron charge) while Ti_{Fe} atoms donate them (blue isolines around atoms show decrease of the electron charge). It is obvious from both Figures that Y_{Fe} atoms causes the shift of O atom towards the closest Ti and Fe atoms during the relaxation sharing additional electron charge with them. Similarly, to the Y_{Fe}-O_{Fe} configurations the higher affinity between O_{oct} and Ti_{Fe} atoms is observed compared to the affinity between O and Y atoms. Y_{Fe} donates 1.14-1.19 *e*, Ti_{Fe} donates 1.12-1.18 *e*, while O_{Fe} attracts 1.36-1.38 *e*.

On the whole, analysis of results discussed in Section 5 shows that in growing Me_{Fe}-O_{Fe}-Me_{Fe} blocks of ODS nanoclusters in *fcc*-Fe, a preference can be given to Y_{Fe}-O_{Fe} fragments, due to a noticeably higher binding energies in them as follows from Tables 5.8 and 5.9 as well as higher concentration of yttrium atoms in nanoparticles according to technological parameters of ODS synthesis in steels as described in Subsection 2.1.1.1. At the same time, arrangement of yttrium atoms inside interstitial centers of lattice is energetically unprofitable. Obviously, even higher Y atom migration barriers in *fcc*-Fe lattice cannot brake formation of Y_{Fe}-O_{Fe} fragments in ODS particles because of essential influence of V_{Fe} vacancies to relief interlattice migration of yttrium.

6. Summary

The presented PhD Thesis is the first systematized first principles description of interactomic interactions in ODS nanoclusters synthesized in *fcc*-Fe. The chosen approach for the *ab initio* calculations performed on *fcc* Fe lattice has been tested on basic parameters such as lattice constant, bulk modulus cohesive energy as well as on V_{Fe} vacancy formation energy. The results of the calculations are in a good agreement with both experimental data as well as with other theoretical studies. This means that the methods used in this work allow getting the plausible results.

DFT PAW method has been used to perform large-scale calculations on the basic properties of bulk *fcc*-Fe lattice and the effects of single vacancy, O, Ti and Y impurities on those properties. Such properties of the bulk *fcc*-Fe lattice as lattice constant, bulk modulus, and cohesive energy have been calculated being in a good qualitative agreement. The formation energies of the single defects as well as the vacancy formation energy have been assessed. The latter is in a good agreement with other simulations. It has been found that the the supercell with the extension of 4×4×4, the cut-off energy of 800eV, and the *k*-point mesh of 7×7×7 are required to achieve the plausible results.

The modeling of the *pair-wise* dopant interactions in *fcc*-Fe lattice has been performed for Y_{Fe}–Y_{Fe}, Y_{Fe}–V_{Fe}, Y_{Fe}–O_{Fe}, Y_{Fe}–O_{oct}, Ti_{Fe}–Ti_{Fe}, Ti_{Fe}–V_{Fe}, Ti_{Fe}–O_{Fe}, Ti_{Fe}–O_{oct}, O_{Fe}–O_{Fe}, V_{Fe}–V_{Fe}, and O–V_{Fe} defect pairs in *fcc*-Fe lattice at different mutual distances followed by the calculations of the more complex defect configurations such as the configurations with three and four V_{Fe} as well as yttrium impurity atom with two and three V_{Fe} vacancies (O_{Fe} atoms substitute

regular Fe atoms in their positions while O_{oct} atoms occupy octahedral interstitials in the lattice) .
The large-scale calculations of atom-substituted *triple-wise* interactions between Y_{Fe}–O_{Fe}–Y_{Fe}, Y_{Fe}–O_{oct}–Y_{Fe}, Ti_{Fe}–O_{Fe}–Ti_{Fe}, Ti_{Fe}–O_{oct}–Ti_{Fe}, Y_{Fe}–O_{Fe}–Ti_{Fe}, Y_{Fe}–O_{oct}–Ti_{Fe} atomic configurations of precipitates have been performed as well, however, without inclusion of V_{Fe} vacancies.
The migration energies and trajectories of Y atom (possessing the largest diameter among atoms considered in this study) inside pure and doped *fcc*-Fe lattice have been calculated using the Nudge Elastic Band (NEB) method as it provides the most accurate results for the migration trajectories.
The results described in this PhD Thesis is a major step towards the modeling of the yttrium oxide particle precipitation required to understand deeper the mechanisms of ODS steels formation.
The results of the calculations have been systematized and uploaded to our partners in IAM-AWP (KIT), Karlsruhe to form a database of the interactions between the defects in iron lattice, which should allow using these results as the base for further ab initio as well as for Lattice Kinetic Monte-Carlo modelling of the ODS steel formation.

7. Main theses

- The chosen approach for the *ab initio* calculations performed on *fcc* Fe lattice has been tested on basic parameters such as lattice constant, bulk modulus cohesive energy as well as on V_{Fe} vacancy formation energy. The results of the calculations are in a good agreement with both experimental data as well as with other theoretical studies.
- The results of the calculations prove that vacancies play a crucial role in the formation of the ODS nanoparticles in ODS steels as they play essential role in migration of impurity atoms inside *fcc*-Fe lattice (oxygen, titanium and yttrium) and stabilize defect complexes.
- The smallest binding energies in the configurations when O atoms occupy the substitute positions have been found when two Y or two Ti atoms as well as Y and Ti atoms are positioned as the 1NN. The binding energies between the defects very moderately increase with the growth of the distance between two Y or Ti atoms in Y-O_{Fe}-Y or Ti-O_{Fe}-Ti configurations as well as Y and Ti atoms in Y-O_{Fe}-Ti configurations when two Y or Ti atoms as well as Y and Ti atoms are 2NN, respectively.
- A pattern between the binding energies and the displacements of the defect atoms is established: the larger of the displacement of the defect atoms towards each other during the relaxation, the larger is their binding energy.
- The distance between the defect atoms has decreased more in the calculated Y_{Fe}-O_{Fe}-Ti_{Fe} compared with Y_{Fe}-O_{Fe}-Y_{Fe} configurations, which means that the local expansion of the crystalline lattice caused by the induced defects is

lower. This might explain the smaller average size of YTiO particles comparing with Y_2O_3 particles.

8. Literature

8.1. Author's publications related to this work

[P1] **A. Gopejenko**, Yu.F. Zhukovskii, P.V. Vladimirov, E.A. Kotomin, and A. Möslang, *Ab initio* simulation of yttrium oxide nanocluster formation on *fc*c-Fe lattice. – *J. Nucl. Mater.* 2010, **406**, p. 345–350.

[P2] **A. Gopejenko**, Yu.F. Zhukovskii, P.V. Vladimirov, E.A. Kotomin, and A. Möslang, Modeling of yttrium, oxygen atoms and vacancies in γ-iron lattice. – *J. Nucl. Mater.* 2011, **416**, p. 40-44.

[P3] **A. Gopejenko**, Yu.F. Zhukovskii, P.V. Vladimirov, E.A. Kotomin, and A. Möslang, Interaction between oxygen and yttrium impurity atoms as well as vacancies in *fcc*-iron lattice: *Ab initio* modeling. – Proc. NATO ARW „Nanodevices and Nanomaterials for Ecological Security" (Eds. Yuri N. Shunin and Arnold E. Kiv; Springer: Dordrecht, Netherlands) 2012, p. 149-160.

[P4] **A. Gopejenko**, Yu.F. Zhukovskii, E.A. Kotomin, Yu.A. Mastrikov, P.V. Vladimirov, V.A. Borodin, and A. Möslang, *Ab initio* modelling of Y–O cluster formation in *fcc*-Fe lattice. – *Phys. Status Solidi B*, 2016, **253**, p. 2136-2143.

[P5] V.I. Gopeyenko and **A. Gopejenko**, Using applications and tools to visualize *ab initio* calculations performed in *VASP*. - In a book: "Augmented Reality, Virtual Reality, and Computer Graphics". Lecture Notes in Computer Science (Eds. L.T. De Paolis and P. Bourdot; Springer International Publishing AG, Cham, Switzerland), 2018, Part I, p. 489-496.

[P6] **A. Gopejenko**, Yu.A. Mastrikov, Yu.F. Zhukovskii, E.A. Kotomin, P.V. Vladimirov, and A. Möslang, *Ab initio* modelling of the Y, O, and Ti solute interaction in *fcc*-Fe matrix. - *Nucl. Instrum. Methods Phys. Res. B* 2018, **433**, p. 106-110.

8.2. Other author's publications

[Q1] **A. Gopejenko**, S. Piskunov, and Yu.N. Shunin, The atomic and electronic structure of pure and defective $PbZrO_3$. – *Comput. Model. & New Technol. (Latvia)*, 2006, **10**(4), p. 7-16.

[Q2] S. Piskunov, **A. Gopejenko**, E.A. Kotomin, Yu.F. Zhukovskii, and D.E. Ellis, Atomic and electronic structure of perfect and defective $PbZrO_3$ perovskite: hybrid DFT calculations of cubic and orthorhombic phases. – *Comput. Mater. Sci.* 2007, **41**, p. 195-201.

[Q3] E.A. Kotomin, S. Piskunov, Yu.F. Zhukovskii, R.I. Eglitis, **A. Gopejenko**, and D.E. Ellis, The electronic properties of an oxygen vacancy at ZrO_2-terminated (001) surfaces of cubic $PbZrO_3$: Computer simulations from the first principles. – *Phys. Chem. Chem. Phys.* 2008, **10**, p. 4258-4263.

[Q4] **A. Gopejenko**, S. Piskunov, and Yu.F. Zhukovskii, *Ab initio* modelling of the effects of varying Zr (Ti) concentrations on the atomic and electronic properties of stoichiometric PZT solid solutions. – *Comput. Theor. Chem.* 2017, **1104**, p. 56-60.

[Q5] Yu.A. Mastrikov, M.N. Sokolov, S Koch, Yu.F. Zhukovskii, **A. Gopejenko**, P.V. Vladimirov, V.A. Borodin, E.A. Kotomin, and A. Möslang. "*Ab initio* modelling of the initial stages of the ODS particle formation process". – *Nucl. Instr. Meth. Phys. Res. B*, 2018, **435**, p. 70–73.

[Q6] Yu.A. Mastrikov, M.N Sokolov, E.A. Kotomin, **A. Gopejenko**, and Yu.F. Zhukovskii. "*Ab initio* modelling of Y and O solute atom interaction in small clusters within the *bcc* iron lattice". – *Phys. Status Solidi B*, 2018, **255**, 1800346 (p. 1-5).

8.3. References on regular publications for PhD Thesis

[1] R. Lindau, A. Möslang, M. Rieth, M. Klimiankou, E. Materna-Morris, A. Alamo, A.-A.F. Tavassoli, C. Cayron, A.-M. Lancha, P. Fernández, N. Baluc, R. Schäublin, E. Diegele, G.

Filacchioni, J.W. Rensman, B. Van der Schaaf, E. Lucon, W. Dietz, Present development status of EUROFER and ODS-EUROFER for application in blanket concepts, *Fusion Engineering Design* **75–79** (2005) 989–996
[2] M. Klimiankou, R. Lindau, A. Möslang, Direct correlation between morphology of $(Fe,Cr)_{23}C_6$ precipitates and impact behaviour or ODS steels, *J. Nucl. Mater.* **367–370** (2007) 173–178
[3] R. Lindau, A. Möslang, M. Schirra, P. Schlossmacher, M. Klimiankou, Mechanical and microstructural properties of a hipped RAFM ODS-steel, *J. Nucl. Mater.* **307–311** (2002) 769–772
[4] http://www.calphad.com/pdf/Fe_Cr_Phase_Diagram.pdf
[5] M. Klimiankou, R. Lindau, A. Möslang, HRTEM Study of yttrium oxide particles in ODS steels for fusion reactor application, *J. Cryst. Growth* **249** (2003) 381–387
[6] C. Cayron, E. Rath, I. Chu, S. Launois, Microstructural evolution of Y_2O_3 and $MgAl_2O_4$ ODS EUROFER steels during their elaboration by mechanical milling and hot isostatic pressing, *J. Nucl. Mater.* **335** (2004) 83–102
[7] E. Vanegas-Márquez, K. Mocellin, L. Toualbi, Y. de Carlan, R.E. Logé, A simple approach for the modeling of an ODS steel mechanical behavior in pilgering conditions, *J. Nucl. Mater.* **420** (2012) 479–490
[8] C.-L. Chen, Y.-M. Dong, Effect of mechanical alloying and consolidation process on microstructure and hardness of nanostructured Fe–Cr–Al ODS alloys, *Mater. Sci. Eng. A*, **528** (2011) 8374– 8380
[9] R. Schäublin, A. Ramar, N. Baluc, V. de Castro, M.A. Monge, T. Leguey, N. Schmid, C. Bonjour, Microstructural development under irradiation in European ODS ferritic/martensitic steels, *J. Nucl. Mater.* **351** (2006) 247–260
[10] T. Okuda and M. Fujiwara, Dispersion behaviour of oxide particles in mechanically alloyed ODS steel, *J. Mater. Sci. Lett.* **14**(22) (1995) 1600-1603
[11] C.A. Williams, E.A. Marquis, A. Cerezo, G.D.W. Smith, Nanoscale characterisation of ODS–Eurofer 97 steel: An atom-probe tomography study, *J. Nucl. Mater.* **400** (2010) 37-45.
[12] M. Klimenkov, R. Lindau, A. Möslang, New insights into the structure of ODS particles in the ODS-Eurofer alloy, *J. Nucl. Mater.* **386–388** (2009) 553–556
[13] V. de Castro, T. Leguey, A. Muñoz, M.A. Monge, P. Fernarndez, A.M. Lancha, R. Pareja, Mechanical and microstructural behaviour of Y_2O_3 ODS EUROFER 97, *J. Nucl. Mater.* **367–370** (2007) 196–201
[14] P. He, M. Klimenkov, R. Lindau, A. Möslang, Characterization of precipitates in nano structured 14% Cr ODS alloys for fusion application, *J. Nucl Mater* **428** (2012) 131–138
[15] M. Šćcepanović, V. de Castro, T. Leguey, M.A. Auger, S. Lozano-Perez, R. Pareja, Microstructural stability of ODS Fe–14Cr (–2W–0.3Ti) steels after simultaneous triple irradiation, *Nucl. Mater. Energy* **9** (2016) 490-495
[16] Y. Yagodzinskyy, E. Malitckii, M. Ganchenkova, S. Binyukova, O. Emelyanova, T. Saukkonen, H. Hänninen, R. Lindau, P. Vladimirov, A. Moeslang, Hydrogen effects on tensile properties of EUROFER 97 and ODS-EUROFER steels, *J. Nucl. Mater.* **444** (2014) 435–440
[17] O.V. Emelyanova, M.G. Ganchenkova, E. Malitskii, Y.N. Yagodzinskyy, M. Klimenkov, V.A. Borodin, P.V. Vladimirov, R. Lindau, A. Möslang, H. Hänninen, Investigation of microstructure changes in ODS-EUROFER after hydrogen loading, *J. Nucl. Mater.* **468** (2016) 355-359
[18] P. Olier, J. Malaplate, M.H. Mathon, D. Nunes, D. Hamona, L. Toualbi, Y. de Carlan, L. Chaffron, Chemical and microstructural evolution on ODS Fe–14CrWTi steel during manufacturing stages, *J. Nucl. Mater.* **428** (2012) 40–46
[19] R.A. Renzetti, H.R.Z. Sandim, M.J.R. Sandim, A.D. Santos, A. Möslang, D. Raabe, Annealing effects on microstructure and coercive field of ferritic–martensitic ODS Eurofer steel, *Mater. Sci. Eng. A* **528** (2011) 1442–1447
[20] R.A. Renzetti, H.R.Z. Sandim, R.E. Bolmaro, P.A. Suzuki, A. Moslang, X-ray evaluation of dislocation density in ODS-Eurofer steel, *Mater. Sci. Eng. A* **534** (2012) 142– 146
[21] M. Klimenkov, R. Lindau, E. Materna-Morris, A. Möslang, TEM characterization of precipitates in EUROFER 97, *Progress Nucl. Energy* **57** (2012) 8-13
[22] L. Toualbi, C. Cayron, P. Olier, J. Malaplate, M. Praud, M.-H. Mathon, D. Bossu, E. Rouesne, A. Montani, R. Logé, Y. de Carlan, Assessment of a new fabrication route for Fe–9Cr–1W ODS cladding tubes, *J. Nucl. Mater.* **428** (2012) 47–53

[23] M.A. Auger, V. De Castro, T. Leguey, J. Tarcísio-Costa, M.A. Monge, A. Muñoz, R. Pareja, Effect of yttrium addition on the microstructure and mechanical properties of ODS RAF steels, *J. Nucl. Mater.* **455** (2014) 600–604
[24] A. Chauhan, D. Litvinov, J. Aktaa, Deformation and damage mechanisms of a bimodal 12Cr-ODS steel under high-temperature cyclic loading, *Internat. J. Fatigue* **93** (2016) 1–17
[25] Z. Li, Z. Lu, R. Xie, C Lu, C. Liu, Effect of spark plasma sintering temperature on microstructure and mechanical properties of 14Cr-ODS ferritic steels, *Mater. Sci. Eng. A* **660** (2016) 52–60
[26] Y. Zhang, D. Liu, Y. Wang, J. Du, C. Zhang, S. Feng, T. Ouyang, J. Suo, A 9%Cr ODS steel composite material reinforced by Ti layers, *Mater. Sci. Eng. A* **676** (2016) 253–262
[27] M.J. Alinger, B.D. Wirth, H.-J. Lee, G.R. Odette, Lattice Monte Carlo simulations of nanocluster formation in nanostructured ferritic alloys, *J. Nucl. Mater.* **367–370** (2007) 153-159
[28] M.J. Alinger, On the Formation and Stability of Nanometer Scale Precipitates in Ferritic Alloys during Processing and High Temperature Service, *PhD Dissertation*, University of California, Santa Barbara (2004)
[29] P.A. Schulz and R.P. Muller, *QUantum Electronic STructure (SeqQuest Electronic Structure Code)* Sandia National Laboratories, Albuquerque (NM), (2004). http://dft.sandia.gov/Quest
[30] J.H. Rose, J.R. Smith, F. Guinea, J. Ferrante, Universal features of the equation of state of metals, *Phys. Rev. B* **29** (1984) 2963-2969
[31] J.E. Lennard-Jones, On the determination of molecular fields. -II. From the equation of state of a gas, *Proc. Royal Society (London) A* **106** (1924) 463-477
[32] S. Ukai, T. Nishida, H. Okada, T. Okuda, M. Fujiwara, K. Asabe, Development of Oxide Dispersion Strengthened Ferritic Steels for FBR Core Application, (I), *J. Nucl. Sci. Technol.* **34** (1997) 256-263.
[33] A. Claisse, *Ab Initio* based Multi-Scale Simulations of Oxide Dispersion Strengthened Steels, *M. Sc. Thesis*, King Technological University, Stockholm (2012)
[34] C.L. Fu, M. Krčmar, G.S. Painter, X.-Q. Chen, Vacancy Mechanism of High Oxygen Solubility and Nucleation of Stable Oxygen-Enriched Clusters in Fe, *Phys. Rev. Lett.* **99** (2007) 225502
[35] M.-M. Peng, W.-Sh. Lai. Interaction between vacancies and the α-Fe/Y_2O_3 interface: A first-principles study, *Nucl. Instrum. Meth. Phys. Res. B* **352** (2015) 67–71
[36] A. Claisse, P. Olsson, First-principles calculations of (Y, Ti, O) cluster formation in body centred cubic iron-chromium, *Nucl. Instrum. Meth. Phys. Res. B* **303** (2013) 18–22
[37] Y. Jiang, J.R. Smith, G.R. Odette, Formation of Y-Ti-O nanoclusters in nanostructured ferritic alloys: A first-principles study, *Phys. Rev. B* **79** (2009) 064103
[38] D. Murali, B.K. Panigrahi, M.C. Valsakumar, Sh. Chandra, C.S. Sundar, B. Raj, The role of minor alloying elements on the stability and dispersion of yttria nanoclusters in nanostructured ferritic alloys: An *ab initio* study, *J. Nucl. Mater.* **403** (2010) 113–116
[39] T.P.C. Klaver, P. Olsson, M.W. Finnis, Interstitials in FeCr alloys studied by density functional theory, *Physical Review B* **76** (2007) 214110
[40] C. Pareige, C. Domain, P. Olsson, Short- and long-range orders in Fe–Cr: A Monte Carlo study, *J. Appl. Phys.* **106** (2009) 104906
[41] Atomistix ToolKitManual. http://www.quantumwise.com/documents/manuals/ATK-2008.10/index.html
[42] A.D. Le Claire, *Physical Chemistry: An Advanced Treatise*, Vol. 10. Academic Press, New York, 1970, p. 684
[43] M.K. Miller, E.A. Kenik, K.F. Russell, L. Heatherly, D.T. Hoelzer, P.J. Maziasz, Atom probe tomography of nanoscale particles in ODS ferritic alloys, *Mater. Sci. Eng. A* **353** (2003) 140–145
[44] P. Erhart, A first-principles study of helium storage in oxides and at oxide–iron interfaces, *J. Appl. Phys.* **111** (2012) 113502
[45] L. Yang, Y. Jiang, G.R. Odette, T. Yamamoto, Z Liu, Y. Liu, Trapping helium in $Y_2Ti_2O_7$ compared to in matrix iron: A first principles study, *J. Appl. Phys.* **115** (2014) 143508
[46] G.D. Samolyuk, Yu.N. Osetsky, Thermodynamic approach to the stability of multi-phase systems: application to the Y_2O_3–Fe system, *J. Phys.: Condens. Matt.* **27** (2015) 305001 (1-9)
[47] J. Brodrick, D.J. Hepburn, G.J. Ackland, Mechanism for radiation damage resistance in yttrium oxide dispersion strengthened steels, *J. Nucl. Mater.* **445** (2014) 291–297

[48] A.V. Ponomareva, Yu.N. Gornostyrev, I.A. Abrikosov, Ab initio calculation of the solution enthalpies of substitutional and interstitial impurities in paramagnetic fcc Fe, *Phys. Rev. B* **90** (2014) 014439.
[49] J. Hubbard, The magnetism of iron, *Phys. Rev. B* **19** (1979) 2626-2636; Magnetism of iron. II, *Phys. Rev. B* **20** (1979) 4584-4595; Magnetism of nickel, *Phys. Rev. B* **23** (1981) 5974-5977.
[50] H. Hasegawa, Single-Site Functional-Integral Approach to Itinerant-Electron Ferromagnetism, *J. Phys. Soc. Jpn.* **46** (1979) 1504-1514; Ising Model and Bethe Approximation in Itinerant-Electron Systems. II. Iron and Nickel, *J. Phys. Soc. Jpn.* **49** (1980) 178-188.
[51] B. Drittler, M. Weinert, R. Zeller, P.H. Dederichs, First-principles calculation of impurity-solution energies in Cu and Ni, *Phys. Rev. B* **39** (1989) 930
[52] G. Kresse and J. Furthmüller, *VASP* the Guide, University of Vienna, 2009; http://cms.mpi.univie.ac.at/vasp/
[53] G. Kresse and D. Joubert, From ultrasoft pseudopotentials to the projector augmented-wave method, *Phys. Rev. B* **59** (1999) 1758-1775
[54] R.A. Evarestov, Quantum Chemistry of Solids: The LCAO First Principles Treatment of Crystals. Springer Series in Solid State Science, Springer-Verlag, Berlin, Heidelberg, 2007, 557 p.
[55] M. Born and J.R. Oppenheimer, Zur Quantentheorie der Molekeln (Germ.), *Ann. Phys.* **84** (1927) 457-484
[56] R.G. Parr and W. Yang, Density Functional Theory of Atoms and Molecules, Oxford Univ. Press, New York, Oxford, 1989, 352 p.
[57] L.H. Thomas, The calculation of atomic fields, *Proc. Camp. Philos. Soc.* **23** (1927) 542-548
[58] E. Fermi, Un metodo statistico per la determinazione di alcune priorieta dell'atome (Ital.), *Rend. Accad. Naz. Lincei* **6** (1927) 602–607
[59] P. Hohenberg and W. Kohn, Inhomogeneous electron gas, *Phys. Rev.* (1964) **136** B864–B871.
[60] W. Kohn and L.J. Sham, Self-consistent equations including exchange and correlation effects, *Phys. Rev.* **140** (1965) A1133–A1138
[61] J.C. Slater, Quantum Theory of Atomic Structure, Vol. 1, McGraw-Hill Book Co, Inc., New York, 1960, p. 502
[62] D.M. Ceperley and B.J. Alder, Ground state of the electron gas by a stochastic method. *Phys. Rev. Lett.* **45** (1980) 566–569
[63] R.M. Martin, Electronic Structure: Basic Theory and Practical Methods, Cambridge Univ. Press, London, 2005, 647 p.
[64] J.P. Perdew, J.A. Chevary, S.H. Vosko, K.A. Jackson, M.R. Pederson, D.J. Singh, and C. Fiolhais, Atoms, molecules, solids, and surfaces: Applications of the generalized gradient approximation for exchange and correlation. *Phys. Rev. B* **46** (1992) 6671–6687
[65] J.P. Perdew, K. Burke, and M. Ernzerhof, Generalized gradient approximation made simple *Phys. Rev. Lett.* **77** (1996) 3865–3868
[66] L.N. Kantorovich, Quantum Theory of the Solid State: An Introduction. Kluwer Acad. Publ., Dordrecht, 2004, 626 p.
[67] C. Delerue and M. Lannoo, Nanostructures: Theory and Modeling, Springer-Verlag, Berlin, Heidelberg, 2004, 297 p.
[68] N.W. Ashcroft and N.D. Mermin, Solid State Physics, Saunders Coll. Press, Philadelphia, 1976, 848 p.
[69] P.E. Bloechl, Projector augmented-wave method, *Phys. Rev. B*, **50** (1994) 17953-17979
[70] N. Troullier and J.L. Martins, Efficient pseudopotentials for plane-wave calculations, *Phys. Rev. B*, **43** (1991) 1993–2006
[71] S. Goedecker, W. Hellmann, and T. Lenosky, Global minimum determination of the Born-Oppenheimer surface within density functional theory, *Phys. Rev. Lett.*, **95** (2005) 55501
[72] A.R. Oganov and C.W. Glass, Crystal structure prediction using *ab initio* evolutionary techniques: Principles and applications, *J. Chem. Phys.*, **124** (2006) 244704
[73] C.W. Glass, A.R. Oganov, and N. Hansen, USPEX–Evolutionary crystal structure prediction. *Comput. Phys. Commun.*, **175** (2006) 713–720
[74] C.J. Pickard, R.J. Needs, High-pressure phases of silane, *Phys. Rev. Lett.*, **97** (2006) 45504
[75] A. Pedersen, S.F. Hafstein, and H. Jónsson, Efficient sampling of saddle points with the minimum-mode following method, *SIAM J. Sci. Comput.*, **33** (2011) 633-652

[76] V. Jadhao and N. Makri, Iterative Monte Carlo with bead-adapted sampling for complex-time correlation functions, *J. Chem. Phys.*, **132** (2010) 104110
[77] J. Hafner, *Ab initio* simulations of materials using VASP: Density-Functional Theory and beyond, *J. Comput. Chem.*, **29** (2008) 2044–2078
[78] A. Unsöld, Beiträge zur Quantenmechanik des Atoms (Germ.), *Ann. Phys.*, **82** (1927) 355-393; http://demonstrations.wolfram.com/UnsoeldsTheorem/
[79] M. Krack, Pseudopotentials for H to Kr optimized for gradient-corrected exchange-correlation functionals, *Theor. Chem. Acc.*, **114** (2005) 145-152.
[80] H.J. Monkhorst, J.D. Pack, Special points for Brillouin-zone integrations, *Phys. Rev. B*, **13** (1976) 5188-5192.
[81] M. Methfessel and A.T. Paxton, High-precision sampling for Brillouin-zone integration in metals. *Phys. Rev. B*, **40** (1989) 3616–3621.
[82] http://theory.cm.utexas.edu/vtsttools/index.html
[83] V.L. Moruzzi, P.M. Marcus, K. Schwarz, P. Mohn, Ferromagnetic phases of bcc and fcc Fe, Co, and Ni, *Phys. Rev. B* **34** (1986) 1784–1791
[84] H. Mehrer (Ed.), Diffusion in Solid Metals and Alloys, Landolt–Börnstein, New Series III, Springer-Verlag, Berlin, Heidelberg, 1990, 481 p.
[85] M. Marsman, J. Hafner, Broken symmetries in the crystalline and magnetic structures of γ-iron, *Phys. Rev. B* **66** (2002) 224409
[86] J.T. Wang, D.S. Wang, Y. Kawazoe, Finite-temperature magnetism of tetragonal iron, *Appl. Phys. Lett.* **88** (2006) 132513
[87] W. Zhong, G. Overney, D. Tománek, Structural properties of Fe crystals, *Phys. Rev. B* **47** (1993) 95–99
[88] G. Ghosh, G.B. Olson, The isotropic shear modulus of multicomponent Fe-base solid solutions, - *Acta Mater.* **50** (2002) 2655–2675
[89] Yu.F. Zhukovskii, P.W.M. Jacobs, M. Causá, On the mechanism of the interaction between oxygen and close-packed single-crystal aluminum surfaces, *J. Phys. Chem. Solids* **64** (2003) 1317-1331
[90] G. Henkelman A. Arnaldsson, H Jónsson, A fast and robust algorithm for Bader decomposition of charge density, *Comput. Mater. Sci.* **36** (2006) 354-360

9. Contributions at scientific conferences

1. The 3rd International Conference "Information Technologies and Management", IT&M'2006 (Riga, Latvia, April, 2005). **A. Gopejenko**, V.I. Gopeyenko and Yu.N. Shunin, "Data base of nanoclusters fundamental electronic and mechanical properties creation". Abstract: pp. 43-44.

2. The 4th International Conference "Information Technologies and Management", IT&M'2006 (Riga, Latvia, April, 2006). **A. Gopejenko**, S. Piskunov and Yu. N. Shunin, „*Ab initio* calculations of atomic and electronic structure of pure and defective $PbZrO_3$". Abstract: p. 18.

3. 22nd ISSP Conference (Riga, Latvia, March, 2006). **A. Gopejenko**, R.I. Eglitis, and S. Piskunov, "Electronic structure of pure and defective $PbZrO_3$: First-principles calculations". Abstract: p. 17.

4. 23rd ISSP Conference (Riga, Latvia, February, 2007). **A. Gopejenko**, R.I. Eglitis, and S. Piskunov, "*Ab initio* calculations of perfect and defective $PbZrO_3$ surfaces". Abstract: p. 18.

5. International Workshop "Fundamental Physics of Ferroelectrics", (Williamsburg, VA, USA, February, 2007). R.I. Eglitis, **A. Gopeyenko**, S. Piskunov, Yu.F. Zhukovskii, and J. Lee, "Electronic structure of perfect and defective $PbZrO_3$ (001): *Ab initio* simulations". Abstracts: pp. 37-38.

6. The 5th International Conference "Information Technologies and Management", IT&M'2007 (Riga, Latvia, April, 2007). **A. Gopejenko**, S. Piskunov, R.Eglitis and Yu. N. Shunin, „*Ab initio* calculations of perfect and defective $PbZrO_3$ (001) surfaces". Abstract: pp. 13-14.

7. 24th ISSP Conference (Riga, Latvia, February, 2008). **A. Gopejenko**, Yu.F Zhukovskii, P.V. Vladimirov, and E.A. Kotomin, "*Ab initio* calculations of O and Y impurities in *fcc* Fe lattice". Abstracts: p. 4.

8. The 6th International Conference "Information Technologies and Management", IT&M'2008 (Riga, Latvia, April, 2008). **A. Gopejenko**, Yu.F. Zhukovskii, P.V. Vladimirov, and E.A. Kotomin, "Ab initio Calculations of oxygen and yttrium impurities in fcc Fe". Abstracts: p. 23.

9. 25th International Symposium on Fusion Technology, (Rostock, Germany, September, 2008).

A. Gopejenko, Yu.F. Zhukovskii, P.V. Vladimirov, E.A. Kotomin, and A. Moslang, "Simulation of yttrium oxide particle formation in iron in support of ODS steel development". Abstract: p. 226.

10. 25th ISSP Conference (Riga, Latvia, February, 2009). **A. Gopejenko**, Yu.F. Zhukovskii, P.V. Vladimirov, E.A. Kotomin, and A. Möslang, "Simulation of yttrium and oxygen solute atoms in fcc Fe lattice in support of ODS steel development. Abstract: p. 55.

11. International conference "Functional materials and nanotechnologies" FM&NT-2009 (Riga, Latvia, April, 2009). **A. Gopejenko**, Yu.F. Zhukovskii, P. Vladimirov, E.A. Kotomin, and A. Moslang, "Simulations on solution of yttrium and oxygen atoms in *fcc* iron lattice". Abstract: p. 101.

12. The 7th International Conference "Information Technologies and Management", IT&M'2009 (Riga, Latvia, April, 2009). **A. Gopejenko**, Yu.F. Zhukovskii, P.V. Vladimirov, E.A. Kotomin, and A. Möslang, "Simulation of yttrium oxide particle formation in iron in support of ODS steel development". Abstract: pp. 30-31.

13. 26th ISSP Conference (Riga, Latvia, February, 2010). **A. Gopejenko**, Yu.F. Zhukovskii, P.V. Vladimirov, E.A. Kotomin, and A. Möslang, "Y-, O- and Fe-vacancy defect complex modeling in *fcc* Fe lattice". Abstract: p. 30.

14. International conference "Functional materials and nanotechnologies" FM&NT-2010 (Riga, Latvia, March, 2010). **A. Gopejenko**, Yu.F. Zhukovskii, P.V. Vladimirov, E.A. Kotomin, and A. Moslang, "*Ab initio* calculations of yttrium and vacancy point defects for ODS steels modeling". Abstract: p. 182.

15. The 8th International Conference "Information Technologies and Management", IT&M'2010 (Riga, Latvia, April, 2010). **A. Gopejenko**, Yu.F. Zhukovskii, P.V. Vladimirov, E.A. Kotomin, and A. Möslang, "Simulation of yttrium oxide particle formation in iron in support of ODS steel development". Abstracts: p. 20-21.

16. Spring European Materials Research Society (E-MRS) Meeting (Strasbourg, France, June, 2010). **A. Gopejenko**, Yu.F. Zhukovskii, P.V. Vladimirov, E.A. Kotomin, and A. Möslang, „Pair and triple point defect complex modeling in *fcc* Fe lattice". Abstracts: NPVI-13.

17. 27th ISSP Conference (Riga, Latvia, February, 2011). **A. Gopejenko**, Yu.F. Zhukovskii, P.V. Vladimirov, E.A. Kotomin, and A. Möslang, „*Ab initio* calculations of binding energies between defects in *fcc* Fe lattice". Abstracts: p. 6.

18. International conference "Functional materials and nanotechnologies" FM&NT-2011 (Riga, Latvia, April, 2011). **A. Gopejenko**, Yu.F. Zhukovskii, P.V. Vladimirov, E.A. Kotomin, and A. Möslang, "*Ab initio* calculations of pair-wise interactions between defects for ODS steels". Abstracts: p. 165.

19. Spring European Materials Research Society (E-MRS) Meeting (Nice, France, May, 2011). **A. Gopejenko**, Yu.F. Zhukovskii, P.V. Vladimirov, V.A. Borodin, E. A. Kotomin, and A. Möslang, "Modelling of interactions between Y, O and vacancy clusters in *fcc* Fe lattice". Abstracts: VP-7.

20. NATO Advanced Research Workshop "Nanomaterials and Nanodevices for Ecological Security" (Jurmala, Latvia, June, 2011). **A. Gopejenko**, Yu.F. Zhukovskii, P.V. Vladimirov, E.A. Kotomin,

and A. Möslang, "Interaction of O and Y impurity atoms as well as Fe lattice: *Ab initio* modeling". Abstracts: PB06.

21. 28th ISSP Conference (Riga, Latvia, February, 2012). **A. Gopejenko**, Yu.F. Zhukovskii, P.V. Vladimirov, E.A. Kotomin, Yu.A. Mastrikov, and A. Möslang. "*Ab initio* calculations of binding energies between defects in *fcc* Fe lattice for further kinetic Monte-Carlo simulation on ODS steel". Abstracts: p. 19.

22. 10th International Conference "Information Technologies and Management", IT&M'2012 (Riga, Latvia, April, 2012). **A. Gopejenko**, Yu.F. Zhukovskii, P.V. Vladimirov, E.A. Kotomin, and A. Möslang, "Quantum chemical calculations of binding energies between Y and O impurity atoms and Fe vacancies inside iron lattice for ODS steels". Abstracts: p. 19.

23. 8th International Conference "Functional Materials and Nanotechnologies" FM&NT-2012 (Riga, Latvia, April, 2012). **A. Gopejenko**, Yu.F. Zhukovskii, P.V. Vladimirov, E.A. Kotomin, and A. Möslang, Quantum chemical simulations on binding energies of pair and tripe-wise defects in *fcc*-Fe lattice for ODS steels. – Abstract: p. 306.

24. First Baltic School on Application of Neutron and Synchrotron Radiation in Solid State Physics and Material Science, BSANS-2012 (Riga, Latvia, October, 2012). **A. Gopejenko**, Yu.F. Zhukovskii, P.V. Vladimirov, E.A. Kotomin, Yu. Mastrikov, and A. Möslang, *Ab initio* modelling of the yttrium and oxigen nanoparticle formation inside fcc iron latice for ods steels development. - Abstracts: p. 30.

25. 29th ISSP Conference (Riga, Latvia, February, 2013). **A. Gopejenko**, Yu.F. Zhukovskii, P.V. Vladimirov, E.A. Kotomin, J.Mastrikov, and A. Möslang, "*Ab initio* calculations of Y and vacancies interactions in *fcc* Fe lattice". Abstracts: p. 61.

26. 11th International Conference "Information Technologies and Management", IT&M'2013 (Riga, Latvia, April, 2013). **A. Gopejenko**, Yu.F. Zhukovskii, P.V. Vladimirov, E.A. Kotomin, Yu.A. Mastrikov, and A. Möslang, "First principles modeling of interactions between Y, O and vacancies in fcc-Fe lattice". Abstracts: p. 112-114.

27. 9th International Conference "Functional Materials and Nanotechnologies" FM&NT-2013 (Tartu, Estonia, April, 2013). Yu.F. Zhukovskii, **A. Gopejenko**, Yu.A. Mastrikov, E.A. Kotomin, P.V. Vladimirov, and A. Möslang, "Modeling of Y-O precipitation in *bcc*-Fe and *fcc*-Fe lattices." – Abstract: OR-35.

28. 30th ISSP Conference (Riga, Latvia, February, 2014). **A. Gopejenko**, Yu.F. Zhukovskii, P.V. Vladimirov, E.A. Kotomin, Yu.A. Mastrikov, V.A. Borodin, and A. Möslang, "First principles calculations of the energy barriers for different trajectories of Y atom migration inside *fcc*-Fe lattice". Abstracts: p. 36.

29. 12th International Conference "Information Technologies and Management", IT&M'2014 (Riga, Latvia, April, 2014). **A. Gopejenko**, Yu.F. Zhukovskii, P.V. Vladimirov, Yu.A. Mastrikov, E.A. Kotomin, V.A. Borodin, and A. Möslang, "*Ab initio* calculations of interactions between Y, O impurity atoms and Fe vacancies for ODS steel implementation in fusion reactors". Abstracts: p. 21-22. *30. Joint 12th RCBJCF Symposium and 9th FMNT Conference (Riga, Latvia, September-October, 2014).*

A. Gopejenko, Yu.F. Zhukovskii, P.V. Vladimirov, E.A. Kotomin, Yu.A. Mastrikov, V.A. Borodin, and A. Möslang, "*Ab initio* calculations of interactions between Y and O impurity atoms and vacancies in bcc- and fcc-iron lattices". Abstracts: p. 282.

31. 31th ISSP Conference (Riga, Latvia, February, 2015). **A. Gopejenko**, Yu.F. Zhukovskii, P.V. Vladimirov, E.A. Kotomin, Yu.A. Mastrikov, V.A. Borodin, and A. Möslang, "*Ab initio* calculations of Y, O and V_{Fe} diffusion barriers inside fcc-Fe lattice". Abstract: p. 41. *32. 13th International Conference "Information Technologies and Management", IT&M'2015 (Riga, Latvia, April, 2015).* **A. Gopejenko**, Yu.F. Zhukovskii, P.V. Vladimirov, V.A. Borodin, E.A. Kotomin, Yu.A. Mastrikov,

and A. Möslang, “Ab initio calculations of Y, O and V_{Fe} migration barriers inside fcc-Fe lattice”. Abstract: p. 21.

33-34. 32th ISSP Conference (Riga, Latvia, February, 2016). **A. Gopejenko**, Yu.F. Zhukovskii, P.V. Vladimirov, E.A. Kotomin, Yu.A. Mastrikov, V.A. Borodin, and A. Möslang, “*Ab initio* calculations of O and V_{Fe} interaction in *fcc* Fe lattice”. Abstract: p. 37. **A. Gopejenko**, Yu.F. Zhukovskii, S. Piskunov, E.A. Kotomin, “Variation of Zr and Ti concentration in PZT: first principles calculations on the electronic structure”. Abstract: p. 95.

35. 14th International Conference "Information Technologies and Management", IT&M'2016 (Riga, Latvia, April, 2016). **A. Gopejenko**, Yu.F. Zhukovskii, S. Piskunov, and E.A. Kotomin, “First principle calculations of PZT varying Zr and Ti concentrations”. Abstract: p. 22.

36. 33rd ISSP Conference (Riga, Latvia, February, 2017). **A. Gopejenko**, Yu.F. Zhukovskii, P.V. Vladimirov, E.A. Kotomin, Yu.A. Mastrikov, V.A. Borodin, and A. Möslang, "A comparative analysis of Y and Ti pairwise interactions in *fcc* Fe lattice: the first principle calculations". Abstract: p. 61.

37. Functional Materials and Nanotechnologies 2017, FM&NT2017 (Tartu, Estonia, April 2017). **A. Gopejenko**, Yu.A. Mastrikov, Yu.F. Zhukovskii, E.A. Kotomin, P.V. Vladimirov, V.A. Borodin, and A. Möslang, “*Ab initio* modelling of pair-wise interactions of Ti solute with Y and O impurities and V_{Fe} vacancies in alfa- and gamma-Fe lattices”. Abstract: P-109.

38. 15th International Conference "Information Technologies and Management", IT&M'2017 (Riga, Latvia, April 2017). **A. Gopejenko**, Yu.F. Zhukovskii, P.V. Vladimirov, E.A. Kotomin, Yu.A. Mastrikov, V.A. Borodin, and A. Möslang, “*Ab initio* calculations of Ti pair-wise interactions inside *fcc*-Fe lattice”. Abstract: p. 13.

39. 19th International Conference on Radiation Effects in Insulators, REI2017 (Versailles, France, July 2017). E.A. Kotomin, Yu.A. Mastrikov, P.V. Vladimirov, V.A. Borodin, S. Koch, **A. Gopejenko**, Yu.F. Zhukovskii, A. Möslang, “*Ab initio* modeling of the Y, O solute interaction in iron matrix”. Abstract: p. 218.

40. Fall European Materials Research Society (E-MRS) Meeting (Warsaw, Poland, September, 2017). Yu.A. Mastrikov, P.V. Vladimirov, V.A. Borodin, S. Koch, **A. Gopejenko**, Yu.F. Zhukovskii, E.A. Kotomin, and A. Möslang, “*Ab initio* modelling of the Y,O solute interaction in iron matrix”. Abstracts: E, p. 119-3.

41. 34th ISSP Conference (Riga, Latvia, February 2018). **A. Gopejenko**, Yu.F. Zhukovskii, Yu.A. Mastrikov, P.V. Vladimirov, E.A. Kotomin, and A. Möslang. "Modelling of Y-Ti-O precipitate inside the *fcc*-Fe lattice in support of ODS particle formation". Abstract: p. 91.

42. 16th International Conference "Information Technologies and Management", IT&M'2018 (Riga, Latvia, April 2018). **A. Gopejenko**, Yu.F. Zhukovskii, Yu.A. Mastrikov, E.A. Kotomin, and P.V. Vladimirov. "*Ab in*itio simulations of the Y, Ti and O solute interactions in *fcc*-Fe lattice in presence of V_{Fe} vacancies". Abstract: pp. 11-12.

43. E-MRS 2018 Spring Meeting (Strasbourg, France, June 2018). Yu.A. Mastrikov, M. Sokolov, E.A. Kotomin, **A. Gopejenko**, and Yu.F. Zhukovskii. "*Ab initio* modelling of Y and O solute atom interaction in small clusters within the *bcc* iron lattice". Abstract: K.PI.5.

44. 35th ISSP Conference (Riga, Latvia, February 2019). **A. Gopejenko**, Yu.F. Zhukovskii, Yu.A. Mastrikov, S. Piskunov, P.V. Vladimirov, E.A. Kotomin, and A. Möslang. "The first principles calculations of the Y, Ti, O, and V_{Fe} interactions inside the *fcc*-Fe lattice in support of ODS particle formation". Abstract: p. 42.

45. 17th International Conference "Information Technologies and Management", IT&M'2019 (Riga, Latvia, April 2019). **A. Gopejenko**, Yu.F. Zhukovskii, Yu.A. Mastrikov, E.A. Kotomin, S. Piskunov,

and P.V. Vladimirov. "First princpiple calculations of Y,Ti, and O solute interactions in *fcc*-Fe lattice for ODS steels development". Abstract: pp. 9-10.

Acknowledgements

The author gratefully acknowledges the doctoral studies support by the European Social Fund and European Social Fund project No. 2009/0216/1DP/1.1.1.2.0/09/APIA/VIAA/044.
This work has been carried out within the framework of the EUROfusion Consortium and has received funding from the Euratom research and training programme 2014 –2018 under grant agreement no. 633053. The views and opinions expressed herein do not necessarily reflect those of the European Commission.
The author sincerely thanks E.A. Kotomin, Yu.A. Mastrikov, S. Piskunov, G. Zvejnieks, J. Purans, A. Anspoks, V.A. Borodin, and M. Klimenkov for valuable suggestions and many stimulating discussions.
The author is especially grateful to D. Bocharov and M. Putnina for invaluable help in finalizing and polishing PhD thesis.
The author is thankful to P.V. Vladimirov for valuable suggestions and many stimulating discussions both during PhD studies and PhD thesis preparation.
The author is grateful to the medical staff of the Oncology Centre of Latvia and to the medical staff of the Department of Thoracic Surgery of Centre of Tuberculosis and Lung Diseases.
The author is sincerely thankful to D. Zelencova and N. Dunko-Lazdina for support during the scientific work and the PhD thesis preparation.
The author is especially grateful to his parents for support throughout the whole period of PhD studies.
The author expresses special gratitude to his uncle Yu. N. Shunin who brought him to science and helped with valuable advises and discussions.
The author is sincerely grateful to his scientific advisor Yu.F. Zhukovskii for permanent support of scientific work during the whole period of PhD studentship, including Thesis preparation.
It is very sorrowful that Yu. N. Shunin and Yu.F. Zhukovskii have passed away, however, they will never be forgotten and the memory of them will stay in author's heart forever.